Characterization of Pd nanoparticles and of silica-supported Pd-catalysts for the Suzuki-Miyaura reaction.

By

Mohammad Abu Hanif

A thesis submitted to the Department of Chemistry

in conformity with the requirements for

the degree of Doctor of Philosophy

Queen's University

Kingston, Ontario, Canada

September 2014

Abstract

The importance of palladium (Pd) as a catalyst in organic coupling reactions is undeniable. Mesoporous silica is widely used as the support of Pd catalysts. But the porous structure of the mesoporous silica limits complete characterization. As a result, heterogeneous Pd catalysts are not fully understood.

Model Suzuki-Miyaura reaction catalysts have been made by immobilizing Pd on a mercaptopropyltrimethoxysilane (MPTMS) functionalized Si substrate. Two types of Pd species were found on the fresh catalysts that may be attributed to a S-bound Pd (II) species and Pd nanoparticles. A sulfur species that has not been previously reported on this class of catalysts has also been observed. A systematic study of various palladium/sulfur complexes using XPS was carried out to identify this species, which may be assigned to high oxidation state sulfur formed by oxidation of thiol during the reduction of the $Pd(OAc)_2$ used to load the catalyst with Pd. Shifts in binding energy observed for both Pd and S spectra of the used catalysts were examined in order to probe the change of electronic environment of reactive palladium center and the thiol ligand during the reaction. Electron and atomic force microscopic imaging of the surfaces demonstrates the formation of Pd nanoparticles on fresh catalysts and subsequent size reduction of the Pd nano-particles following reaction.

Nanoparticles have gained increased attention due to their unique properties different from the bulk materials. Polyvinyl pyrrolidone (PVP) and dodecyl sulfide stabilized palladium nanoparticles have been synthesized with a size range of 3 to 10 nm and 2 to 5 nm respectively. XPS confirmed the conversion of Pd (II) to Pd (0) and presence of stabilizing agent on nanoparticles surface by observing Pd 3d, N1s (for PVP stabilized) and S 2p (for dodecyl sulfide

stabilized) high resolution spectra. Dispersion and size of the nanoparticles were measured by TEM. It was observed that the shift of binding energy of the nanoparticles is strongly size dependent. Finally, the ability of N-heterocyclic carbenes (NHCs) to substitute the stabilizing agent of Pd nanoparticles was investigated. The XPS studies suggest the substitution of dodecyl sulfide from the Pd nanoparticles by NHCs.

Acknowledgements

The last five years in the Chemistry department have been full of joy and decisive. At this moment, I would like to take the opportunity to acknowledge the people who have been such supportive and made my time with huge positive experience.

I would like to start thanking my supervisor, Prof. J. Hugh Horton, for his guidance and being supportive at every stage of my research. I am grateful for the opportunities such as giving chance to present my works in different conferences you have provided to me while working in your lab. Thanks to Prof. Hans-Peter Loock and Prof. Donal H. Macartney for being my research committee members and advisors. Your insightful comments and guidelines were very helpful and encouraging. Working in Dr. Horton's group has also afforded me the scope to work with some very talented people. They were very helpful in getting me started. They made our lab a friendly place to work. Thanks to Peiling and Alyza for being so friendly and supportive. I owe a debt of gratitude to Dr. Iraklii for being so supported in the last four years. I also want to thank all the members of chemistry department for being so cooperative.

Inside and outside of lab, I have shared beautiful times with my wife, my constant companion, Ruba. Without you my time in Kingston would not have been the same. Your encouragement, commitment, and love have brought me here today. Thank you. Lastly, and most importantly, thanks to my mother, father, sisters and brothers. Thanks for your constant inspiration and prayer. I am indebted to you all. Please keep me in your prayer.

Statement of Originality

I hereby certify that all of the work described within this thesis is the original work of the author carried out under the supervision of Prof. Hugh Horton. Dr. Iraklii Ebralidze assisted me with the Suzuki-Miyaura reactions and GC-MS analysis described in chapter 4. The ternary diagrams in chapter 4 are done by Dr. Iraklii. Any published (or unpublished) ideas and/or techniques from the work of others are fully acknowledged in accordance with the standard referencing practices.

Mohammad Abu Hanif

September 2014

Table of Contents

List of Figures

List of Tables

List of Abbreviations

AES	Auger electron spectroscopy
AFM	Atomic force microscope
APTES	Aminopropyltriethoxysilane
Au	Gold
BE	Binding energy
DI	Deionized
DMF	Dimethylformamide
DMSO	Dimethyl sulfoxide
EG	Ethylene glycol
eV	Electron volt
ESCA	Electron spectroscopy for chemical analysis
GC-MS	Gas chromatography-mass spectrometry
KE	Kinetic energy
LB	Langmuir and Blodgett
LFM	Lateral force microscopy
MFM	Magnetic force microscopy
MPTMS	3-mercaptopropyltrimethoxysilane
mM	Millimole
NHC	N-heterocyclic Carbene
nm	Nanometer
OTS	Octadecyltrichlorosilane

Pd	Palladium
PF8	Perfluorooctytriethoxysilane
PVP	Polyvinylpyrolidone
R_a	Roughness
RCA	Radio corporation of America
R^{ea}	Extra-atomic relaxation
R & D	Research and Development
SAM	Self-assembled monolayer
SBA	Santa Barbara amorphous
SEM	Scanning electron microscope
SH	Thiol
Si	Silicon
SNOM	Scanning near-field optical microscopy
SPM	Scanning probe microscope
STM	Scanning tunneling microscope
TEM	Transmission electron microscope
TOABr	Tetraoctyl ammonium bromide
THF	Tetrahydrofuran
TON	Turn over number
UV-Vis	Ultra-violet visible spectroscopy
XPS	X-ray photoelectron spectroscopy
XRD	X-ray diffraction

Chapter 1

Introduction

1.1. Surface Science and Catalysis

1.1.1 Introduction

The application of surface science has enormous economic impact in our society. It plays an indispensable role in industries such as chemical and energy conversion, information processing, health care, and material and environmental protection.[1] Surfaces are of particular interest to chemists in understanding the process of a particular chemical reaction. In many cases, modern surface science techniques can directly observe the changes occurring during different stages of the reaction process. Solid surfaces are interesting because the atoms of a surface do not have a full complement of neighbours which results in the lower coordination number than that for atoms in the bulk solid.[2] The consequences of the lower coordination number of surface atoms lead to different electronic structures than in the bulk and favours adsorption of gas or solvent molecules. Since the arrangement of surface atoms is different than that in the bulk, these surface atoms generally possess high reactivity. For these reasons, surfaces and interfaces have drawn increased attention for chemical and biological processes in research and development (R&D).

With the invention of various surface science techniques, the horizon of knowledge about surface chemistry has been expanded. Expansion of knowledge demands further development of

surface characterization techniques and better understanding of the properties of the surfaces and interfaces. Therefore, the use of surface science and surface analytical techniques can provide essential insights in characterizing and better understanding different aspects of chemical reactions including catalysis where traditional methods are not always successful. Perhaps the most widely quoted motivation for modern surface science studies is the goal of understanding heterogeneous catalysis.

1.1.2 Catalysis

The name 'catalysis' was coined by Berzelius in 1836 from the Greek word 'katalusis', which has the sense of 'down' and 'loosen'. In general, a catalyst is a chemical entity which changes the rate a of chemical reaction without being consumed itself at the end of the reaction.[3] It is commonly said that a catalyst works by lowering the activation energy of the reaction (E_a in figure 1-1); however, in most cases, it actually opens an alternative reaction pathway that is sometimes more complicated, but the highest activation barrier in the catalytic pathway is still lower than that of the non-catalytic one.[4] Catalysts can be divided into two groups: homogeneous and heterogeneous catalysts. In homogeneous catalysis the catalysts and the reactants are in the same phase, either gas or liquid, whereas in the heterogeneous systems the catalysts and the reactants exit in different phases. The latter case has the advantage that, by the end of the reaction the catalyst can often be removed by simple filtration.[5]

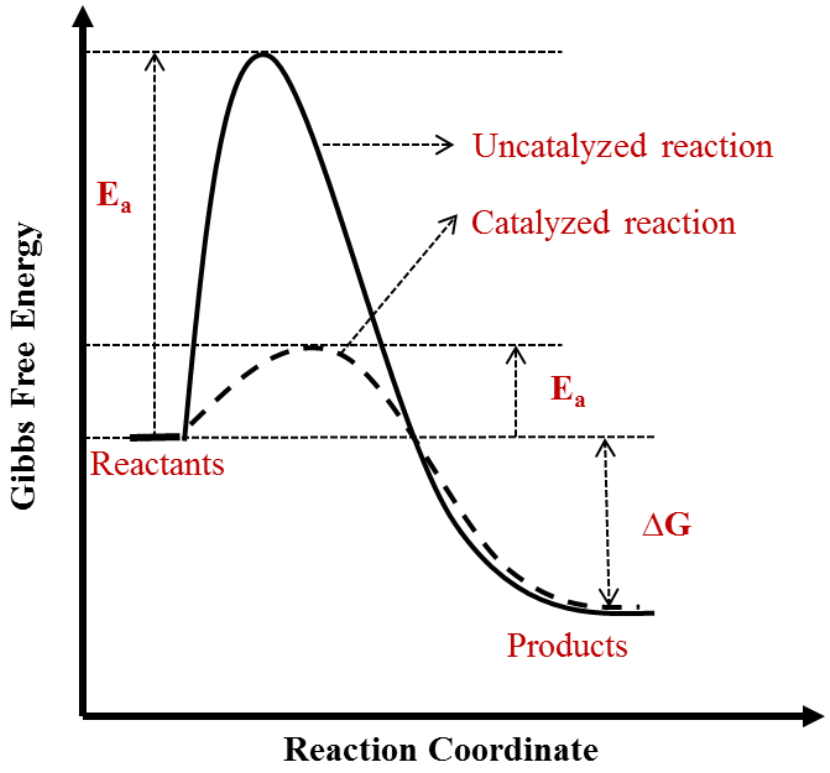

Figure 1.1: Energy diagram of catalyzed and uncatalyzed reactions.

1.1.3 Use of Transition Metals in Catalysis

Transition metal catalyzed reactions have been reported as early as 150-years ago, such as stoichiometric metal-promoted homocouplings.[6 7] During the second half of the 20th century, the use of transition metals as catalysts became important in organic synthesis.[8] The use of these metals has revealed the path to the development of a large number of transition-metal-catalyzed reactions for the synthesis of complex organic molecules, including fine chemicals and C-C bonds.[9 10] Due to their ability to activate various organic compounds, transition metals have been used for the formation of new bonds. The increased possibility for coordination of ligands as a

result of the access to partially filled d-orbitals makes transition metals more versatile than the main group metals in a catalytic sense. The partial occupation of d-orbitals helps the transition metals to act as a sink for ligands, either supplying or accepting electron density.[11]

1.1.4 Palladium as Catalyst

Palladium (Pd) is considered a useful and versatile catalyst among many other transition metals in organic synthesis because of its abundance of possibilities of carbon-carbon bond formation. The importance of C-C bond formation is unquestionable. Since the discovery of cross-coupling reactions catalyzed by palladium in the 1970s, these reactions have become extremely important techniques for forming C-C, C-N, and C-O bonds by chemists.[9] [10] Furthermore, Pd catalysts and reagents show a great tolerance of many functional groups such as carbonyl and hydroxyl groups. Interestingly, from the discovery of palladium in 1802 by Wollaston until the middle of the 20th century, the chemistry of palladium remained dwarfed by the presence of other transition metals, namely platinum and nickel. After World War II, demand increased for cheap sources of plastic and fine chemicals. As part of this research effort, the discovery of the Wacker process (scheme 1-1) – which began as the pursuit to synthesize ethylene oxide from ethylene - in which ethylene is oxidized to acetaldehyde by air in a palladium (palladium on charcoal) catalyzed reaction, stimulated research into the use of palladium in organic chemistry.[12] Hafner *et al* and Tsuji *et al* are considered the pioneers of using palladium in organic synthesis.[12] [8]

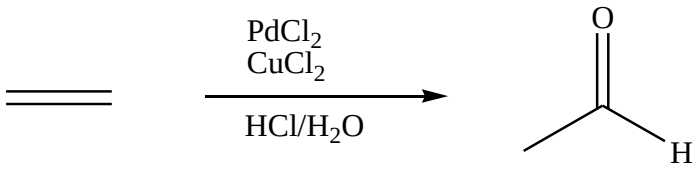

Scheme 1-1: Synthesis of acetaldehyde from ethylene by Wacker process.

Subsequently, interesting developments in the area of palladium catalyzed coupling chemistry were reported by Heck[13] (1968, aryl palladium chemistry, $Li_2[PdCl_4]$), Fitton[14] (1968, oxidative addition of aryl halide, Pd^0-$[PPh_3]_4$), and Mizoroki[15] (1971, coupling reaction of aryl halide with alkenes, Pd(II) complex), who opened up the future of palladium as an important transition metal for catalysis.

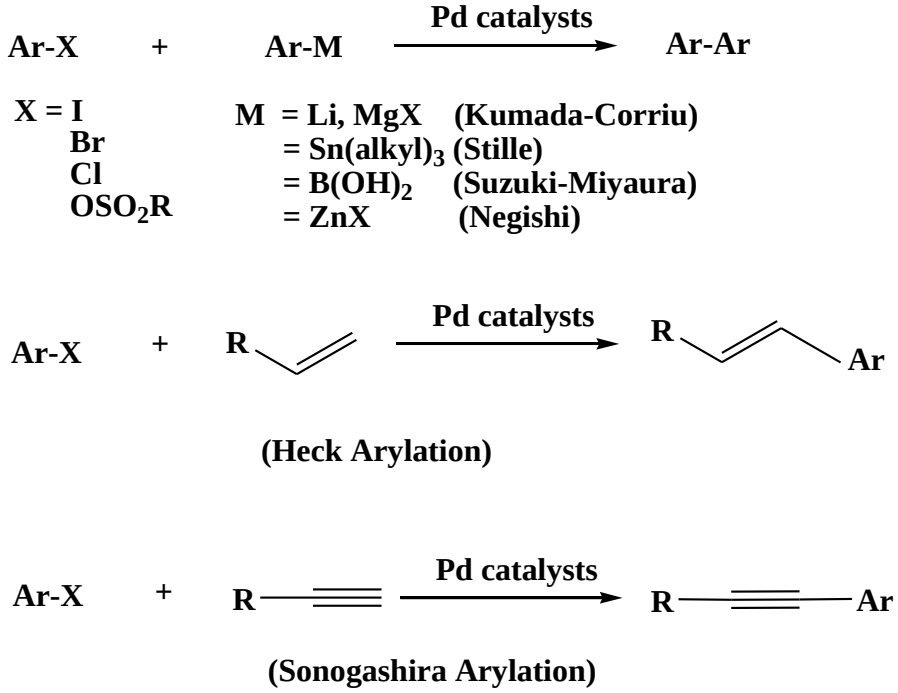

Scheme 1-2: General palladium catalyzed reactions.

Later on, Sonogashira (1975, palladium-catalyzed coupling of acetylenes), Corriu-Kumada (1975, cross-coupling of aryl halide and Grignard reagents, $Pd[PPh_3]_4$), Negishi (1979, organialuminum), and Suzuki-Miyaura (1979, coupling of aryl halide and organo baron compounds, $Pd(PPh_3)_4$ made significant progress in this area, and therefore palladium catalyzed coupling reactions are now well-established.[10]

1.2 The Suzuki-Miyaura Reaction

The Suzuki-Miyaura reaction, which refers to the Pd-catalyzed cross-coupling of aryl or alkyl halides with boranes or boronic acid derivatives, is considered as one of the most important C-C bond forming procedures available in organic chemistry.[16] [10]

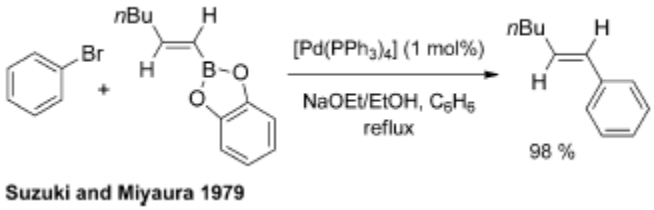

Scheme 1-3: Palladium catalyzed Suzuki-Miyaura reaction.[10]

In 2010, the Nobel prize in chemistry was awarded to Akira Suzuki, Ei-ichi Negishi, and Richard Heck in recognition of the palladium catalyzed C-C bond forming reactions. The basic mechanism of the Suzuki-Miyaura reaction, not very different from most transition-metal cross–coupling reactions, is outlined in figure 1-2. The reaction consists of three steps. The first step is the oxidative addition of an electron-rich Pd^0, usually ligated to an aryl halide, and the second is the transmetalation of the arylboron species to the oxidative addition product.

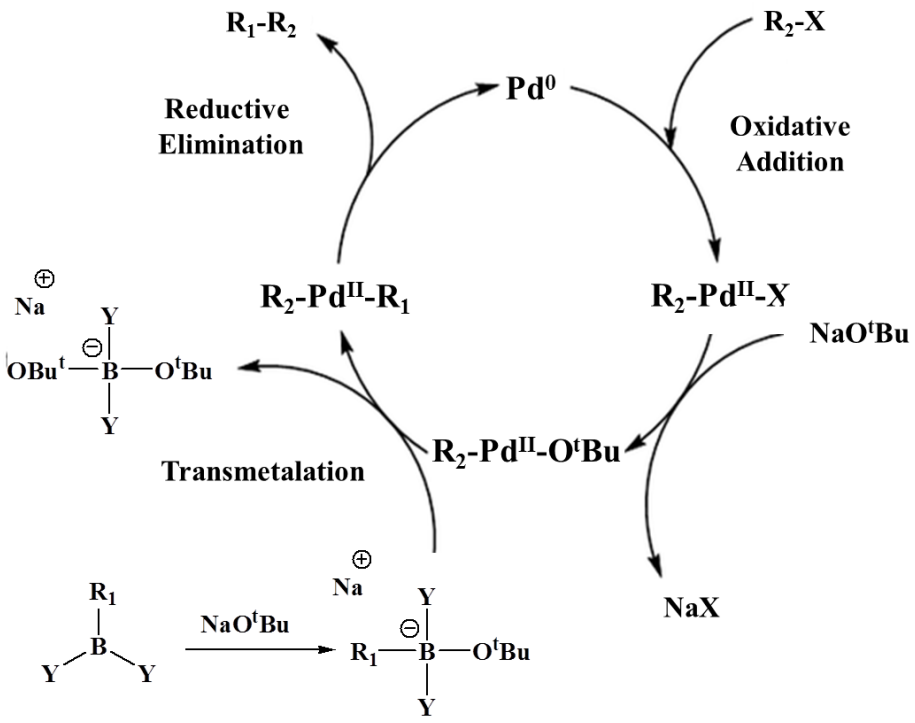

Figure 1-2: Mechanism of Suzuki-Miyaura reaction.

The third step is the reductive elimination of the diarylated Pd, forming the new biaryl C-C bond with releasing Pd^0 catalysts. This mechanism is well accepted in the scientific community. Although the process seems fairly straight-forward, it actually results from a series of complicated events, some of which are not fully understood yet. Indeed, for heterogeneous catalysts, the role of Pd(II) and Pd(0) in the catalytic mechanism, like which one is the active part of the catalysts and the critical role of the tethering ligand (here 3-mercaptopropyltrimethoxy silane), warrant further comment.

1.3 Transition metal nanoparticles

In 1959, Richard P. Feynman, the world renowned physicist, gave a speech entitled "There's Plenty of Room at the Bottom". The speech is considered as the first one which publicly described the manipulation of matter on a tiny scale.[17] He showed the dream of writing 24 volumes of the Encyclopedia Britannica on the head of a pin. Five decades later, Feynman's speech has become more of a reality; significant advances in the field of nanotechnology have been made. The word nano comes from the Greek word 'nanos', which means 'dwarf' or extremely small, an order of magnitude: one billionth of something, in its modern scientific sense. In an example of daily life, the diameter of a human hair is 50,000 nanometers. So, nano-sized structures are incredibly small. Nanomaterials are the particles with a size range of 1 nm to 100 nm.[18] Nanoparticles of less than 10 nm size with near monodispersed distribution have gained a lot attention over the past decades.[19] This interest arises because the nanoparticles are considered to have unique properties which lie somewhere in between those of bulk and the single particles species (Figure 1-3). Ancient peoples believed in 'The Elixir of life'; they thought that a solution of soluble gold could cure many bodily ailments and eventually give them eternal life. Interestingly, researchers have been using gold nanoparticles to combat cancer, catalyse various reactions, and as biological and chemical sensors.

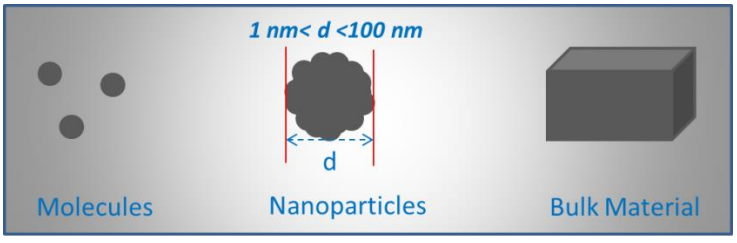

Figure 1-3: Schematic representation of nanoparticles.

1.3.1 History of metal nanoparticles

Though Feynman is credited for first conceiving of nanotechnology, nanoparticles have been around since ancient times. The history of metal nanoparticles goes back to two thousand years ago when soluble Au-NPs were used as pigments for aesthetic and curative purposes. The application of nanoparticles in making ruby glass and for coloring ceramic was found in ancient times, for example, the famous Lycurgus cup in the British Museum (dated 4th century AD).[20] The use of nanoparticles was also found in the time of ancient Rome. At that time, the application was mostly concentrated in decorative purposes. In modern ages, nanoparticles synthesis goes back to about 150 years ago when Graham[21] described the state of inorganic particles in solution, or colloids in 1861. Many methods of synthesizing metal particles have been practised since the first rational synthesis of gold colloids by Faraday[22] in 1857. Faraday demonstrated the formation of AuNPs by reducing tetrachloroaurate $[AuCl_4]^-$ using phosphorous as the reducing agent. In the 1990s this method was popularized by Brust *et al* using $NaBH_4$ as the reducing agent in a two-phase system (organic solvent-water) stabilized by a ligand.[23] There is another early method for NP synthesis named the polyol method: the thermal decomposition of metal(0) precursors in the presence of alcohol as solvent and stabilizing polymers

1.3.2 Palladium Nanoparticles

Though nanoparticles research is primarily focused on coinage metals, mostly those of gold, the interest in the properties of other transition metal nanoparticles is also growing. Palladium nanoparticles are of great importance in the application of catalysis, hydrogen storage, and sensing. Since palladium is one of the most efficient metals in catalysis, synthesis of palladium nanoparticles has been widely studied.[24] Kwangjin *et al* studied the selectivity of the reaction controlled by the size and shape. Due to the high surface area to volume ratio of nanoparticles, they have attracted increasing interest from researchers over the past decade. The key features in producing materials that are more effective and efficient are the preparation of palladium nanoparticles with well-controlled sizes and high monodispersity. C.M. Shen *et. al.* synthesized *n*-octadecayl mercaptan capped Pd nanoparticles.[25] It was reported that 20 min reaction time gave 1.3 nm Pd nanoparticles and with increasing reaction time larger nanoparticles (2.1 nm for 120 min and 5.5 nm for 360 min) were generated.[25] They also controlled the size of the Pd nanoparticles by changing the $Pd/C_{18}H_{37}SH$ molar ratio. In this case, smaller nanoparticles (2.1 nm) with narrow size distribution were synthesized using higher $Pd/C_{18}H_{37}SH$ molar ratio (2:1) and larger Pd nanoparticles with poor dispersion (~5nm) were synthesized using lower $Pd/C_{18}H_{37}SH$ molar ratio (4:1).[25] Reliable synthetic procedures for palladium nanoparticles and study of their properties are prerequisites to the economic use of the valuable metal and sustainable application in the subsequent reaction. A more detailed survey of synthetic methods for Pd nanoparticles will be given in chapter 5.

1.4 N-Heterocyclic Carbene (NHC)

Carbene compounds are neutral species containing a divalent carbon atom bounded by six-electron valency. Among these six electrons, four are involved in σ-bonding and two stay with the central carbon. Carbenes have long being considered as fleeting intermediates since they do not respect to octet rule. In the early 1960s, Wanzlick first attempted to isolate carbenes by α-elimination of chloroform from imidaziline precursors, or by deprotonation of imidazolium salt with a strong base.[26] However, the first reported stable carbene was documented by Bertrand et al in 1988, who described the synthesis of phosphinosilylcarbene.[27] In 1991, the successful synthesis (stability, isolation, and storability) of the first crystalline carbenes were reported by Arduengo, a so-called N-heterocyclic carbene (NHC).[28] In the past two decades, the chemistry of NHCs has witnessed a great development.[29] NHCs have become versatile ligands for transition metals as well as used as powerful organic catalysts in molecular chemistry.

NHC have become valuable donor ligands in transition metal-mediated catalysis and organocatalysis such as C-H activation and C-C bond formation.[30] Unlike phosphine ligands, carbenes are resistant to degradation at high temperature because the lone pair of carbenes forms strong σ-bonds to metals. In transition metal catalysis, NHCs have been shown to be versatile and tunable ligands that may change the mechanistic pathway or control the selectivity of the electrophilic metal atoms via simple modification to substituents.[31] Therefore, NHC-stabilized nanoparticles would expect to possess similar catalytic activity.

1.5 Research Work

Over the last few decades, palladium-catalyzed coupling reactions have gained particular attention for their role in the synthesis of fine chemicals and pharmaceutical ingredients. Using palladium catalyzed coupling reactions in the pharmaceutical industry offers some advantages such as the mild reaction conditions and relatively non-toxic nature of the compounds used. However, while soluble Pd complexes are commonly used as catalysts, their efficient separation after reaction for subsequent recycling remains a challenge and has economic and environmental implications.[32] This is a significant problem for the pharmaceutical industries because strict guidelines are followed to limit the levels of heavy metals, including palladium, in products for human consumption, especially in drugs.[32a]

Several purification methods such as distillation or adsorption on to a solid have been developed to separate palladium from pharmaceutical ingredients but none of these have been highly effective because of the property of the final products. For example, distillation could be used to separate the final products from reaction mixture since palladium is not volatile; however, as many pharmaceutical ingredients are also not highly volatile there is a chance of agglomeration and degradation of the products at high temperature. Converting homogeneous catalysts to a heterogeneous one offers the advantage of easy separation by simple filtration.[32b,33] Researchers have taken several approaches to the development of heterogeneous catalysts, such as adsorption of the metal on an inorganic solid support or incorporation of palladium into mesoporous silica, and these catalysts were applied in organic reactions.[34] But they did not

behave as true heterogeneous catalysts because they first dissolve in the reaction and after the reaction they tend to return to the support. Therefore, this kind of release and return process leads to the inactivation of the catalysts. Another strategy, which is considered as more promising, was reported by Jacobs and Jones: there they first attached a suitable ligand to the support, then bound the metal with the ligand.[35] These catalysts were used in Mizoroki-Heck reactions, but leaching of Pd from the pre-catalysts was reported. Shimizu, Davis and Crudden have successfully developed thiol functionalized mesoporous silica supported Pd catalysts.[36] These catalysts were applied in organic coupling reactions, and showed good catalytic activity with low level of palladium leaching in repeated usages.

Despite the omnipresence of the Suzuki-Miyaura reaction, and even with the rigorous footprint provided to it by a generation of modification and improvement[37], there still remain some major shortcomings. In terms of catalysis, there are many general theories available regarding homogeneous catalysts, and about how they work, however regarding heterogeneous catalysts a general protocol is still lacking. Furthermore, as the Suzuki-Miyaura reaction is currently used in the synthesis of many molecules, including molecules for human consumption, special measures need to be taken to remove the remaining Pd from the final product which cost time and money.[32a] Though advances made in the field of heterogeneous catalysis have greatly lowered the amount of Pd that is ultimately leached into solutions, by developing recyclable and supported Pd catalysts, the modes of action need to be better understood to allow for further improvement.

There have been a few surface science studies of heterogeneous Pd catalysts for coupling reactions[38,39,40] and palladium nanoparticles. A systematic characterization of model heterogeneous Pd catalysts and palladium nanoparticles, and investigation of the electronic properties of their surfaces using surface science techniques, has not been completely done. These represent a significant gap in our knowledge of the active part of the catalyst, and catalyst deactivation. There has been considerable speculation in the literature as to the mechanism of the coupling reactions; the active part of palladium catalysts, Pd(0) or Pd(II). Clearly, a systematic study of palladium catalysts and palladium nanoparticles using surface science techniques could help answer such questions.

One particular challenge, when dealing with mesoporous silica supported palladium catalysts, is that due to the typical porous structure of the mesoporous silica it is not always possible to investigate the surface chemistry taking place deep within the pores. A model heterogeneous palladium catalyst made by immobilizing palladium on a functionalized silicon wafer offers the advantage of easy characterization by modern surface science techniques. Here, X-ray photoelectron spectroscopy (XPS) and related theories are applied to better understand the nature of the catalytic activity of the model system. In addition, AFM and SEM have been used to acquire complementary information about the surface topography of the catalyst.

Following an outline of the experimental methods in chapter 2, the procedures used to clean and functionalize the silicon wafer surfaces which acts as a support for the Pd catalysts are outline in Chapter 3. Chapter 4 describes a systematic surface science study of a model

heterogeneous palladium catalyst. The primary goal was to reproduce and further study the thiol functionalized mesoporous silica supported palladium (SBA-15-SH-Pd) catalysts results of McEleney *et al*[39] and MacQuarrie *et al*[38] through developing a model system. The model system mimics the real catalysts,SBA-15-SH-Pd, but offer the advantage of characterizing with modern surface science techniques.

Chapter 5 describes the application of surface science techniques to better understand the synthesis and electronic properties of palladium nanoparticles. Nanoparticles have tremendous potential use in catalysis, medical chemistry, sensors, hydrogen storage, and electronics.[24] Whatever the application might be, the size of the nanoparticles plays key role. A high surface-to-volume/area ratio of nanoparticles makes them a very economic candidate in catalysis application. The use of XPS in nanoparticle characterization is not reported in the literature very often and limited to confirm the formation of palladium nanoparticles by observing a Pd 3d peak at 335.0 eV regions. The XPS can also be used to confirm the presence of stabilizing agents present on the surface of the nanoparticles. By using the XPS and the Auger data in the Wagner plot, information regarding the size of the particles can also be acquired. The main focus of this work is to synthesize different sizes of palladium nanoparticles and characterize those by XPS and related concepts including Auger parameter and Wagner plot concept to better understand how the electronic properties of palladium nanoparticles change with their size. The properties of nanoparticles can be tuned by changing the capping agents.

Chapter 6 describes the substitution of the stabilizing agent of Pd nanoparticles by N-heterocyclic carbene (NHC). Recently, NHCs have been successfully used on gold surface to form an ultra-stable self-assembled monolayer (SAM).[41] Here, we report for the first time on the formation of NHC SAMs on Pd. This chapter highlights the methods and the ability of NHCs to replace the dodecyl sulfide stabilizing agent from the Pd nanoparticle surfaces.

In summary, the work presented in this thesis details recent developments in the area of surface modification, supported palladium catalysts for Suzuki-Miyaura reactions, synthesis of palladium nanoparticles, and alteration of nanoparticle properties by substitution of stabilizing agents. The XPS has been extensively used to characterize the functionalized silica supported Pd catalysts and Pd nanoparticles. Auger parameters and Wagner plots gave valuable information to identify the chemical state of Pd. The model Pd catalysts design showed that there are two types of active Pd present on the catalysts surface; one of them found to be more active than the other. However, relatively less active Pd species were found to be more stable in the reaction condition. Using surface science techniques in the model system helps identifying a sulfur species that has not previously reported in this type catalyst, Different sizes of Pd nanoparticles were synthesized and characterized by XPS and TEM. The XPS has been found to be an useful instrument to critically analyze Pd nanoparticles.

1.6 References

(1) Somorjai, G. A.; Li, Y. M. *PNAS* **2011**, *108*, 917.

(2) McCash, E. M. *Surface Chemistry*; Oxford University Press, 2001.

(3) Sinfelt, J. H. *Surface Science* **2002**, *500*, 923.

(4) Rothenberg, G. *Catalysis – Concept and Green Applications*; Wiley-VCH, 2008.

(5) Mehnert, C. P.; Weaver, D. W.; Ying, J. Y. *J. Am. Chem. Soc.* **1998**, *120*, 12289.

(6) Glaser, C. *Ber. Dtsch. Chem. Ges* **1869**, *2*, 422.

(7) Glaser, C. *Ann. Chem. Pharm.* **1870**, *154*, 137.

(8) Tsuji, J.; Takahash.H; Morikawa, M. *Tetrahedron Lett.* **1965**, 4387.

(9) de Meijere, A.; Diedrich, F. *Metal-Catalyzed Cross-Coupling Reactions*; 2nd ed.; Wiley-VCH: Weinheim, 2004.

(10) Seechurn, C.; Kitching, M. O.; Colacot, T. J.; Snieckus, V. *Angew. Chem. Int. Ed.* **2012**, *51*, 5062.

(11) Hegedus, L. S.; soderberg, B. C. G. *Transition Metals in the Synthesis of Complex Organic Molecules*; University Science Books: Sausalito, California

2010.

(12) Smidt, J.; Hafner, W. *Angew. Chem. Int. Ed.***1959**, *71*, 284.

(13) Heck, R. F. *J. Am. Chem. Soc.* **1968**, *90*, 5518.

(14) Fitton, P.; Johnson, M. P.; McKeon, J. E. *Chem. Commun.* **1968**, 6.

(15) Mizoroki, T.; Mori, K.; Ozaki, A. *Bull. Chem. Soc. Jpn.* **1971**, *44*, 581.

(16) Miyaura, N.; Yamada, K.; Suzuki, A. *Tetrahedron Lett.* **1979**, *20*, 3437.

(17) Feynman, R. P.; Caltech Engineering and Science, 1960; Vol. 23:5.

(18) Roduner, E. *Nanoscopic Materials Size-dpendent Phenomena*; The Royel Society of Chemistry: Cambridge, 2006.

(19) Aiken, J. D.; Finke, R. G. *J. Mol. Catal.A-Chem.* **1999**, *145*, 1.

(20) Daniel, M. C.; Astruc, D. *Chem. Rev.* **2004**, *104*, 293.

(21) Graham, T. *Philos. Trans. R. Soc.* **1861**, *151*, 183.

(22) Faraday, M. *Philos. Trans. R. Soc.* **1857**, *147*, 145.

(23) Brust, M.; Walker, M.; Bethell, D.; Schiffrin, D. J.; Whyman, R. *J. Chem. Soc.-Chem. Commun.* **1994**, 801.

(24) Cookson, J. *Platinum Met. Rev.* **2012**, *56*, 83.

(25) Shen, C. M.; Su, Y. K.; Yang, H. T.; Yang, T. Z.; Gao, H. J. *Chem. Phys. Lett.* **2003**, *373*, 39.

(26) Wanzlick, H. W. *Angew. Chem. Int. Ed. Engl* **1962**, *1*, 75.

(27) Igau, A.; Grutzmacher, H.; Baceiredo, A.; Bertrand, G. *J. Am. Chem. Soc.* **1988**, *110*, 6463.

(28) Arduengo, A. J.; Harlow, R. L.; Kline, M. *J. Am. Chem. Soc.* **1991**, *113*, 361.

(29) Fevre, M.; Pinaud, J.; Gnanou, Y.; Vignolle, J.; Taton, D. *Chem. Soc. Rev.* **2013**, *42*, 2142.

(30) Herrmann, W. A. *Angew. Chem. Int. Ed.* **2002**, *41*, 1290.

(31) Marion, N.; de Fremont, P.; Lemiere, G.; Stevens, E. D.; Fensterbank, L.; Malacria, M.; Nolan, S. P. *Chem. Commun.* **2006**, 2048.

(32) (a) Garrett, C. E.; Prasad, K. *Adv. Synth. Catal.* **2004**, *346*, 889(b) Polshettiwar, V.; Molnar, A. *Tetrahedron* **2007**, *63*, 6949.

(33) Jas, G.; Kirschning, A. *Chem. Eur. J.* **2003**, *9*, 5708.

(34) Yin, L. X.; Liebscher, J. *Chem. Rev.* **2007**, *107*, 133.

(35) (a) De Vos, D. E.; Dams, M.; Sels, B. F.; Jacobs, P. A. *Chem. Rev.* **2002**, *102*, 3615(b) Weck, M.; Jones, C. W. *Inorg. Chem.* **2007**, *46*, 1865.

(36) (a) Shimizu, K.; Koizumi, S.; Hatamachi, T.; Yoshida, H.; Komai, S.; Kodama, T.; Kitayama, Y. *J. Catal.* **2004**, *228*, 141(b) Ji, Y. Y.; Jain, S.; Davis, R. J. *J. Phys. Chem. B* **2005**, *109*, 17232(c) Crudden, C. M.; Sateesh, M.; Lewis, R. *J. Am. Chem. Soc.* **2005**, *127*, 10045(d) Crudden, C. M.; McEleney, K.; MacQuarrie, S. L.; Blanc, A.; Sateesh, M.; Webb, J. D. *Pure Appl. Chem.* **2007**, *79*, 247(e) Webb, J. D.; MacQuarrie, S.; McEleney, K.; Crudden, C. M. *J. Catal.* **2007**, *252*, 97.

(37) Miyaura, N.; Suzuki, A. *Chem. Rev.* **1995**, *95*, 2457.

(38) MacQuarrie, S.; Horton, J. H.; Barnes, J.; McEleney, K.; Loock, H. P.; Crudden, C. M. *Angew. Chem. Int. Ed.* **2008**, *47*, 3279.

(39) McEleney, K.; Crudden, C. M.; Horton, J. H. *J. Phys. Chem. C* **2009**, *113*, 1901.

(40) MacQuarrie, S.; Nohair, B.; Horton, J. H.; Kaliaguine, S.; Crudden, C. M. *J. Phys. Chem. C'* **2010**, *114*, 57.

(41) Crudden, C. M.; Horton, J. H.; Ebralidze, I. I.; Zenkina, O. V.; McLean, A. B.; Drevniok, B.; She, Z.; Kraatz, H.-B.; J.Mosey, N.; Seki, T.; Keske, E. C.; Leake, J. D.; Rousina-Webb, A.; Wu, G. *Nat. Chem.* **2014**, *6*, 409.

Chapter 2

Experimental Methods

The principal experimental methods applied in the work described in this thesis are introduced. In particular, X-ray photoelectron spectroscopy (XPS) is dealt with in some detail because it has been the main instrument/tool used for all the studies presented in the following chapters. Other techniques and related theories, which I have used during my doctoral study, are also briefly introduced.

2.1 X-ray Photoelectron Spectroscopy (XPS)

The technique of X-ray photoelectron spectroscopy (XPS), also known as electron spectroscopy for chemical analysis (ESCA), was developed by Kai Siegbahn while he was working in Uppsala. Kai Siegbahn was awarded the Nobel Prize in 1981 for this contribution. The XPS has been considered as one of the major techniques for characterizing/ analysing thin films, solids, and surfaces.[1] XPS is used to study the binding energy of core level electrons in an atom and changes in the binding energy due to the atoms being in different chemical environments. XPS also provides information of surface chemical composition and the chemical state of the elements in a sample. Figure 2-1, is the schematic representation of the XPS system.

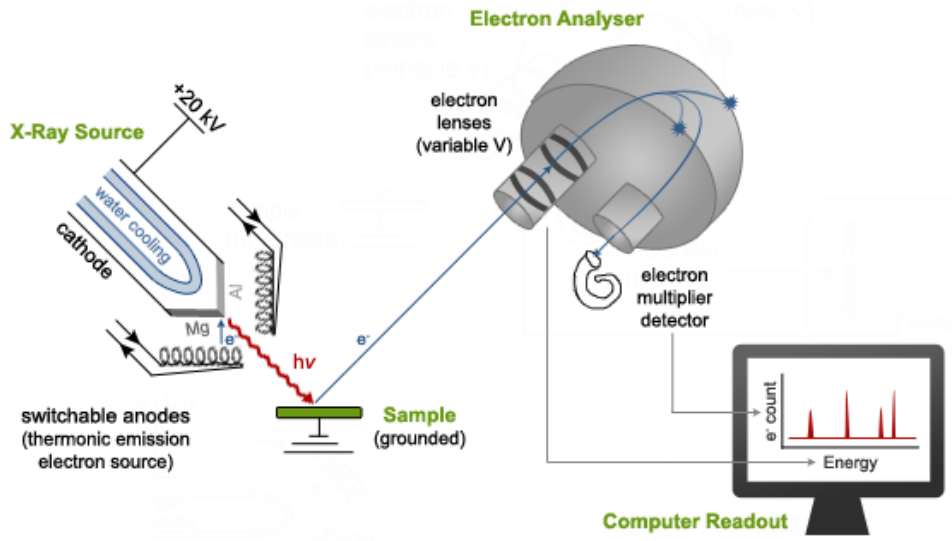

Figure 2-1: A schematic representation of an X-ray photoelectron spectrometer. (Courtesy of Dr. J.H. Horton, Queen's University, Department of Chemistry)

2.1.1 Physical Principles

The XPS experiment involves the bombardment of a sample surface with X-rays under ultra-high-vacuum (10^{-9} torr). The incident X-ray is capable of penetrating many micrometers into the bulk. The XPS process is presented schematically in figure 2-2. The atoms in the material excited by the X-ray lead to ejection of electrons (photoionisation) either from core levels or from valence levels. Electrons generated close to the surface are prone to escape into the vacuum, in the form of photoelectrons. The overall process is known as the photoelectric effect. The photoelectric effect was coined by Heinrich Hertz in 1887 while he produced an electric current in a photocell by simply illuminating the cathode with light of sufficiently short wavelength.[2] Therefore, in the XPS technique, an atom absorbs photon energy ($h\upsilon$), then a core

or valence electron having different binding energy (E_{BE}) is ejected with a particular kinetic energy (E_{KE}), can be written as-

$$E_{BE} = h\upsilon - E_{KE} - \varphi \qquad (2\text{-}1)$$

where,

E_{KE} is the kinetic energy of the photoelectron;

h is the Planck's constant;

υ is the frequency of the exciting radiation;

E_{BE} is the binding energy of the photoelectron with respect to the Fermi level of the sample;

φ is the work function of the spectrometer

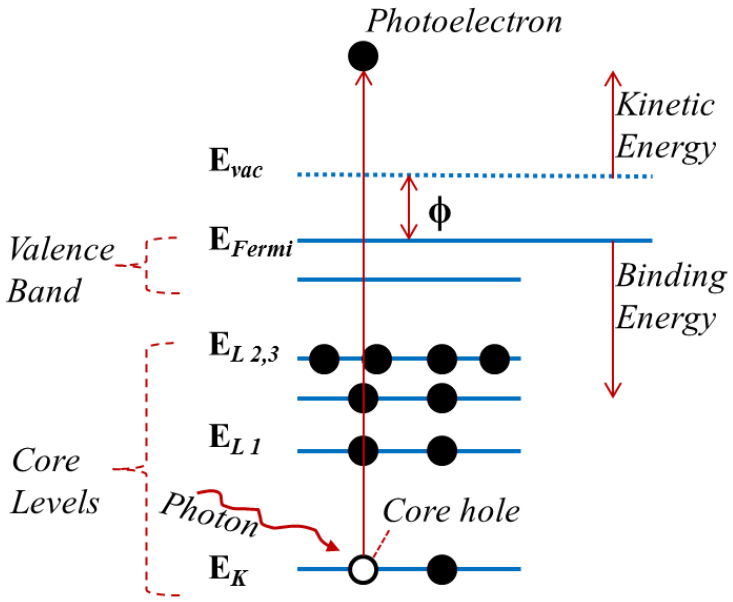

Figure 2-2: Schematic representation of XPS process.

The photoelectrons are energy analyzed and represented as a spectrum of electron intensity as a function of energy. In the XPS spectrum, the peak intensity depends on the density of state, the transition probability, the ionization site, and the electron mean free path of the electron in the solid. The relative peak intensities/peak areas can be calculated for quantitative analysis of the sample surface stoichiometry. More details of the XPS are available in the literature.[1] Here, several topics related to the current research are discussed in detail.

2.1.2 Core Levels Peaks and Spin-orbit splitting

Core level peaks are named as nl_j where n is the principle quantum number, l is the orbital angular momentum, and j is the total angular momentum quantum number. Here the total angular momentum, $j = (l \pm s)$ and s denotes the spin angular momentum quantum number. The atomic notation of core level peaks and the spin-orbit splitting are shown in figure 2-3.

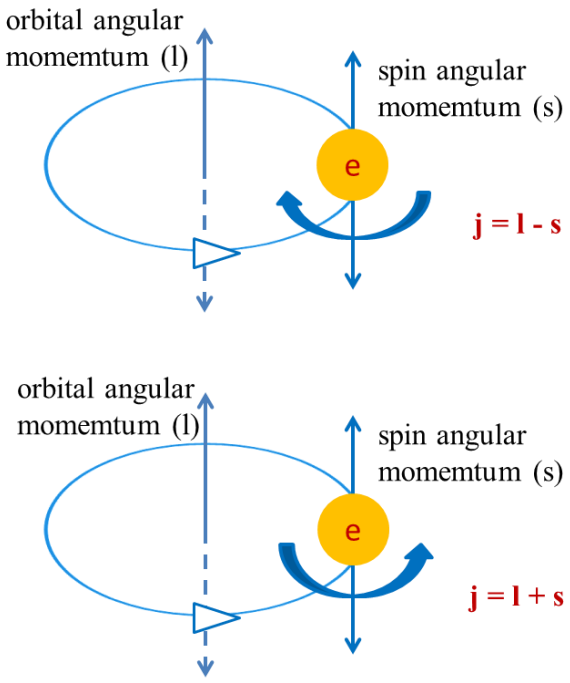

Quantum numbers				Atomic notation	X-ray notation
n	l	s	j		
1	0	± ½	1/2	1s	K_1
2	0	± ½	1/2	2s	L_1
2	1	± ½	3/2	$2p_{3/2}$	L_2
2	1	± ½	1/2	$2p_{1/2}$	L_3
3	0	± ½	1/2	3s	M_1
3	1	± ½	1/2	$3p_{1/2}$	M_2
3	1	± ½	3/2	$3p_{3/2}$	M_3
3	2	± ½	3/2	$3d_{3/2}$	M_4
3	2	± ½	5/2	$3d_{5/2}$	M_5

Figure 2-3: A schematic representation of spin-orbit splitting process. The double ended arrows in the spin angular momentum (s) indicating the parallel and anti-parallel vector to the orbital angular momentum.

For *s* levels (when l = 0) singlet core level peaks are generated whereas all other levels (*p*, *d*, *f*,..) (when l >0) doublet core level peaks are generated. The unpaired electron left behind due to photoionization may have orbital angular momentum and spin angular momentum vectors either parallel or anti-parallel, resulting in two possible states with different energies and giving peaks at different positions. This is known as spin-orbit splitting or multiplet splitting. This is an initial state effect. For this reason, sometimes two peaks are observed for one element. In that case, the high intensity peak is usually considered for further analysis. Examples of spin-orbit splitting are discussed in the following chapters.

2.1.3 X-ray Satellite Peaks

In photoelectron spectra, some extra features are frequently observed. These are known as satellite peaks, usually found on the high binding energy side of a main peak. When a core electron is removed by photoionization, equivalent nuclear charge is increased to the valence electrons.[1] There is a substantial reorganization of valence electrons due to this major perturbation. This may lead to a transition of an electron from a bonding orbital to an anti-bonding orbital simultaneously with core ionization. The photoelectron electron on its way out interacts with a valence electron and excites it to a higher energy level. Due to this interaction, the photoelectron's energy is reduced. According to equation 2-1, KE will give a XPS peak at higher BE and generally the satellite peak appears a few eV above (BE scale) the core electron position. For example, in figure 2-4, satellite peaks of silicon (Si) are observed at higher binding energy position than that of core Si XPS peak. This type of peak is called shake-up satellite peak.

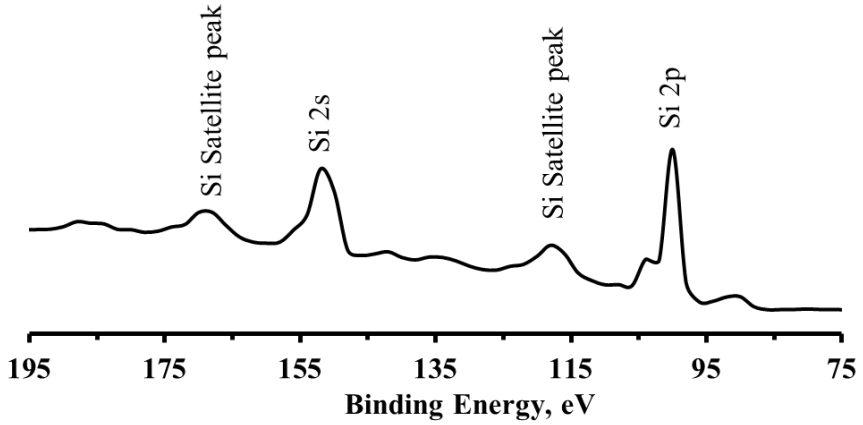

Figure 2-4: XPS satellite peak of a Si wafer surface.

There is another type of satellite peak known as the shake-off satellite peak. These result when the valence electron is ejected from the ion completely to the continuum, those appear as a broadening of the core level peak or contribute to the inelastic background.

2.1.4 Chemical Shifts

The chemical shift is one of the most important features of XPS by which it can discriminate between oxidation states and chemical environments. The chemical shifts can be defined as the core level binding energy shift due to the changes of chemical state, local environment, and potential of the atom. The chemical shift may be used to obtain information on how the atoms are chemically bound in a system. Chemical shifts are readily observable and interpretable in the XPS spectra because of: (1) their high intrinsic resolution since core levels are discrete and generally of a well-defined energy, and (2) simplifying interpretation due to one-electron process. The extra coulombic interaction between photoemitted electron and the ion core of atoms with higher oxidation state exhibit a higher binding energy. Figure 2-5, shows the XPS peak of palladium (Pd 3d).Two states of palladium have been recorded; one at around 338.0 eV represents the presence of Pd^{II} oxidation state and another peak at around 335.5 eV proves the presence of Pd^{0} oxidation state in the sample surface region. The chemical shift is also affected by some other aspects, as will be discussed momentarily .

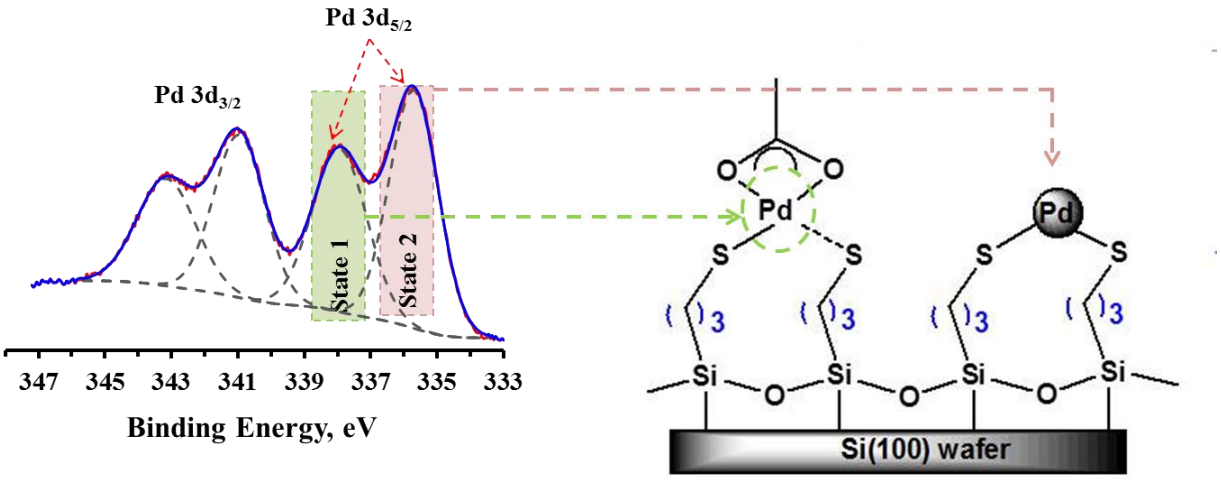

Figure 2-5: Chemical shift of Pd 3d due to the presence of Pd^{II} and Pd^{0} oxidation states.

2.2 Auger Electron Spectroscopy (AES)

The Auger electron spectroscopy (AES) technique was discovered by Pierre Auger in the 1920s. AES is a standard analytical tool in surface science, and detailed explanations of this technique and application may be found in the literature.[1] However, a brief account is given here. AES is used for determining the elemental composition of the first few atomic layers of a solid surface. The AES and XPS processes are related as is shown in figure 2-6. In the Auger process, an excited atom with a core hole in its shell *A* tends to relax to attain an energetically lower state. The core hole in the *A* shell is filled by an electron from an outer shell *B*. This electron is emitted and carries excess energy as kinetic energy which is sufficient to ionize another electron from shell *C*, given by

$$E_{KE} = E_A - E_B - E_C. \qquad (2\text{-}2)$$

Where, E_{KE} is the kinetic energy of the Auger electron and E_A, E_B, and E_C represent the energy of the shell A, B, and C respectively.

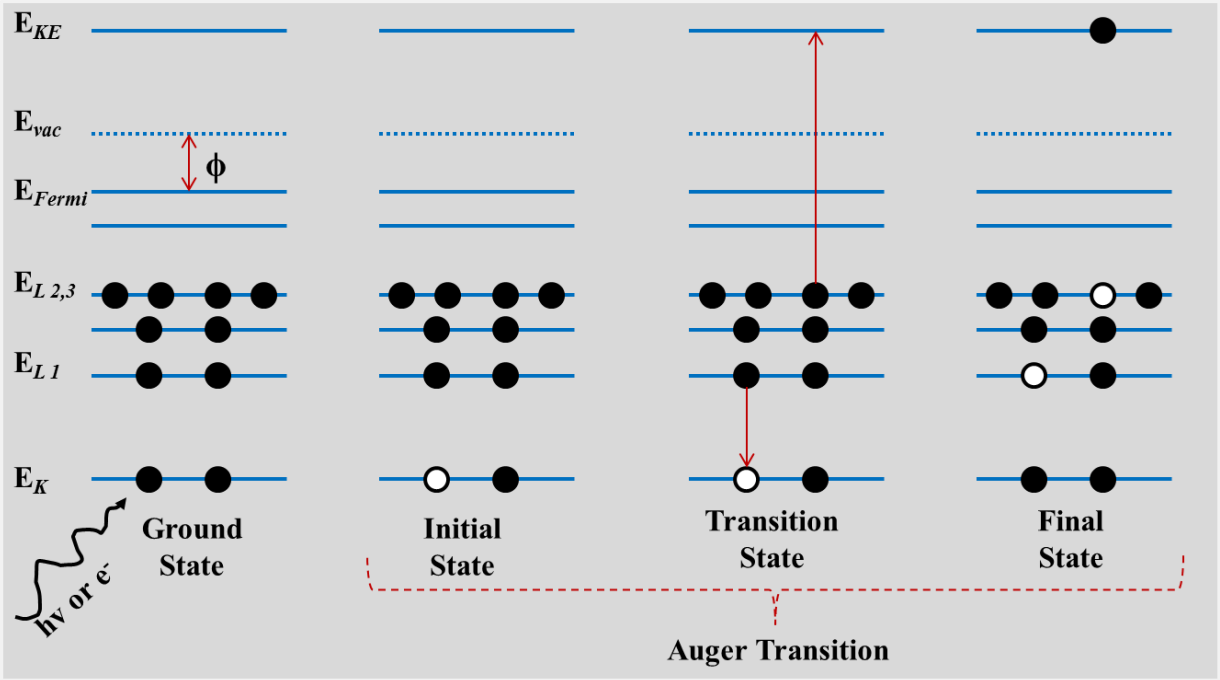

Figure 2-6: Schematic representation of Auger process of KLL transition. The core hole in K is filled by an electron from L in the transition state. The excess energy is sufficient enough to eject another L electron from the atom.

2.2.1 Nomenclature of Auger peak/ Auger transition

In the Auger transition, three atomic levels are involved and the nomenclature reflects this. Auger transitions are generally identified with nomenclature like $X_AY_BZ_C$ where X, Y, and Z are the spectroscopic terms refer to the principle quantum numbers (K, L, M etc.) while *A*, *B*, and *C* denote the standard spectroscopic terms used in j-j coupling (1= s, 2= $p_{1/2}$, 3= $p_{2/3}$, 4= $d_{3/2}$ etc). In the example in figure 2-6, the Auger process is shown where initial ionization occurs in the K level. Following in levels L_1 and $L_{2,3}$ represent the relaxation and the emission (Auger) of

electrons. Due to the photoionization vacancy that has been created in K level an electron from the L_1 level drops down to fill that vacancy. This process releases energy which is equal to the difference in binding energies of K level and L_1 level. As a result, another electron from the $L_{2,3}$ level is removed. So this transition is named as KLL. In Auger transitions, the energy of the Auger electron depends on the difference between core hole energies and not on the incoming energy that excites electron or photon. As a result, each electron has its own characteristic Auger transitions. Like XPS, AES also an extremely surface sensitive technique. The basic difference between XPS and AES may be explained that XPS is a primary photo-emission processes whereas AES is a secondary relaxation process.

2.2.2 Auger parameter and Wagner Plot

The concept of the Auger parameter was developed by Charles D. Wagner in 1970s.[3] He showed that in the series of NaF, NaCl, NaBr, and NaI, the kinetic energy difference between the Auger electron (KLL) and the Na photoelectron (1s) varied from 574.0 to 576.9 eV, a range 2.9 eV. Wagner described this chemical shift as the measure of the polarizability of the chemical environment of the core-ionized atom.[4] Giuliano Moretti[5] refined the concept, addressing several key points:

(1) the same element in the same sample shows a fixed difference in kinetic energy between the Auger and photoelectron spectra;

(2) an estimation of the Auger parameter makes unnecessary the use of correction for charging effects;

(3) there is no need for work function corrections; therefore direct comparism of Auger parameters between labs becomes possible.

The difference between the kinetic energy of the Auger electron and the kinetic energy of a photoelectron is defined as the Auger parameter and is accurately measurable in the presence of static charging. Therefore, Auger parameters can be used in the characterization of insulators and semiconductor materials.

Initially, the Auger parameter was defined as the kinetic energy differences of Auger and photoelectron peaks of the same elements, measured in the same spectrum[3b], given by

$$\alpha = E_{KE}\,(C'\,C''\,C''') - E_{KE}\,(C) \qquad (2\text{-}3)$$

Where, E_K (C' C'' C''') denotes the Auger electron kinetic energy involving transitions among C', C'' and C''' core levels, and E_K (C) denotes the photoelectron kinetic energy involves core level C. When C is same as either C', C'', **or** C''', the value of α could be negative in equation 2-3. To make it positive, Wagner[3b] arbitrarily added 1000 or 2000 eV. Later on, the Auger parameter was redefined by simply adding the photon energy to α, given by

$$\alpha' = \alpha + h\nu = E_{KE}\,(C'\,C''\,C''') + E_{BE}\,(C) \qquad (2\text{-}4)$$

Where, α' is known as the modified Auger parameter (the term "modified" is not necessarily added in modern use) and the symbol α is often instead used to represent the

polarizability of the chemical species. E_{BE} *(C)* denotes the binding energy of the photoelectron from core level C. Wagner[3b] and Thomas[6] showed in the simplest approximation that the shifts in core ionization energy, ΔE_{BE}, and in the kinetic energy of C' - C'' - C''' Auger transition, ΔE_{KE}, can be given by the following equations

$$\Delta E_{BE} = \Delta\varepsilon - \Delta R^{ea} \qquad (2\text{-}5)$$

$$\Delta E_{KE} = -\Delta\varepsilon + 3\Delta R^{ea} \qquad (2\text{-}6)$$

Where, $\Delta\varepsilon$ represents the change of initial state effect or initial state charge distribution; ΔR^{ea} denotes the final state extra-atomic relaxation or polarization energy resulting from the neighbouring ligands of the core-ionized atom.

The shift in the Auger parameter can be found from these two equations

$$\Delta\alpha' = \Delta E_{BE} + \Delta E_{KE} = 2\Delta R^{ea} \qquad (2\text{-}7)$$

This equation can be used to experimentally measure the polarization energy.

The Auger parameter thus provides analytical results independent of static charge referencing, and still can be considered as a one-dimensional quantity like XPS and Auger data alone. Wagner came with a new approach that encompasses recording the position of the sharpest Auger line and the most intense XPS line of compounds of each element on a two-

dimensional plot, to identify chemical states. Later this became known as a Wagner plot or chemical state plot.[7] The Wagner plot is usually drawn by plotting the kinetic energy of Auger electrons as the ordinate and the corresponding XPS binding energy as the abscissa oriented in the negative direction. The Auger parameter is plotted as diagonal lines with a slope of -1 which represent the changes in final state effects. According to equation (2-7), the compound will reside in the upper part of the Wagner plot if it has higher relaxation energy (final state effect). The initial state effect also determines the position of compounds in the plot. The initial state effect resembles the contribution of the chemical shift of the local valence charge and the local potential at the core ionized atom in the sample materials.[4]

As may be noted from Equation 2-5 (derived above), the observed binding energy shift itself depends on both the aforementioned initial state effect and final state effect [3b] and can be written as,

$$\Delta BE = \Delta\varepsilon - \Delta R^{ea} \qquad (2\text{-}5)$$

Here, $\Delta\varepsilon$ represents the contribution to the binding energy state arising from the initial state effect. The initial state effect is generally associated with the difference in oxidation state and this factor is often mistakenly taken to completely control the binding energy ranges associated with a particular oxidation state of a given element. However, the extra-atomic relaxation or polarizability of the surrounding chemical environment can have a strong influence on the binding energy shift, often in a direction opposite to that of any initial state effect. Therefore any interpretation of a binding energy shift must consider more that a naïve

interpretation based on oxidation state alone, and also account for the polarizability of the surrounding medium. Hence, the use of Wagner plots when interpreting XPS data; these will be used at a number of points throughout this thesis as a means of aiding the interpretation of the photoelectron spectroscopic gathered.

2.2.3 Relaxation Energy in XPS

When a compound is exposed to a high energy photon (such as the Mg Kα X-ray used in XPS), a photoelectron leaves the compound resulting in a core-hole. Upon formation of this positively charged hole, all the electrons from neighbouring orbitals tend to move towards the hole to be relaxed. The relaxation energy is entirely transferred to the outgoing photoelectron, based on the adiabatic approximation.[4] The relaxation energy can be written as-

$$R(C) = R^{a}\text{ (core electrons)} + R^{a}\text{ (valence electrons)} + R^{ea}\text{ (extra-atomic contribution)}^{4} \quad (2\text{-}8)$$

Where, both R^{a} terms related to the electron density at the core-ionized atom or atomic relaxation energy. R^{a} (core electrons) is independent on the chemical state of the element and is constant. However, R^{a} (valence electrons) is dependent on the chemical state of the element in question both in initial state and final state of the photoemission process, and R^{ea} deals with the contribution of all other atoms in the system of the relaxation process. Therefore, if we consider that the number of valence electrons will remain constant, then the final state relaxation energy will depend necessarily on the dipole polarization or polarizability of the neighbouring ligands of the core-ionized atom.

2.2.4 Local and Non-local Screening Mechanism

In the presence of a core-hole, the polarization of the photoelectron may be accompanied by two main channels: the local and non-local screening mechanism.[8] In the local screening process, electrons from the ligand band tend to go into a localized atomic orbital of the core ionized atom. Late transition metal ions with well localized d orbitals maintain a local screening mechanism. The atomic relaxation energy is large in this electron transfer and due to this the Auger parameter should be independent of the chemical nature of the ligands; while going from one chemical state to another should not change significantly.[4] For non-local screening, the electronic polarizability of the ligands strongly influences the relaxation energy. In this case, with the increase of ligand polarizability the overlap of the ligand orbitals with extended s and p cation orbitals (from the ligand valence orbitals) increases. As a result, with non-local screening the Auger parameter is influenced by the chemical nature of the ligands.

2.2.5 Instrumentation

XPS and AES experiments were carried out using a Thermo Instrument Microlab 310F surface analysis system (Hastings, UK). Mg Kα (1253.6 eV) was used as the X-ray source at 15 kV anode potential and 20 mA emission current. During the experiments ultra-high vacuum (10^{-9} – 10^{-10} torr) was maintained. A Shirley fit algorithm was used for background subtraction and a Powell peak-fitting algorithm for data analysis.

2.3 Atomic Force Microscopy (AFM)

Atomic force microscopy (AFM) is a high resolution imagining technique that is just one of a series of techniques known as scanning probe microscopies (SPM) widely used to resolve features as small as an atomic lattice in the real space. The principle of the AFM technique is inherited from the scanning tunneling microscope (STM), and was invented by G. Binning and H. Rohrer in 1981 who shared the Nobel Prize in physics in 1986 for this invention. Since its invention the AFM has drawn attention to researchers to observe and manipulate molecular and atomic level features. While STM is limited to imaging conducting surfaces only, the AFM has much wider scope and application since it can be used for imaging both conducting and non-conducting surfaces. There are also some other techniques similar to the AFM but they measure different parameters such as magnetic force microscopy (MFM), lateral force microscopy (LFM), or scanning near-field optical microscopy (SNOM), amongst others.

The basic principle of AFM is schematically represented in figure 2-7. The main components of AFM includes a AFM tip mounted on a cantilever (usually made of silicon), a laser source and laser reflection part to measure cantilever deflections generated by interactive force between the sample surface and the tip, a set of piezoscanners, an electron feedback system/ -photodetector, and software to collect and interpret data. In operation, the tip is brought into contact with sample surface and a laser beam is reflected from the opposite side of the cantilever onto a photodetector. The photodetector is a photodiode divided into four parts shown in figure (A, B, C, and D). The deflection signal is detected by measuring the difference between A+B versus C+D. It can measure both lateral and torsional bending of the cantilever. The tip-

sample separation is controlled through a high voltage amplifier and fed to a piezoscanner, that regulates the tip-sample separation. This is done to keep the error signal at zero. The output of this process generates the topographic data of the sample surface. Better control over minimizing deflection or amplitude signal, improve the image quality.

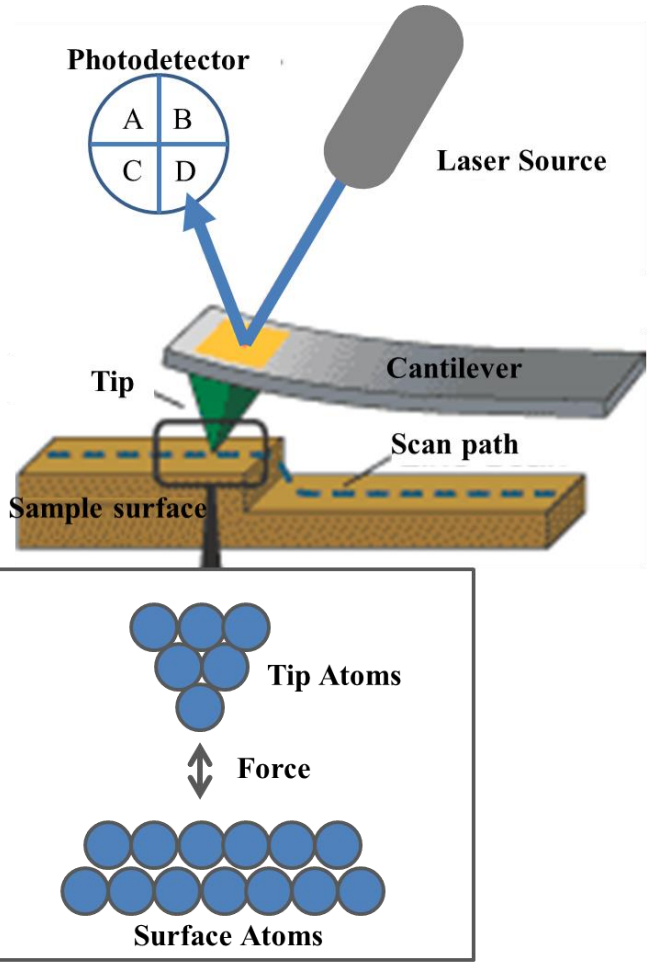

Figure 2-7: Schematic representation of the AFM technique

The AFM has three principle operation modes: contact mode, tapping mode (also known as intermittent contact mode), and non-contact mode. In contact mode, a constant deflection of the cantilever is maintained during scanning by the feedback loop. In this mode, the scanning

area is very small, and tip and surface remain in close contact. Therefore, the chance of damaging the tip and the sample surface is high. In non-contact mode, the cantilever stays close to the sample surface and maintains smaller oscillation amplitude. The non-contact mode is more sensitive than tapping and contact mode that can generate images with atomic resolution. The chances of damaging the tip and the sample are less here. In tapping mode, the cantilever is driven to oscillate near to its resonance frequency.. This mode can generate topographic as well as phase images. Compared to the contact mode, the tip and samples are not easily damaged here.

AFM images were obtained using a Veeco Multimode Microscope equipped with a IIIa controller. All AFM images were acquired under ambient conditions.

2.4 Scanning Electron Microscopy (SEM)

A scanning electron microscope (SEM) is a type of electron microscope that uses a focused beam of high energy electrons to generate a variety of signals at the surface of a sample. These signals of electron-sample interactions reveal information about surface morphology, chemical composition, and orientation of materials of the sample made with. The SEM has a large depth of field that permits more of a sample to be in focus at one time and researchers have more control over the degree of magnification.

principle typical SEM instrument is shown in figure 2-8. In typical SEM operation, a beam of electrons is produced at the top of the microscope by an electron gun. The process needs a high vacuum system. The beam travels through electromagnetic fields and lenses, eventually focused on the sample. Upon hitting the sample, electrons and X-rays are ejected from the sample. These X-rays, backscattered electrons, and secondary electrons are collected by a detector. The detector converts the signals and sent to a screen as image.

Figure 2-8: Representative LEO 1530 FE-SEM system

In this research work, SEM images were acquired using a Zeiss LEO 1530 field emission SEM.

2.5 Transmission Electron Microscopy (TEM)

The transmission electron microscope (TEM) is a microscopy technique operates on the same basic principles as the light microscope but uses high energy electron beam instead of light. Since it uses electrons (accelerated at several hundred kV: 200 kV electrons have a wavelength of 0.025Å) as the light source, SEM generates a resolution thousand times better than with a light microscope. Electromagnetic lenses are used to focus the electrons and the image is observed on a fluorescent screen, or recorded by a digital camera or on film. (Figure 2-9). The whole system from source to screen is under vacuum and the sample has to be very thin so that the electrons travel through it.

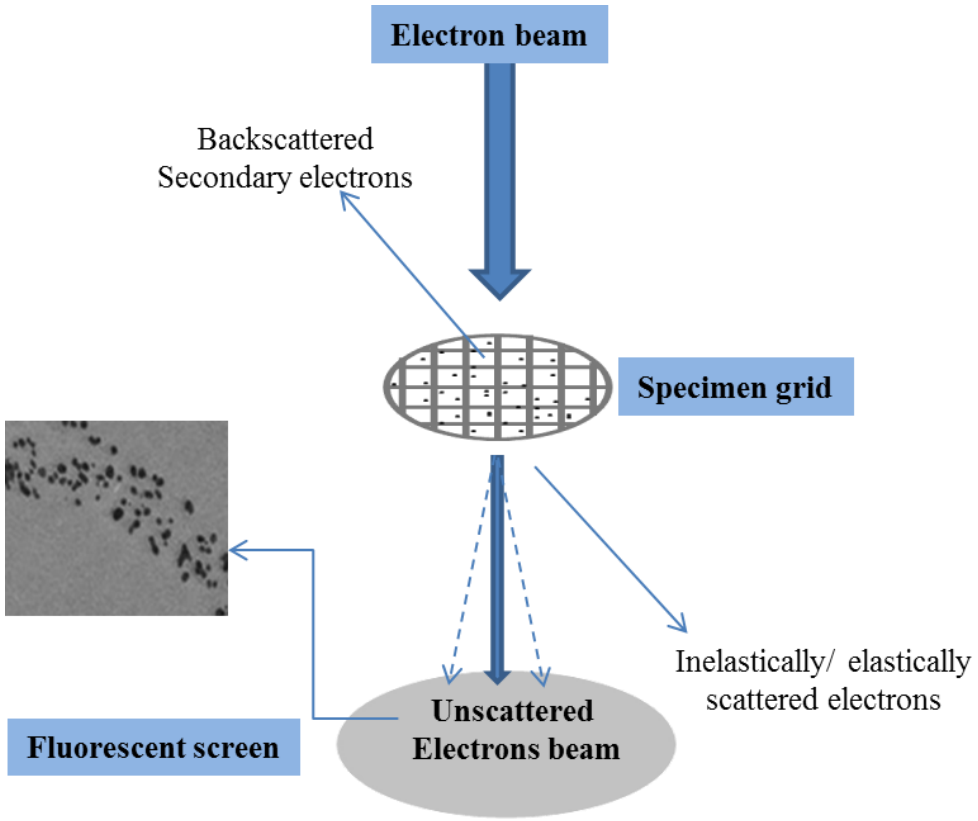

Figure 2-9: Schematic representation of TEM technique.

TEM images reported in this thesis were acquired using Hitachi H-7000 TEM instrument. Samples were prepared by putting a drop of ultrasonically-mixed, dilute suspension of the nanoparticles on a carbon-coated grid. After evaporation of the solvent the grids were inserted into the TEM chamber for measurements. Experiments were carried out under high vacuum conditions.

2.6 Contact Angle Measurement

If a drop of liquid is placed on a solid surface there are mainly two possibilities: the liquid will spread on the solid surface completely (contact angle, $\Theta = 0$) or there will be a fixed angle based on the properties of the surface and the liquid droplet. In the latter case, a three-phase contact line (Fig. 2-10) is formed. The three phases: the solid, the liquid, and the vapor are in contact at this line.

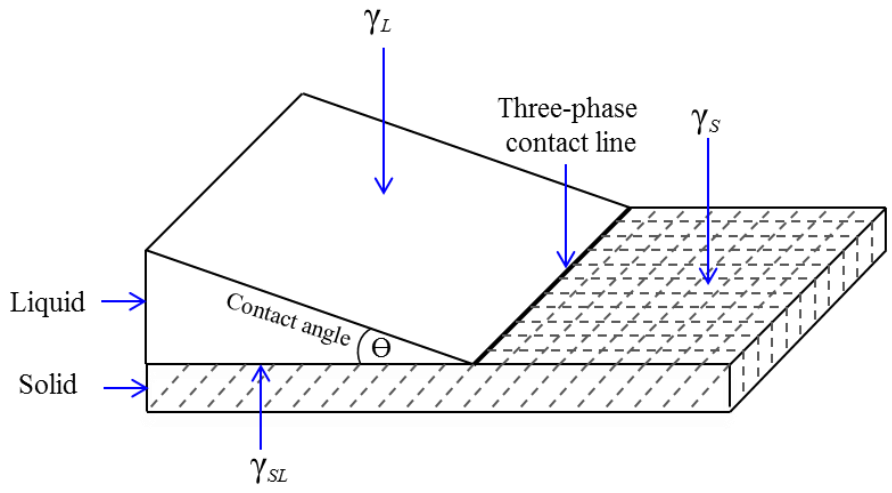

Figure 2-10: Contact angle (Θ) of a liquid drop on a solid surface.[9]

In 1805, Thomas Young[10] first described the contact angle of a liquid drop on an ideal solid surface as the mechanical equilibrium of the drop under the action of the three interfacial tensions. Therefore, Young's equation is the basis for quantitative description of contact angle measurement.

$$\gamma_L \cdot \mathrm{Cos}\,\Theta = \gamma_S - \gamma_{SL} \tag{2-9}$$

Where,

Θ is the contact angle

γ_L is the solid surface free energy

γ_S is the liquid surface free energy

γ_{SL} is the solid/liquid interfacial free energy

If the interfacial tension of the solid phase is higher than that of the solid-liquid interface ($\gamma_S > \gamma_{SL}$), the contact angle will be smaller than 90°; the liquid will partially wet the solid. In opposite case ($\gamma_S < \gamma_{SL}$), the contact angle will exceed 90°; the liquid will not wet the solid (figure 2-11).

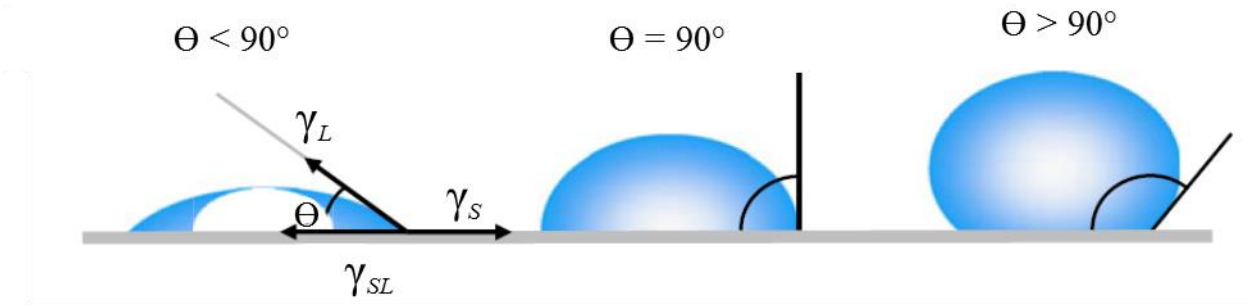

Figure 2-11: Schematic representation of contact angles formed on a smooth homogeneous solid surface.

Contact angle is commonly measured by observing a sessile drop with a telescope or microscope. A goniometer is usually used to determine the contact angle. Contact angles in this thesis were measured at ambient conditions on a VCA Optima goniometer (AST Product, Inc., MA) by the sessile drop technique. Drop sizes (1μL) were controlled and each reported contact angle was an average value of at least three drops on different areas of a given wafer.

2.7 Gas Chromatography- Mass Spectrometry (GC-MS)

The gas chromatography-mass spectrometry is an analytical technique, combining the features of gas-liquid chromatography and mass spectrometry, by which complex mixtures of chemicals may be analyzed.[11] The GC-MS is widely used to determine structure, molecular weights, and elemental composition of organic compounds in a complex mixture. Details of this method may be found in the literature.[12] However, a brief account is given here. The sample solution is injected into the GC inlet. The sample is then vaporized and swept onto a chromatographic column using the gas carrier, usually helium. While the sample flows through the column, the compounds in the mixture are separated by virtue of the relative interaction with the carrier gas (mobile phase) and the coating of the column (stationary phase). Then the samples pass through a heated transfer line and converted to ions at the ion production point, usually by electron ionisation. When the analyte or sample compounds are introduced into the mass spectrometer ion source, the sample molecules are ionized by a beam of electrons produce the radical cation. The process can be written as-

$$M_{(g)} + e^- = M^+_{(g)} + 2e^- \qquad (2\text{-}10)$$

The peak for this ion in the mass spectrum gives the molecular weight of the compound. The molecular ion usually fragments into smaller ions due to the large amount of imparted energy which provide the fingerprint for the molecular structure. The degree of fragmentation depends on the energy of the impacting electrons and on the 1^{st} ionisation potential of the sample molecule. Ions can also be produced by chemical ionisation especially for volatile or/ and halogenated compounds. The positively charged ions are then separated according to various mass related properties which depend upon the type of analyser used. Most commonly used analysers are quadrupole mass-spectrometers and ion traps. The separated ions are detected by a detector and are amplified to boost the signal as a visual display on the computer screen.

In my research work, GC-MS analysis was performed using an Agilent 6850 series GC with a FID detector equipped with 19091J-413E nonpolar column and operated under HP GC ChemStation software.

2.8 References

(1) *Surface Analysis by Auger and X-ray Photoelectron Spectroscopy*; Briggs, D.; Grant, J. T., Eds.; IM Publications and SurfaceSpectra Limited, 2003.

(2) Hertz, H. *Annalen der Physik* **1887**, *267*, 983.

(3) (a) Wagner, C. D. *Anal. Chem.* **1975**, *47*, 1201(b) Wagner, C. D. *Farad. Discuss.* **1975**, *60*, 291(c) Wagner, C. D.; Joshi, A. *J. Elec. Spectrosc. Relat. Phenom.* **1988**, *47*, 283.

(4) Moretti, G. *J. Elec. Spectrosc. Relat. Phenom.* **1998**, *95*, 95.

(5) Moretti, G. *J. Elec. Spectrosc. Relat. Phenom.***1995**, *76*, 365.

(6) Thomas, T. D. *J. Elec. Spectrosc. Relat. Phonom.* **1980**, *20*, 117.

(7) Wagner, C. D. *J. Elec. Spectrosc. Relat. Phenom.***1977**, *10*, 305.

(8) Veal, B. W.; Paulikas, A. P. *Phys. Rev. B* **1985**, *31*, 5399.

(9) Butt, H.-J.; Graf, K.; Kappl, M. *Physics and Chemistry of Interfaces*; WILEY-VCH GmbH & Co. KGaA, 2003.

(10) Young, T. *Phil. Trans. Roy. Soc.* **1805**, *95*, 65.

(11) (a) *Food Toxicants Analysis*; first ed.; Picó, Y., Ed.; Elsevier Science, 2007(b) Lambert, J. B. *Organic structural spectroscopy*; Prentice Hall: Boston, MA, 2011.

(12) *Handbook of Instrumental Techniques for Analytical Chemistry*; Settle, F. A., Ed.; Prentice Hall PTR, 1997.

Chapter 3

Preparation and characterization of self-assembled monolayers of perfluoro-octyltriethoxysilane and 3-mercaptopropyltrimethoxysilane on Si wafer.

3.1 Introduction

The formation of organic monolayers using the Langmuir and Blodgett (LB) technique was discovered in 1920.[1] In this case, a weak bond forms between the molecules and substrate by physisorption.[1] Self-assembled monolayers (SAMs) refer to the molecular assemblies that form spontaneously by the immersion of an appropriate substrate into a solution containing an active surfactant.[2] Alteration of the properties of solid surfaces to facilitate the covalent immobilization of different molecules has become an important process in the generation of surfaces with controlled binding properties. Self-assembled monolayers and multilayers formed on silicon (Si) surfaces have found potential applications in the construction of low-energy surfaces, lubrication, bio-compitable surfaces, monolayer lithography, biosensors, and catalysis.[3]

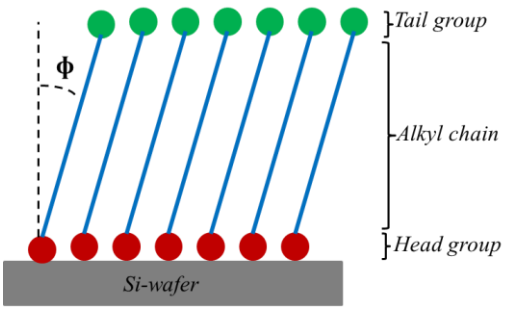

Figure 3-1: A schematic representation of different parts of SAMs. ϕ represents the tilt angle of alkyl chain.

The SAMs generally consists of three parts: the -*head group* which forms the chemical bond with the atoms on the surface; an -*alkyl chain* contributes to ordered packing of the molecules by means of the van der Waals interaction between the chain; and the *tail group* modifies the property of the surface through the use of different functional groups.[4] Those SAM precursor molecules that exhibit higher packing density will generate better coverage and a more ordered over layer. Usually the tilt angle is lower for the higher packing density SAMs.

There are two classes of SAMs that are widely reported[4]: alkanethiols on gold substrates and chlorosilane or alkoxysilane SAMs on silica substrates. Alkanethiol on gold was first reported in 1983[5] and the silane-based SAMs were coined by Bigelow *et al* and further developed by Moaz and Sagiv.[2,6] Numerous studies have explored such variables as the effect of solvent, ligand/ precursor concentration, deposition time, and temperature.[7] A large number of precursors have been used to functionalize different substrates such as $–CH_3$ terminated nonpolar octadecyltrichlorosilane (OTS), $–NH_2$ terminated aminopropyltriethoxysilane (APTES), and –SH terminated polar 3-mercaptopropyltrimethoxysilane (MPTMS) on glass[8], SiO_2[9] or gold[10]. Amongst these, MPTMS has attracted significant attention because of its affinity for both silica and to the noble metals such as gold.[11] MPTMS has also been used as the coupling agent/ ligand between Si surface and transition metals and have potential application in biosensors, protein absorption, and catalysis.[12] Although the adsorption of MPTMS on SiO_2 has been widely studied, reproducibility has been difficult to achieve because of their interplay between different parameters.

MPTMS deposition is also dependent on the nature of the silica substrate. For example, commercially available silicon wafers are typically covered with a layer of native oxide (SiO_{2-x}) which is quite different from an oxide layer grown using wet-chemical processes. Native oxides are sometimes hydrophobic in nature because of the presence of siloxane rings, which are stable against hydrolysis. Surface functional groups are responsible for the molecular properties of silicon. Contamination on the commercially available Si-wafers is a is a major problem in many industries such as semiconductor, storage, imaging, pharmaceuticals, automotive, food, and medical equipment[13] Typical contaminant particles deposited on the wafer surface range in the size of less than 10 nm to several hundred microns.[13] Contamination can be from the metal ions, organic contaminants, and particulates that are readily adsorbed on the surface. These contaminants may also be encountered during the manufacturing process, in the processing room, or from the processing chemicals and water. The presence of contamination on the silicon wafer surface causes the uncontrolled variations in the surface fabrication process which can be viewed visually or may be detected with sophisticated analytical equipment. Since contaminants have an impact on products performance, the silicon wafers require contamination removal to achieve high performance of product. There are many cleaning processes and nearly all the cleaning and surface functionalization processes are done in the liquid phase, because the liquid phase provides the advantage of high solubility of chemical reagents and contaminants, and easier prevention of electrostatic deposition of particles associated with air.[13] Therefore, cleaning these contaminants is the pre-requisites for modifying a surface.

Since this is the key step or the foundation of making self-assembled monolayers/over layers, a number of procedures have been developed to clean the silicon wafer surface. Detailed

information about silicon wafer cleaning procedures are available in the literature.[13] However, the most widely used protocol for Si wafer cleaning known as the RCA process (after the RCA corporation by whom the inventor were employed) was developed by Werner Kern *et al.* in 1970s.[14] Since then the formulations have been modified but the methods developed 40 years ago remain the backbone of most Si wafer cleaning processes. As second method of cleaning Si wafer involved using a H_2SO_4 and H_2O_2 mixture, known as piranha solution. The cleaning of the silicon wafer is also known as hydroxylation because after cleaning SiOH groups are introduced onto the surface. The RCA and piranha cleaning procedure are briefly described below:

Cleaning by RCA solutions:

RCA solution is a mixture of NH_4OH, H_2O_2, and H_2O with the composition of 1:1:5 to 1:1:50 parts by volume. The substrates are heated in the solution at a temperature of 40-75°C for about 10-20 mins followed by quench and rinse with copious amounts of DI H_2O.

Cleaning by Piranha Solution:

Piranha solution is a mixture of concentrated H_2SO_4 and 30% H_2O_2, which is used to remove gross organic materials from Si surfaces. The ratio of H_2SO_4 to H_2O_2 varies from 2:1 to 4:1 by volume. The substrates are usually heated at a temperature of 80-100°C for 30 to 60 mins. Then the substrates are rinsed with deionized water several times to remove viscous liquid. The piranha solution is a strong oxidizer; it does remove most organic matter, and will hydroxylate the surface as well. The resulting surface is extremely hydrophilic. Handling piranha solutions

require special safety features; because this can be explosive (if mixed with acetone or isopropyl alcohol)! During preparation, one must always use protection equipment, and add the H_2O_2 to the H_2SO_4,not the other way around. Before disposal, one must allow the solution to cool, and diluted with distilled water. A catalytic amount of manganese dioxide will help to reduce the oxidizing ability of the solution.

The goal of this part of my research is to better understand the basic features of the Si surface functionalization process with organic precursors; more specifically, to generate a Si-based surface with transition metal binding capabilities that can be further used as catalysts for coupling reactions or scavengers for transition metals/ heavy metals.

3.2 Experimental

N-type Si (100) wafer were purchased from S.E.H. Malaysia, MPTMS and perfluorooctyltriethoxy silane (PF8) were purchased from Sigma-Aldrich; ammonium hydroxide 30% solution in water was obtained from Caledon Labs; 30% hydrogen peroxide and 98% and fuming sulfuric acid were bought from Fisher Scientific.

3.2.1 Hydroxylation/ Cleaning of Si wafer

In my current research, I used piranha solution and RCA solution to hydroxylate Si wafers: these methods are relatively easy to carry out, and avoid the use of highly hazardous

hydrofluoric acid. The silicon wafers were cut into pieces of 1cm x 1cm size. Initially, the Si wafers were cleaned with either the piranha solution and the RCA solutions alone. Using the process alone did not allow the generation of a completely hydroxylated surface. Then the silicon wafer surfaces were cleaned by treating the surfaces first with piranha solution and then with RCA solution followed by rinsing the wafers with copious amounts of de-ionized water. The samples were dried with N_2 blowing and stored in a glass vial under N_2.

3.2.2 Functionalization of hydroxylated Si wafer

The goal of functionalizing the Si -wafer is to tune the surface properties. In this case, to prepare a surface at which $Pd(OAc)_2$ can attach securely and act as a heterogeneous Pd catalyst (discussed in detail in Ch. 4). The 3-mercaptopropyltrimethoxysilane (MPTMS) was our chosen linker because of its commercial availability and the fact that the thiol group has a high affinity for binding metals. However, before using MPTMS for functionalization, perfluorooctytriethoxysilane (PF8) was used to optimize the conditions for Si surface functionalization. The idea behind the use of this compound was that the sensitivity of the S 2p peak in XPS is very low and obscured by the presence of a strong Si 2p satellite peak, whereas the F1s gives a very intense XPS peak. Figure 3-2 shows the structures of PF8 and MPTMS. Before functionalization, all the glassware was passivated by immersing in a toluene solution of octadecyltrichlorosilane (OTS) for 24 hrs to avoid any competing adsorption of the PF8 and MPTMS on the wall of the glassware.

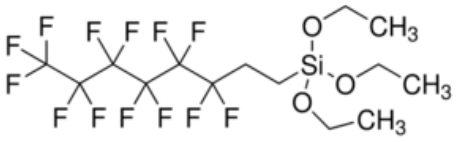

PF8

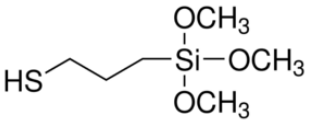

MPTMS

Figure 3-2: Chemical structures of perfluorooctyltriethoxysilane (PF8) and 3-mercaptopropyltrimethoxysilane (MPTMS).

PF8 solutions at concentrations ranging from 1 mM to 50 mM in toluene were prepared under atmospheric conditions. Hydroxylated Si substrates were immersed into PF8 solution for 1 hour to 24 hours at room temperature. Then the samples were rinsed and sonicated twice in toluene for 20 min each, dried by N_2 blowing, and stored in a glass vial. MPTMS solutions were prepared in toluene of varying concentrations (1 mM to 100 mM). The Si substrates were immersed into the solution at controlled conditions for 1 hour to 24 hours. Then the samples were rinsed and sonicated in toluene and chloroform for 20 min each, followed by rinsing with ethanol, dried by N_2 blowing, and stored in a glass vial.

3.3 Results and Discussion

3.3.1 Hydroxylation of Silicon wafer

Once the silicon wafer was hydroxylated using the methods described in experimental section, the substrates were characterized by X-ray photoelectron spectroscopy (XPS), atomic force microscopy (AFM), and water contact angle. Figure 3-3 shows the XPS survey scan of the silicon wafer before and after hydroxylation. It is seen from the figure that after hydroxylation the intensity of the C 1s peak is reduced. Reduction of the C 1s peak proves the removal of organic contaminants. The trace C 1s signal may be due to the presence of residual carbon. O 1s and Si 2p peaks were found in the expected energy regions. No other unusual peaks were observed in the survey scan of the silicon wafer.

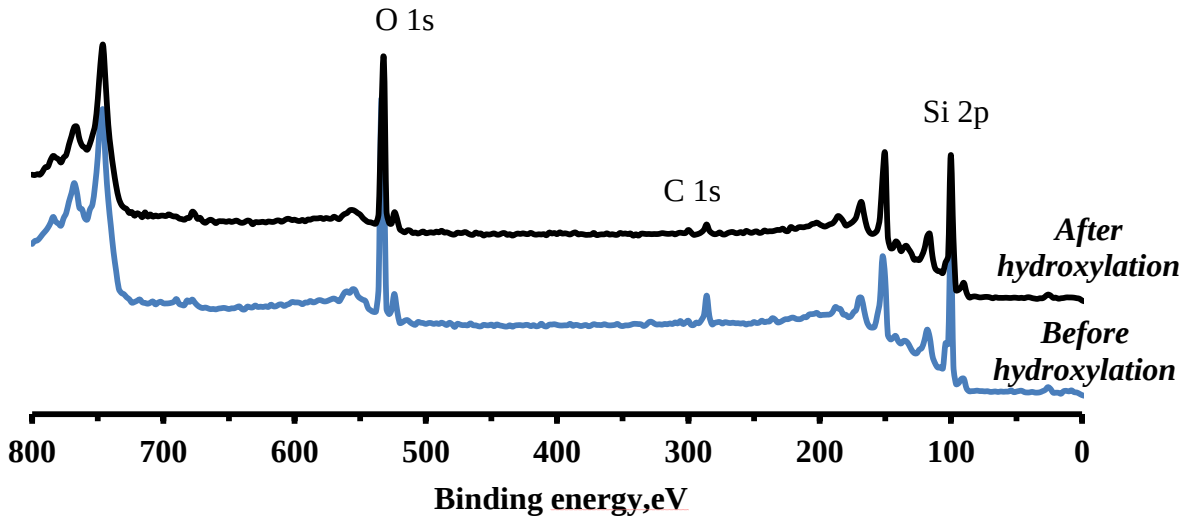

Figure 3-3: XPS survey scan of silicon wafer surfaces before and after hydroxylation.

Contact angle measurements gave information about the surface hydrophilicity of the sample. Surfaces hydroxylated with only piranha solution or only RCA gave contact angles of 25 ± 2^0 and 30 ± 4^0, respectively. These results also correspond well to the literature values(24.5±1.5°).[15] We assume that, following these cleaning methods, the surface did not necessarily become completely hydrophilic or not fully covered with the silanol group, because, theoretically, the contact angle of a completely hydrophilic surface should be zero.

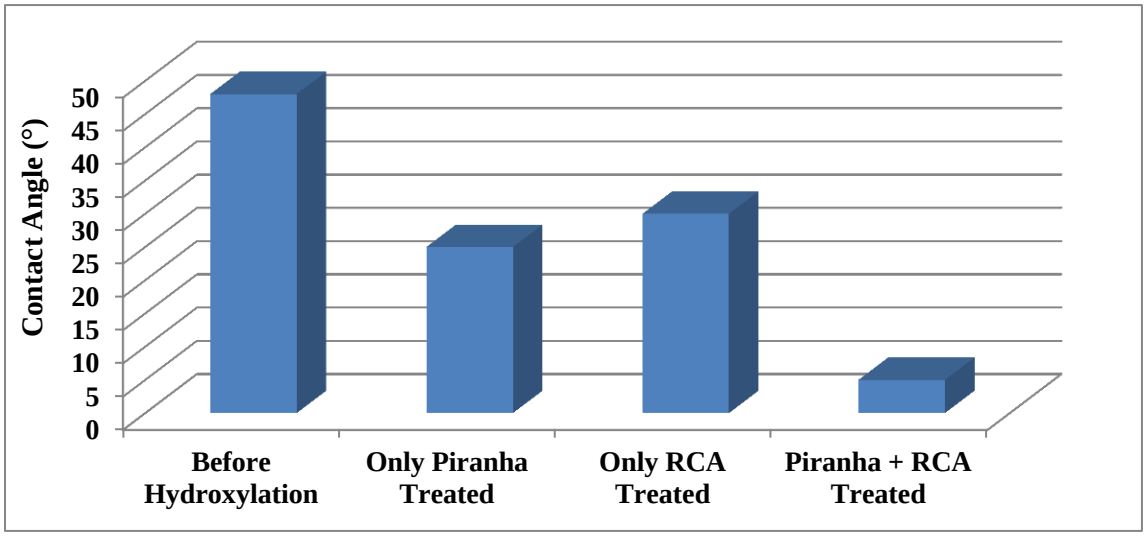

Figure 3-4: Water contact angles of hydroxylated Si wafer surfaces using different methods.

Better results were found by treating the surface with the piranha solution followed by the RCA solution (Figure 3-4 and 3-5). Figure 3-4 shows the water contact angles of silicon wafers before and after hydroxylation respectively. After this two-step treatment, the measured contact angle is reduced to 5 ± 2^0 whereas it was 48 ± 3^0 before hydroxylation, indicating that enough silanol groups formed on the surface to result in an almost completely hydrophilic surface.

(A) (B)

Figure 3-5: Representative water contact angle of silicon wafer before (A) and after (B) hydroxylation.

The surface morphology was also investigated after hydroxylation by AFM. Figure 3-6 shows the AFM image of hydroxylated surface. It is seen from the images that the measured mean roughness (R_a) of the sample was 0.12 nm. The 3-D image also shows the smooth topographic view of the hydroxylated surface. This roughness of the hydroxylated surface also corresponds well with the literature value (0.13 nm).[16]

(A) (B)

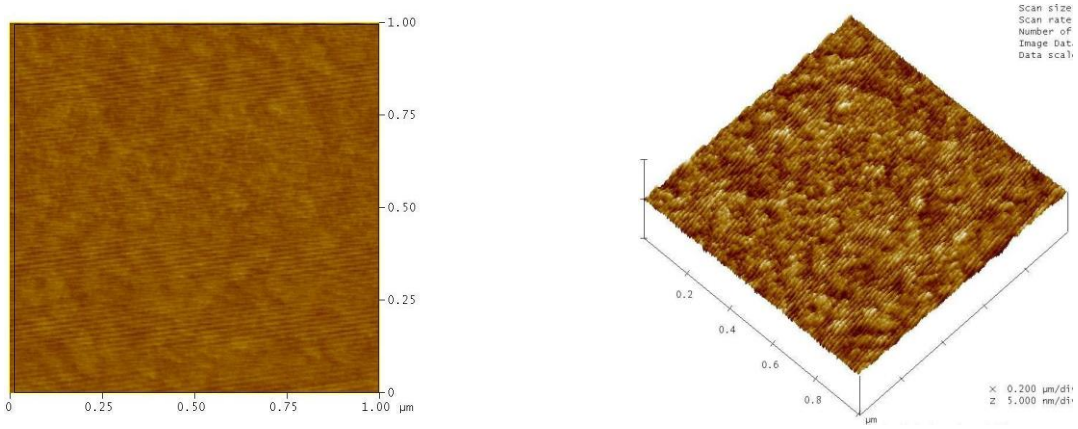

Figure 3-6: AFM images of hydroxylated Si wafer surface. (A – Top view; B - 3D view).

3.3.2 Functionalization of hydroxylated silicon wafer

The deposition conditions and surface properties were characterized using freshly prepared surfaces to avoid contamination. The analytical data of PF8 and MPTMS functionalized surfaces with interpretations are summarized in the following sections.

3.3.2.1 Functionalization of hydroxylated silicon wafer by PF8

The conditions of PF8 overlayer formation on Si surface was optimized by changing concentrations and reaction time. Table 3-1 summarizes the contact angle values of surfaces functionalized with various concentrations of PF8 and deposition time. Due to the hydrophobic nature of the terminal CF_3 group of the silanated surface, contact angle measurements allow one to monitor the effectiveness of the silanization/ functionalization process. If the contact angle is >90°, then water will not wet the surface which means the surface is completely hydrophobic in nature (chapter 2 describes more about contact angles and surface wettability). Hydrophobicity was accomplished using as low as 5 mM PF8 concentration and 24 hours deposition time. Increasing the concentration would reduce the deposition time such that for 10 mM concentrations it took 2 hours and for 50 mM concentrations 1 hour was sufficient to obtain a hydrophobic surface. This is a broad range and to get more specific conditions, we analyzed the surfaces with XPS and AFM as well.

Table 3-1: Water contact angle of various PF8 functionalized Si-wafer surfaces.

Concentration (mM) of PF8	**Deposition Time (Hour)**	**Contact Angle (°)**
1.00	1	44 ± 4
	2	50 ± 2
	24	70 ± 5
5.00	1	60 ± 3
	2	74 ± 4
	24	99 ± 3
10.00	1	65± 3
	2	98 ± 2
	24	108 ± 1
50.00	1	100 ± 5
	2	107 ± 1
	24	108 ± 1

Figure 3-7 shows the contact angle of PF8 functionalized surface. The contact angle of 98 ± 2^0 for the functionalized (*conditions: 10 mM of PF8 and 2 hours*) surface indicates that the surface is no longer hydrophilic. That the contact angle was not much further increased with the increase of concentration indicates that the surface is saturated.

(A) (B)

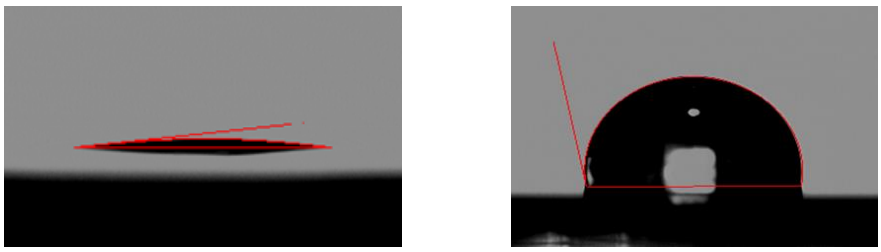

Figure 3-7: Representative water contact angle of Si-wafer surfaces before (A) and after (B) functionalization by PF8 molecule.

PF8 functionalized Si-wafer surfaces were characterized with XPS to determine the elemental composition of Si (both Si(0) and Si (II) oxidation state), C and F. Figure 3-8 shows the representative survey scan of the PF8 functionalized sample.

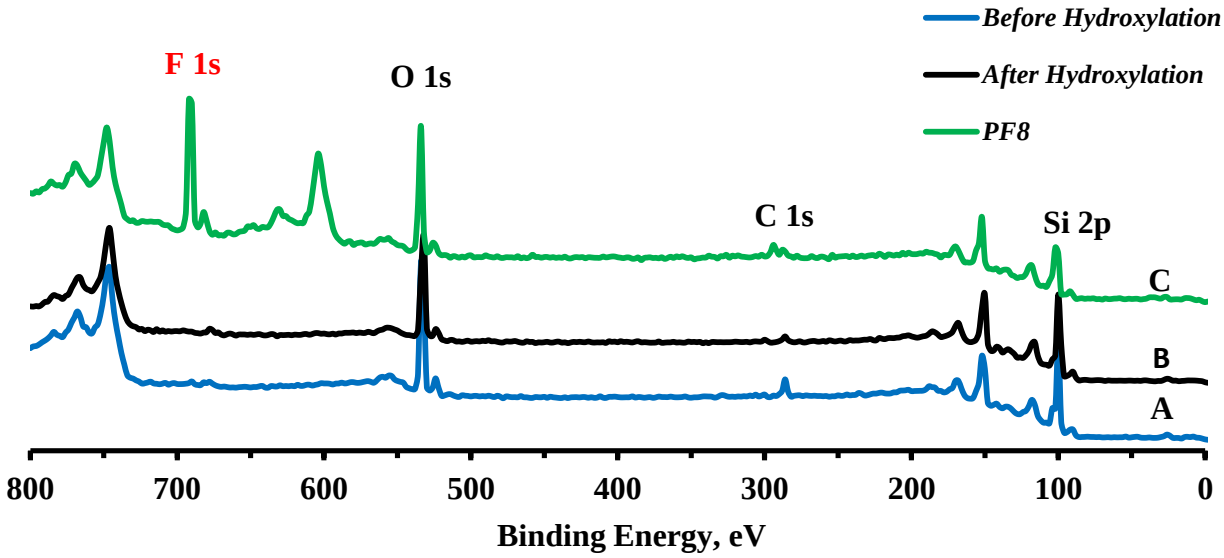

Figure 3-8: XP survey spectra for a Si wafer surface (A) before any modification, (B) after hydroxylation, and (C) after PF8 functionalization.

XPS peaks at 100 eV and 150 eV correspond to the Si 2p and Si 2s environment respectively, while a single peak at 532.0 eV corresponds to O1s. The intense peak of F 1s at a binding energy of 689 eV and a series of C peaks were observed, which confirmed the presence of PF8 on the surface. To optimize the conditions we investigated further by analyzing the C 1s, F 1s, and Si 2p XPS peaks. Figure 3-9 shows the C1s regions for surfaces prepared using varying concentrations and deposition times. Here, three peaks of C 1s were observed for a PF8 functionalized sample. The peak at 285 eV arises from the CH_2 group of the chain and the other two higher binding energy peaks corresponds to CF_2 and terminal CF_3, respectively. Quantitative results are given in table 2. Table 2 compares the stoichiometric C/F intensity ratio to the experimental C/F ratios, indicating that a surface functionalized by 10 mM concentration of PF8 and 2 hours deposition time gives the closest C/F ratio on the surface to the stoichiometric values. This may be due to the formation of a closely packed ordered overlayer of PF8 on the hydroxylated silicon wafer surface.

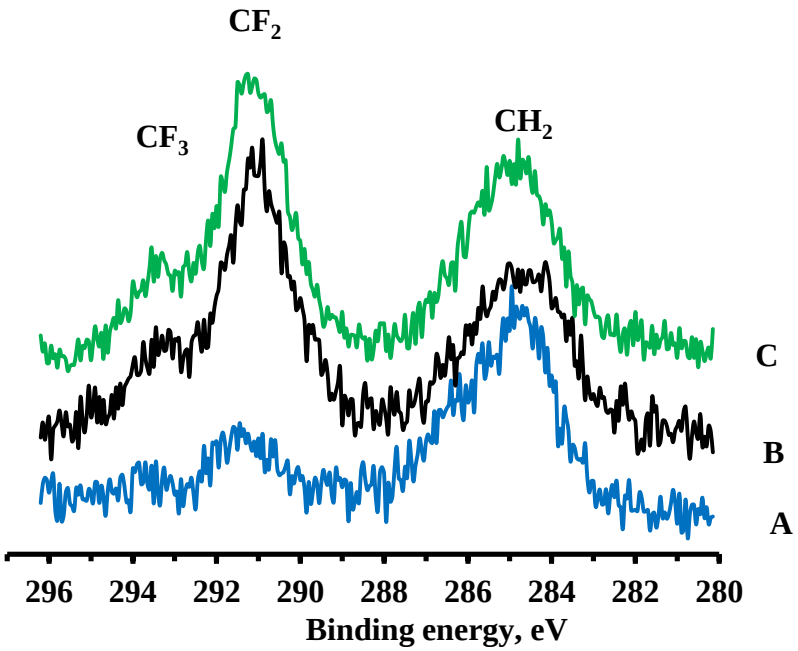

Figure 3-9: X-ray photoelectron spectra of the C 1s for PF8 modified surfaces (A) 5 mM PF8 and 24 hours, (B) 10 mM PF8 and 2 hours, and (C) 50 mM PF8 and 1 hour.

Table 3-2: Comparison of C1s and F1s intensity ratio of PF8 modified surface

Concentration (mM)	**Stoichiometric C/F Ratio**	**Experimental C/ F Ratio**		
		1 hr	**2 hr**	**24 hr**
5	**0.62**	2.56	0.77	0.75
10		0.93	**0.63**	0.55
50		0.66	0.55	0.50

With the increase of deposition time and concentration of PF8 the intensity of F increased and the relative intensity of Si 2p peak decreased. This is due to the formation of a PF8 over

layer on the surface. Figure 3-10 shows the percentage of F and Si on the surface (Samples prepared using 10 mM concentration). It is seen from the graph that the percentage of F on the surface increased with time and after 2 hours it was stabilized. On the other hand, the percentage of Si on the surface decreased with time and stabilized after 2 hours. This can be explained that after 2 hours the surface was saturated and completely covered by PF8.

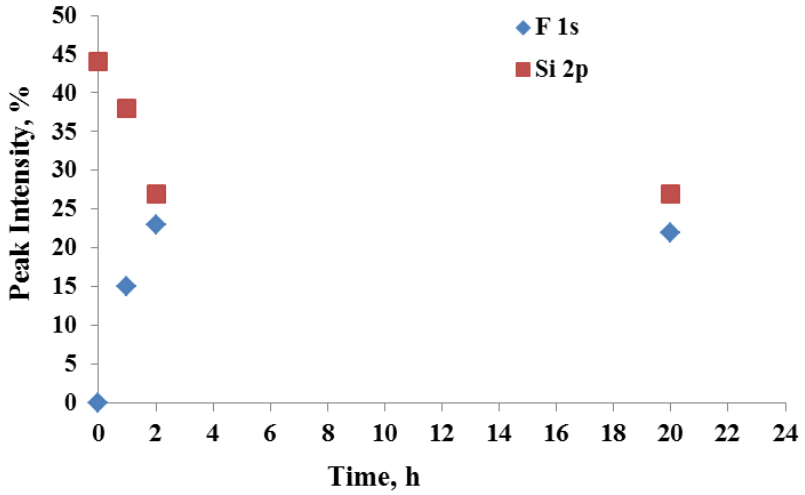

Figure 3-10: Intensity changes with time for F 1s and Si 2p spectra of a PF8 modified surface.

The surface morphology and roughness of the PF8 functionalized samples were also analyzed by AFM. Figure 3-11 shows the topographic view of a PF8 functionalized (*condition: 10 mM and 2 hours*) surface indicating that a smooth over layer of PF8 was present. It is noteworthy that the surface treatment with 10 mM PF8 for 2 hours induces a more homogeneous surface with the surface roughness of 0.335 nm. This result correlates with the XPS and contact angle results.

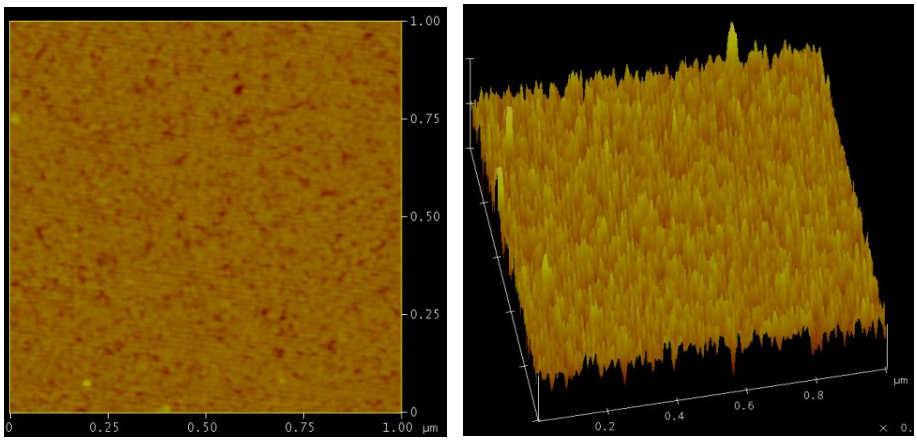

Figure 3-11: AFM images (top view and 3-D view) of Si-wafer surface functionalized by 10 mM PF8 and 2 hours deposition time.

Therefore, the toluene solution of 10 mM PF8 concentration and 2 hours deposition time was considered as the optimum conditions for developing a smooth over layer of PF8 on a hydroxylated Si wafer surface. This result gave a starting point for MPTMS deposition.

3.3.2.2 Functionalization of silicon wafer by MPTMS

Using the approach described above, the hydroxylated Si wafer was functionalized by MPTMS. The effect of MPTMS concentration, deposition time, and water content of solvents were investigated. A range of MPTMS functionalized samples were prepared varying the concentration from 1 mM to 100 mM, the deposition time from 1 hour to 24 hours, and regular and dry toluene as solvents. Samples were characterized to find the optimum condition for

overlayer formation. Figure 3-12 shows the XPS survey scan spectra of a MPTMS functionalized surface where the C 1s peak is more prominent than that of the hydroxylated surface.

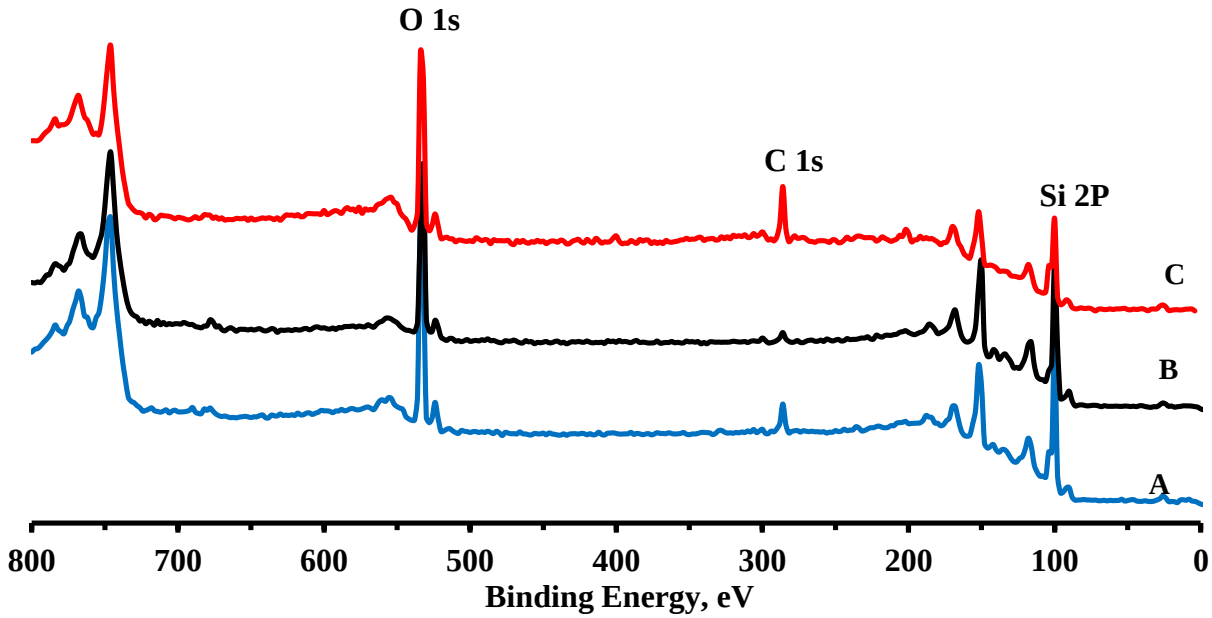

Figure 3-12: XP survey spectra for Si wafer surface (A) before any modification, (B) after hydroxylation, (C) after MPTMS functionalization.

A high resolution S 2p peak was observed for the MPTMS functionalized surface, which indicates that the surface was successfully functionalized. Figure 3-13 presents the S 2p and Si 2p XPS peaks of MPTMS functionalized surfaces. It was found that the intensity of the S 2p peak increased with the increase of MPTMS concentration (Figure 3-13). At the same time, the relative intensity of SiO_2 was increased compared to Si, indicating the formation of a thicker over layer with increasing precursor concentration.

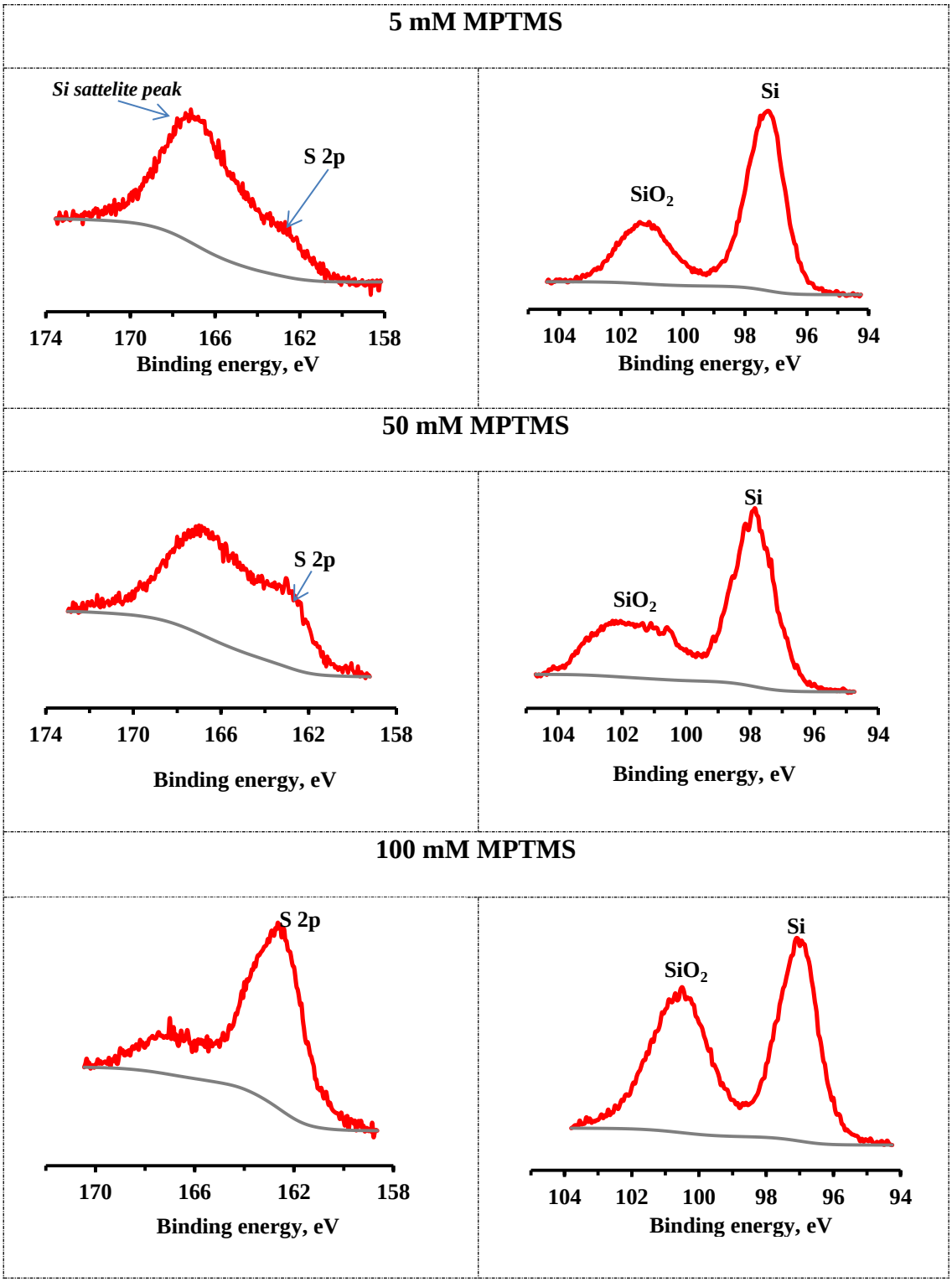

Figure 3-13: S 2p and Si 2p XPS peaks for MPTMS modified surfaces.

Only conditions involving 24 hours or more of exposure time were optimized because less than these times do not produce any discemible S 2p peak in XPS. All the XPS peaks in figure 3-13 correspond to samples prepared with a 24 hours deposition time. Since we used a Si wafer as our substrate, the S 2p peak tends to be masked by the Si satellite peak (figure 3-13), therefore it is sometimes hard to distinguish or interpret. To overcome this issue, we also measured the relatively less intense S 2s XPS peak. Figure 3-14 shows a representative S 2s peak of a MPTMS functionalized surface.

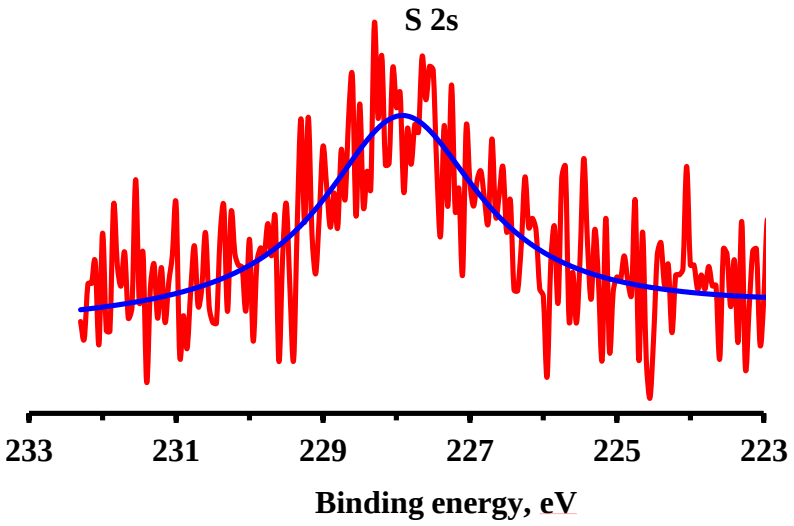

Figure 3-14: Representative S 2s peak of MPTMS functionalized surfaces.

AFM results show that using regular toluene as a solvent generated an uneven overlayer of MPTMS on the hydroxylated Si. This may be due to the fact that presence of trace amount of water in the solvent helped premature polymerization of MPTMS molecules in the solution. These then adsorbed on the surface and formed islands. The presence of large islands is clearly

seen in the AFM images (Figure 3-15). These islands were more prominent on the surfaces functionalized with higher concentrations of MPTMS.

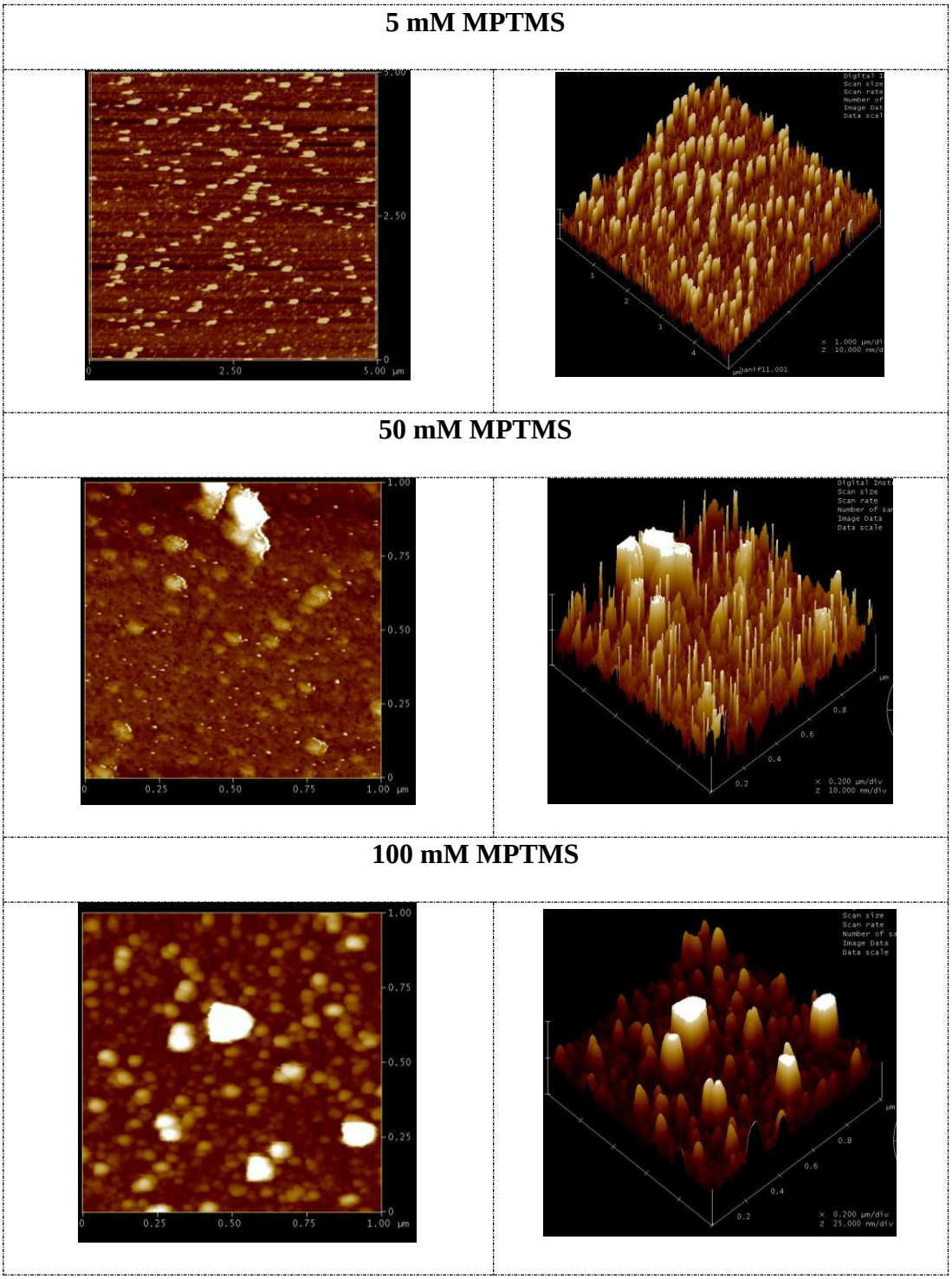

Figure 3-15: AFM images of MPTMS functionalized surface using regular toluene.

Using anhydrous toluene helped overcome this problem. Figure 3-16 shows the AFM images of MPTMS functionalized surfaces prepared using anhydrous toluene. It is seen

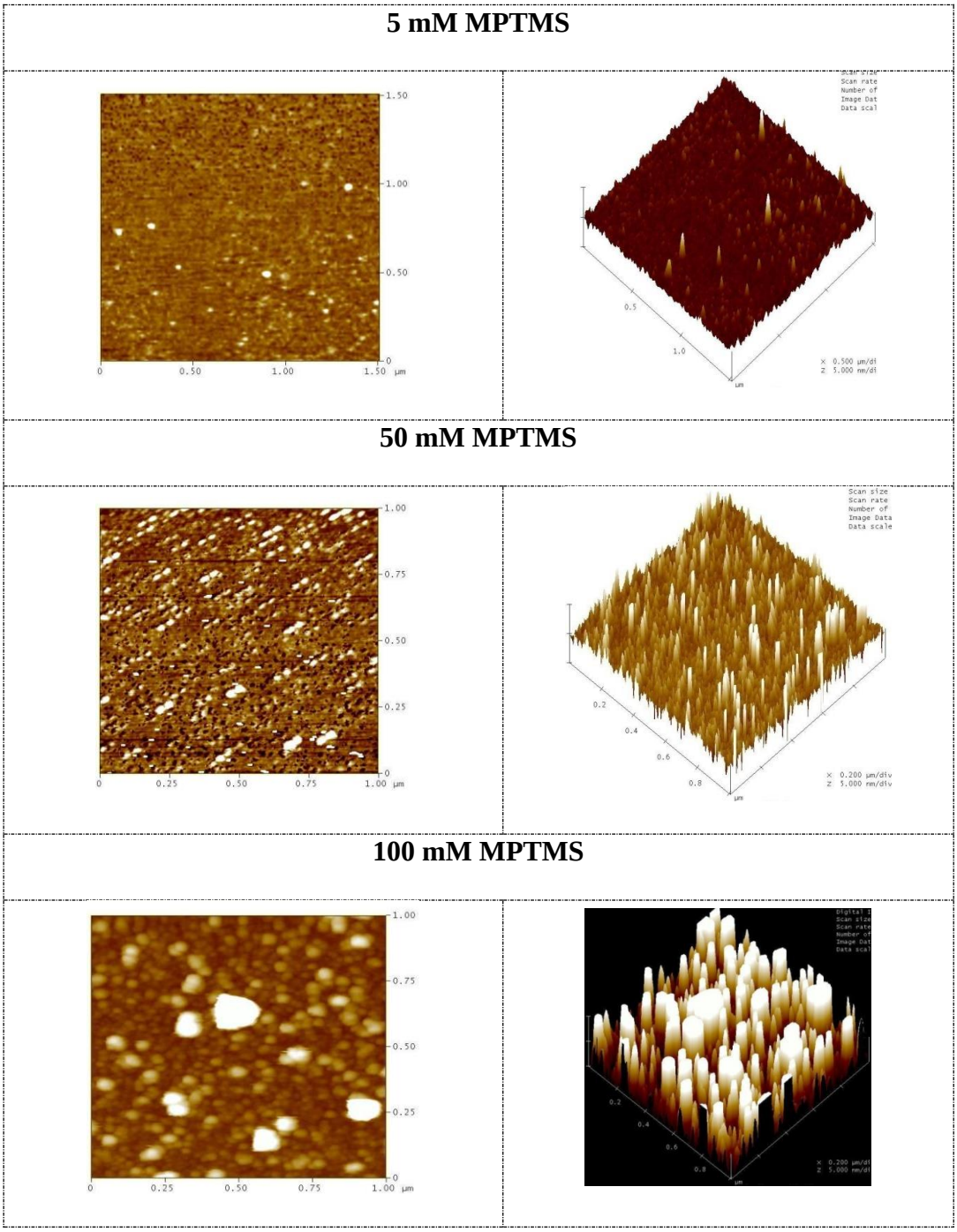

Figure 3-16: Top view and 3-D topographic AFM images of silicon wafer surface modified by MPTMS of different concentration using anhydrous toluene.

from the images that surfaces functionalized with higher concentrations of MPTMS still produce islands. The surface morphology changed significantly with increased concentration of MPTMS. It was recorded in the roughness analysis that there was very large increase of R_a from 0.234 nm to 5.055 nm for 5 mM and 100 mM concentration respectively. Although a greater S content of the surface was reported in XPS analysis (Figure 3-13), topographic analysis using AFM showed that lower concentration was desirable for formation of a smooth overlayer.

Table 3-3: Water contact angles of MPTMS fucntionalized surfaces.

Concentration (mM) of MPTMS	Time (Hour)	Contact Angle (°)
1	1	40 ± 2
	2	43 ± 5
	24	55 ± 2
5	1	50 ± 3
	2	52 ± 4
	24	70 ± 2
10	1	52 ± 5
	2	63 ± 2
	24	81 ± 2
50	1	62 ± 3
	2	67 ± 4
	24	81 ± 4

Table 3-3 presents the water contact angles of various MPTMS functionalized surfaces. A sample prepared with a 5 mM MPTMS concentration and 24 hours deposition time gave a contact angle 70 ± 2°, which corresponds to the literature value of a thiol modified surface.[4]

(A) (B)

Figure 3-17: Representative water contact angle of Si-wafer surfaces before (A) and after (B) functionalization by MPTMS molecules.

Figure 3-17 shows the water contact angles before and after MPTMS functionalization of the surface. The contact angle result also correlates with the AFM results. Comparing XPS, AFM, and water contact results, it can be summarised that 5 mM of MPTMS in anhydrous toluene and 24 hours deposition time is the optimum condition for making a smooth overlayer of MPTMS on the hydroxylated Si wafer.

3.4 Conclusion

The optimum conditions for forming over-layers of PF8 and MPTMS were determined using XPS, AFM, and water contact angle measurements. Hydroxylation of silicon wafers using a two step cleaning process generated a completely hydrophilic surface. The surface chemical composition analysis using XPS, surface wettability analysis using water contact angle, and topographic analysis using AFM gave us a detailed idea about the growth process of organic molecules on the silicon wafer. The self-assembly of organic molecules on the hydroxylayed silicon surface continues to be of great interest in achieving miniaturization of various devices and catalysts design. In my current research work, MPTMS functionalized Si wafers will be used as the support of model heterogeneous palladium catalysts as discussed in the following chapter.

3.5 References

(1) (a) Ulman, A. *Adv. Mater.* **1990**, *2*, 573; (b) Langmuir, I. *Trans. Farad. Soc.* **1920**, *15*, 0062.

(2) Bigelow, W. C.; Pickett, D. L.; Zisman, W. A. *J. Colloid Sci.* **1946**, *1*, 513.

(3) (a) Balachander, N.; Sukenik, C. N. *Langmuir* **1990**, *6*, 1621; (b) Calvert, J. M. *J. Vac. Sci. Tech. B* **1993**, *11*, 2155; (c) MacQuarrie, S.; Nohair, B.; Horton, J. H.; Kaliaguine, S.; Crudden, C. M. *J. Phys. Chem. C* **2010**, *114*, 57.

(4) Aswal, D. K.; Lenfant, S.; Guerin, D.; Yakhmi, J. V.; Vuillaume, D. *Analytica Chimica Acta* **2006**, *568*, 84.

(5) Nuzzo, R. G.; Allara, D. L. *J. Am. Chem. Soc.* **1983**, *105*, 4481.

(6) Maoz, R.; Sagiv, J. *J. Colloid Interface Sci.* **1984**, *100*, 465.

(7) Yang, S. R.; Kolbesen, B. O. *App. Surf. Sci.* **2008**, *255*, 1726.

(8) Tseng, J. Y.; Lin, M. H.; Chau, L. K. *Colloids and Surfaces a-Physicochemical and Engineering Aspects* **2001**, *182*, 239.

(9) Hu, M. H.; Noda, S.; Okubo, T.; Yamaguchi, Y.; Komiyama, H. *App. Surf. Sci.* **2001**, *181*, 307.

(10) Piwonski, I.; Grobelny, J.; Cichomski, M.; Celichowski, G.; Rogowski, J. *App. Surf. Sci.* **2005**, *242*, 147.

(11) Brust, M.; Walker, M.; Bethell, D.; Schiffrin, D. J.; Whyman, R. *J. Chem. Soc. Chem. Comm.* **1994**, 801.

(12) McEleney, K.; Crudden, C. M.; Horton, J. H. *J. Phys. Chem. C* **2009**, *113*, 1901.

(13) *Handbook of silicon wafer cleaning technology*; Reinhardt, K. A.; Kern, W., Eds.; Norwich, NY: William Andrew, 2008.

(14) (a) Kern, W. *RCA Review* **1970**, *31(6)*, 207; (b) Kern, W. In *First International Symposium on Cleaning Technology in Semiconductor Device Manufacturing* Pennington, NJ, 1990; Vol. 90-9:3.

(15) Ben Ali, M.; Bessueille, F.; Chovelon, J. M.; Abdelghani, A.; Jaffrezic-Renault, N.; Maaref, M. A.; Martelet, C. *Materials Science & Engineering C-Biomimetic and Supramolecular Systems* **2008**, *28*, 628.

(16) Zhang, J. L.; Li, W.; Zhai, Y.; Yang, H.; Wang, Y. P. *App. Sur. Sci.* **2005**, *245*, 94.

Chapter 4

Pd and S Binding Energies and Auger Parameters on a Model Silica-Supported Suzuki-Miyaura Catalyst: Insights into Catalyst Activation.

4.1 Introduction

Palladium has been widely used as a catalyst for carbon-carbon bond formation and plays an increasingly important role in cross-coupling reactions, such as the Suzuki-Miyaura reaction.[1] This class of reaction has gained particular attention for its role in the synthesis of pharmaceutical ingredients and fine chemicals.[2] Some compounds of immense economic value such as Valsartan[3] and Telmisartan[4] in the pharmaceutical industry and Boscalid[5] in the agrochemical industry require the use of this reaction as part of the production process. As a consequence of the increased complexity of target molecules in industry and academic research, the development of C-C bond formation methodology and especially the better understanding of the processes that take place during Suzuki-Miyaura reaction remain an important aspect of organic chemistry. Using palladium catalyzed coupling reactions in the synthesis of active pharmaceutical ingredients offers advantages, such as the mild reaction conditions and the relatively non-toxic nature of the catalysts.[6] However, while homogeneous Pd complexes are commonly used as catalysts, they suffer from the problems associated with the requirement of sensitive ligands and the problem of catalyst recovery. Therefore, their efficient separation after reaction for subsequent recycling remains a challenge with both economic and environmental implications.[7]

The heterogenisation of homogeneous catalysts has been a major area of research in the last few decades. Heterogeneous catalysts, by contrast, can often be filtered out of the product mixture and reused without significant loss of activity. A number of immobilization protocols have been used to heterogenize homogeneous palladium catalysts. The most straightforward of these is the physisorption of Pd onto a solid support.[8] However, the weakly bound Pd may leach significantly during the reaction. Another strategy is to covalently tether the Pd to a suitable ligand that is itself covalently linked to a solid support.[6] Alumina, silica and carbon are commonly used in such a catalyst due to their thermal stability and suitable physical properties.[8] Among these, mesoporous silicates have been used widely by many groups as the potential supports for palladium catalysts.[9] [10] [11] Silica offers some advantageous properties including excellent chemical and thermal stability, good accessibility, and the presence of an organic group which can be robustly anchored to the surface to provide catalytic centers. One of the most frequent methods of creating palladium metal complexes, as well as stabilizing palladium nanoparticles, is the addition of an organic ligand that typically contains a heteroelement which may act as a Lewis base. While phosphines[12], amines[13], and carbenes[14] may serve as the Lewis base, the strong interaction between the platinum group metals and soft, sulfur-containing ligands make these very promising and highly efficient stabilizers.[15] MPTMS contains both the siloxane group suitable for hydroxylated surface functionalization and a thiol group to interact with palladium, has been intensively used by ourselves[16] and others[10] [11] to create effective catalyst for Suzuki-Miyaura reactions. Although bulk palladium metal efficiently catalyzes the Suzuki–Miyaura reaction[17], a higher activity of a supported catalyst is achieved due to large active surface area and small particles size, i.e. a high dispersion of the active phase.[8] Thus,

mesoporous silica supporting both a mercaptopropylsiloxane Pd(II) complex together with small Pd clusters, was found to be more active in Suzuki coupling than Pd metal particles alone.[9]

Despite significant success in the development of effective heterogeneous Pd catalysts, there is much evidence suggesting that even traditional heterogeneous catalysts such as bulk palladium[17] or palladium on carbon[18 19] act by releasing small amounts of soluble Pd, which then may redeposit at the completion of the reaction or remain in the reaction mixture. For example, oxidative addition of aryl iodide to Pd(0) results in the dissolution of Pd nanoparticles and formation of ArPdI or $[ArPdI_3]^{2-}$ species.[20] Catalysis using Pd foil[17] demonstrated that the coupling reaction occurs by dissolution of Pd species followed by re-deposition of Pd, preferentially at the cooler edges of the heated reaction site, rather than uniformly across the surface. Thiol functionalized mesoporous silicates are known to be efficient scavengers for Pd and display an excellent ability to remove palladium from organic and aqueous solutions.[11 21] Therefore, they appear to be good candidates as supports for Pd in a heterogeneous catalyst.

On the other hand, the processes taking place on the surface of silica-supported Pd catalysts, particularly the oxidation state of the reactive Pd species, and the role that the thiol tether plays in activation of the catalyst, remain poorly understood. Our previous work using X-ray photoelectron spectroscopy (XPS) and the Auger parameter[16] to characterize Pd catalysts supported on the mesoporous silicate SBA-15 found that Pd forms a new species of lower binding energy during the coupling reaction; this was attributed to the formation of a metallic Pd nanoparticle. Importantly, the binding energies observed still lay in the region normally attributed to Pd(II) species, as opposed to Pd(0) as would be expected for Pd nanoparticles: this

was attributed to a reduction in polarizability in the Pd environment, due to the small size of the nanoparticles formed.

In this chapter, different approaches of making model catalysts are described. The chapter is divided into two parts. The first part describes work associated with the conditions for optimization of the model heterogeneous palladium catalysts preparation and their application in the Suzuki-Miyaura reaction. The second part emphasized a more systematic procedure of making model catalysts, exploring the oxidation state of Pd species and S species present on the catalysts surface, and a better understanding of their activity in the Suzuki-Miyaura coupling reaction. While these catalysts are not as effective as those on mesoporous silicate supports, they have the advantage that a wider range of Pd particle sizes can be grown, as nanoparticle growth is no longer constrained by pore size. This is important as we will explore here the effect of nanoparticle size has on the Pd binding energy. These flat catalysts are also better suited for imaging with atomic force microscopy (AFM) and scanning electron microscopy (SEM). In addition, the cavity structure of the mesoporous silicates results in a catalyst with a range of active sites, which contribute to an average XPS signal; some sites deep within the pore structure may not be observed due to electron attenuation effects. The use of a single layer, flat model catalyst minimizes electron attenuation effects, and should lead to a more homogeneous surface layer. Finally, we will explore the changes in binding energy associated with the thiol ligand, which has often been neglected in previous XPS studies of these catalytic systems.

4.2 Experimental Section

Materials

Palladium acetate, mercaptopropyltrimethoxysilane (MPTMS), octadecyltrichlorosilane, phenylboronic acid, 1-iodo-4-methylbenzene, and pinacol were purchased from Sigma-Aldrich; ammonium hydroxide 30% solution in water was obtained from Caledon Labs; 30% hydrogen peroxide and 98% and fuming sulfuric acid were bought from Fisher Scientific.

Methods

Part one: Palladium acetate solution was prepared in THF with a concentration from 0.1 mM to 10 mM. MPTMS functionalized Si wafers (procedure of making MPTMS functionalized Si wafer is described in Ch. 3) were immersed into the solution of $Pd(OAc)_2$. Deposition/ immersion time was varied from 5 minutes to 24 hours. Then the Si wafers were rinsed with THF and sonicated in THF for 5 minutes to remove loosely bound Pd from the surface. Then these were dried by N_2 blowing and stored in a glass vial.

Part two: In this part, instead of THF, a mixture of THF and ethanol was used as the solvent. Model catalysts were prepared by changing other parameters such as time and temperature (Table 4-1). A series of catalysts were prepared by Pd immobilization on the MPTMS functionalized silicon substrate by immersion in a 1 mM solution of $Pd(OAc)_2$. The effects of temperature, the composition (ethanol/THF) of the solvent, and the exposure time on Pd deposition were explored by using the Scheffé's simplex-lattice experimental design for three

components.[22] [23] [24] Ten different catalysts were prepared, under the conditions summarized in Table 4-1. Ternary plots were then plotted from this data using regression coefficients calculated using Scheffé's algorithm.[22]

Table 4-1: Conditions used to deposit Pd on the thiol-terminated Si substrate

Sample	Pd Deposition Conditions: 1.0 mM $Pd(OAc)_2$			
	Temperature (^oC)	Solvent Composition, vol%		Exposure Time (min)
		Ethanol	THF	
1	50	100	0	60
2	20	0	100	60
3	20	100	0	240
4	42	72	28	60
5	28	28	72	60
6	42	100	0	108
7	28	100	0	190
8	20	28	72	108
9	20	72	28	190
10	30	67	33	120

Phenylboronic acid pinacol ester was synthesized according to the published[25] procedure: phenylboronic acid (3.4 mM) and pinacol (3.4 mM) were dissolved in anhydrous Et_2O; the mixture was stirred for 1 hour at room temperature and concentrated under reduced pressure. The crude product was purified by chromatography (3:7 EtOAc–EtPet), yielding after solvent evaporation the ester in the form of white crystalline solid. $Pd(DMSO)_2Cl_2$ was prepared according to the published[26] procedure: 50 mg of $PdCl_2$ was dissolved in 1 ml of DMSO at 50ºC. The crystals were formed via slow vapor diffusion of diethyl ether into the DMSO solution at room temperature. $Pd_4(OAc)_4(SEt)_4$ and $Pd_6(SEt)_{12}$ were prepared according to published procedures[27] [28] via recrystallization from solutions of the relevant compound in 1,2-dichloroethane. Pd nanoparticles were synthesized according to the procedure by Shen *et al.*[29]

Disulfide functionalized surfaces (R-S-S-R) were obtained by a modified procedure of Aida *et al.*[30] in which the MPTMS-functionalized surfaces described above were immersed in a solution of 3 mg of iodine in DMSO:DI water (1ml:0.1ml) mixture for 1 h, followed by surface washing by DMSO:DI water solution. Alkyl thioacetate functionalized surfaces (R-S-Ac) were obtained by immersing MPTMS-functionalized surfaces in acetic anhydride for 1 h, followed by surface washing by DI water. Alkylsulfate functionalized surfaces ($R\text{-}O\text{-}SO_3H$) were obtained by first functionalizing the hydroxylated Si(100) substrate using 2-(trimethoxysilyl)ethyl acetate by immersion in a 5 mM solution of 2-(trimethoxysilyl)ethyl acetate in toluene for 24 hrs. These were then placed in a 1 M NaOH solution for 20 min to hydrolyze the acetyl group, washed by deionized (DI) water, and dried under a N_2 stream. The resulting alkyl hydroxy-terminated surface was submerged in fuming sulfuric acid (oleum) for 30 min, followed by surface washing by DI water.

Suzuki-Miyaura Coupling Reaction

Part One: For catalysts prepared in part one of the procedure: Freshly prepared catalysts were used in the Suzuki-Miyaura reaction to check their activity. A solution of aryl halide (table 4-2) and phenylboronic acid in 1.8 mL DMF were added to a solution of base (table 4-2) in DI water (0.2 mL) and loaded with the model catalyst, sealed and flushed with argon. Reaction temperature was 65 - 70°C and reaction time was 4 - 20 h, without stirring.

Table 4-2: Suzuki-Miyaura reaction conditions.

Compound	**Formula**	**mM/ Equivalent**	**Amount**	**Solvent, Reaction condition**
1-iodo-4-methylbenzene*	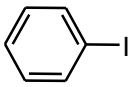	0.035 mM/ 1	7.63 mg	DMF= 1.8mL + H_2O = 0.2mL 65- 70°C 4h-20 h
Phenylboronic acid	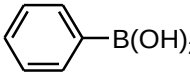	0.0525 mM/ 1.5	10.7 mg	
Base	Cs_2CO_3	0.0525 mM/ 1.5	17.1 mg	

*a series of other compounds were also used: full list are available in the results section.

Part two: A solution of 1-iodo-4-methylbenzene (0.035 mM, 7.63 mg) and phenylboronic acid pinacol ester (0.0525 mM, 10.7 mg) in 1.8 mL of anhydrous DMF were added to a solution of cesium carbonate (0.525 mM, 17.1 mg) in DI water (0.2 mL) and loaded with model Pd catalyst, sealed and flushed with argon. The reaction mixture was then heated at 70°C without stirring under Ar for 24 hrs, cooled to room temperature, and the Si wafer supporting the

catalyst was removed from the reaction mixture, rinsed with DMF:DI water (10:1 v/v) solution, then DI water, and finally dried under an N_2 stream. It was then taken for further surface characterization and recycling, as appropriate. The catalytic reaction was monitored by GC-MS

4.3 Results and Discussion

4.3.1 Characterization of Model Pd Catalysts

4.3.1.1 Part One: Optimization of Pd-catalysts preparation

A schematic procedure of developing the model heterogeneous palladium catalyst is shown in the figure 4-1. Corresponding figures represent how the surfaces were characterized after each step. The first two steps of the procedure and characterization are described in chapter 3. Here, the procedure of immobilizing $Pd(OAc)_2$ on the MPTMS functionalized Si-wafers, application of the model catalysts, and their characterized are discussed.

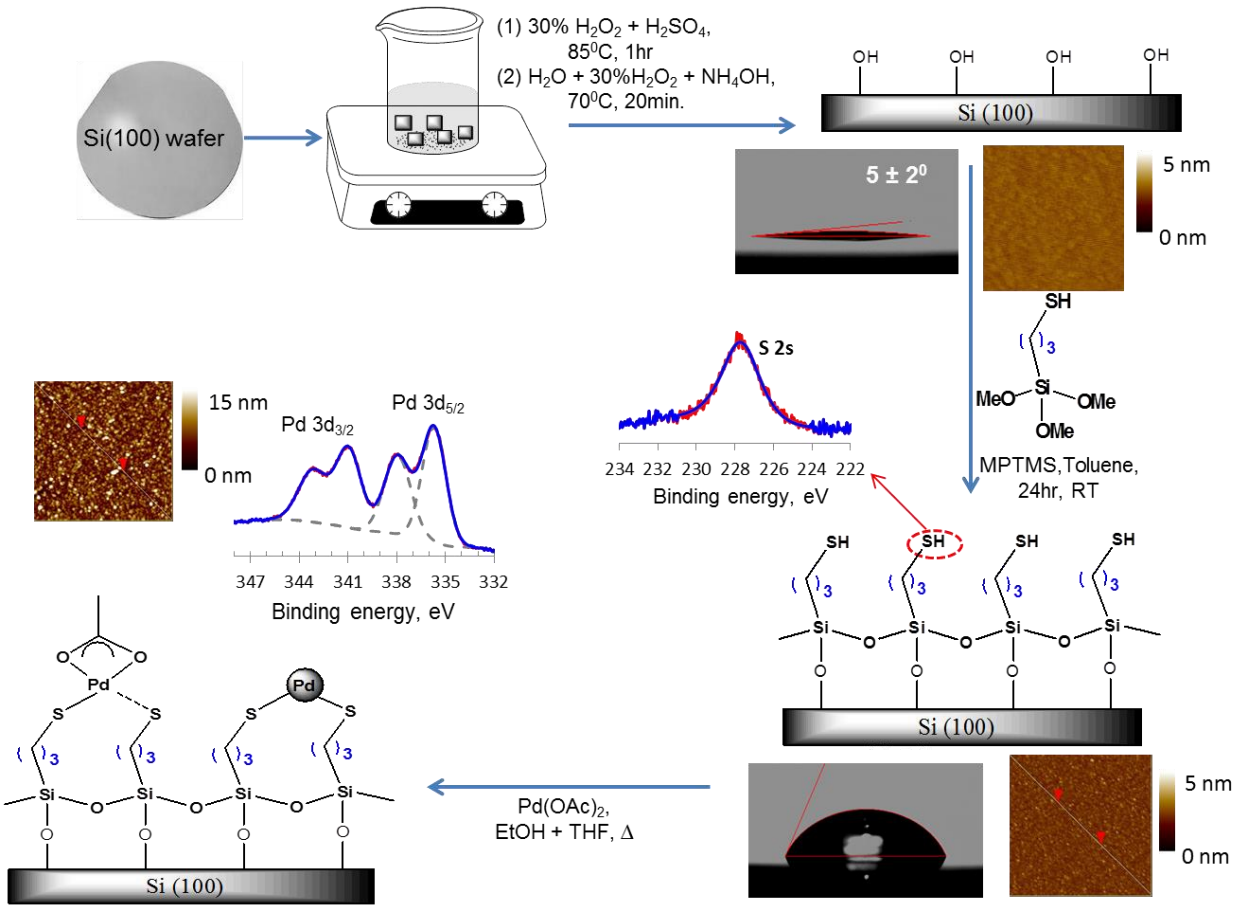

Figure 4-1: Schematic diagram of the preparation of model catalysts, functionalized silicon wafer supported palladium.[31]

Figure 4-2 consists of the XPS wide scan spectra of Si wafers after each step of the preparation. Key observations obtained from wide scan spectra of the Pd immobilized surface (figure 4-2-D) include the presence of a Pd 3d peak at about 337.0 eV binding energy regions, an increased intensity of C 1s peak, and reduction of the intensity of Si peaks. These clearly indicate the deposition of palladium on the thiolated surface. High resolution spectra were collected to support this assumption and to better understand the catalyst's surface.

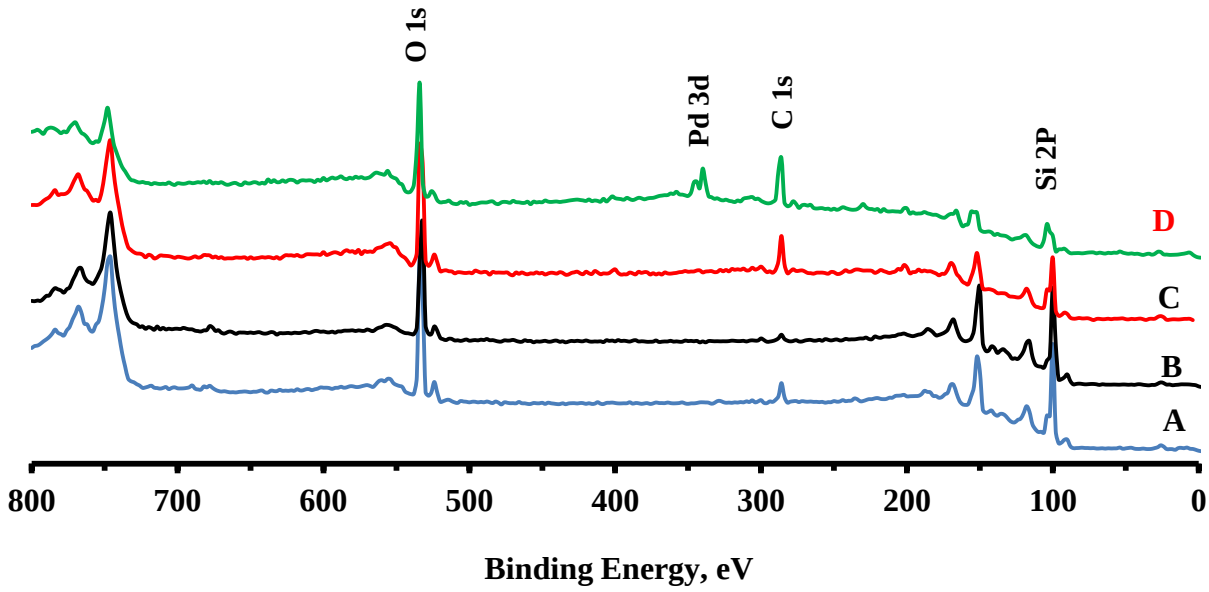

Figure 4-2: XP survey scan spectra for Si wafer surfaces (A) before any modification, (B) after hydroxylation, (C) after MPTMS functionalization, and (D) after Pd loading.

Typical XPS and Auger spectra for palladium, sulfur and carbon of the prepared catalysts are shown in the figure 4-3. Figure 4-3-A represents the Pd 3d peak of palladium acetate powder. It is seen that two peaks (i.e. Pd $3d_{5/2}$, $3d_{3/2}$) were well resolved and here the more intense peak, Pd $3d_{5/2}$, has been considered for our measurement. Palladium acetate powder gives peaks in the region of 338.4 eV, indicative of the presence of Pd (II) oxidation state. After palladium loading on the thiolated Si-wafer surface the shape of the Pd 3d spectra has changed. Figure 4-3-C is the XPS Pd 3d peak of the surface after palladium immobilization. It is clear that more than one species of palladium is present on the fresh catalysts. What are they? There could be many possibilities and will be discussed in the following discussion. For now, I denote the higher binding energy peak as state 1 and the lower binding energy peak as state 2. It is interesting that

this peak (State 2) was not observed in our group's previously reported work – in the functionalized mesoporous silica (SBA-15) supported palladium catalysts. This is evidently

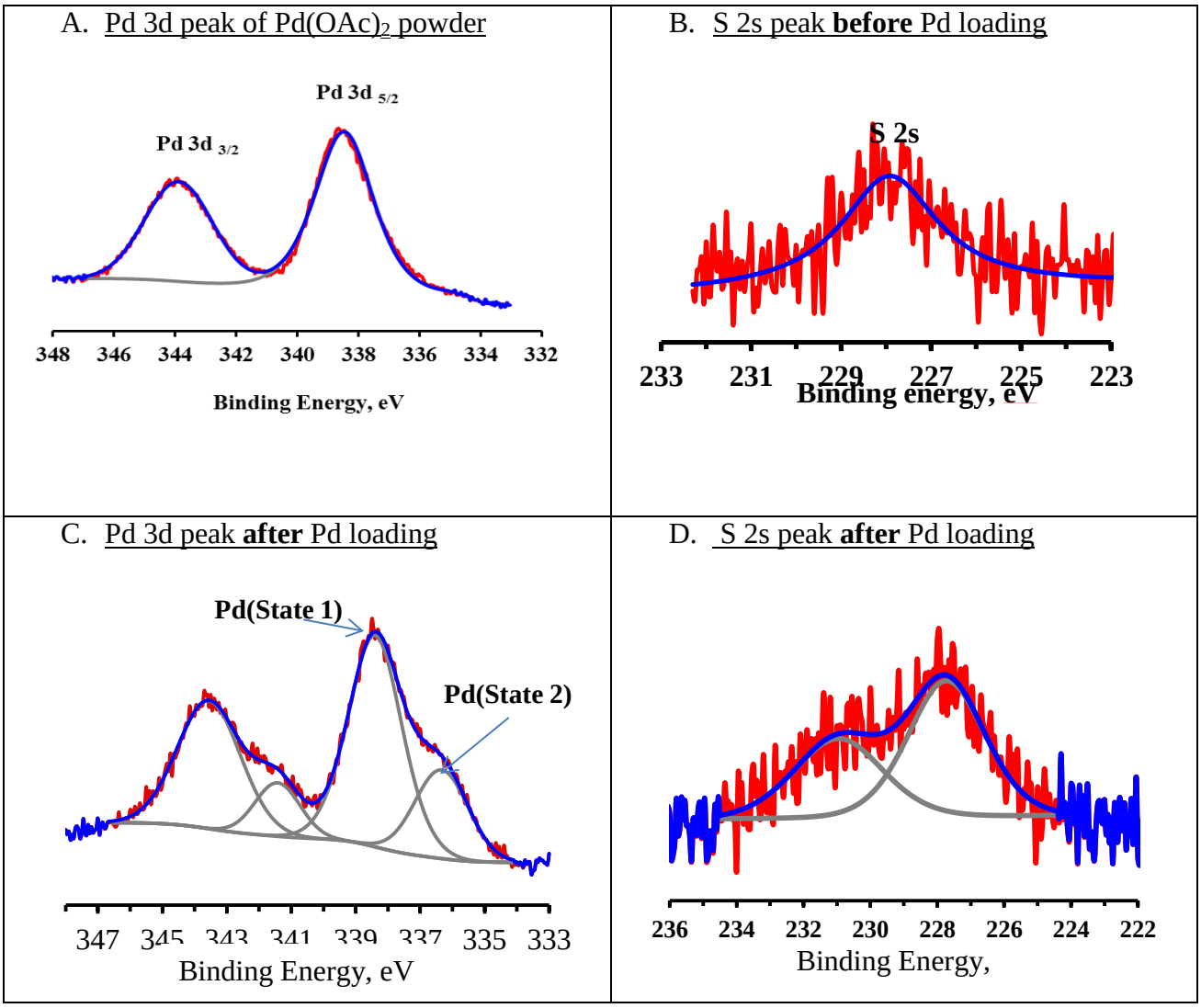

Figure 4-3: XPS spectra of palladium 3d and sulfur 2s of the model catalysts.

one finding, now available to us, using this model system. A similar observation is shown from the sulfur 2s data (figures 4-3-B and 4-3-D) i.e. a new peak of S appeared at a higher binding energy. This is particularly interesting because, to the best of our knowledge, in this kind of

catalyst sulfur XPS data has not been analysed or reported comprehensively. More experiments and analysis to better understand the new peak of Pd (at lower BE) and S (at higher BE) are described in the second part of this chapter. In the Auger analysis we considered the $M_4N_{45}N_{45}$ transition for the Pd XAES peak. A representative Auger peak of the palladium immobilized surface is shown in figure 4-4.

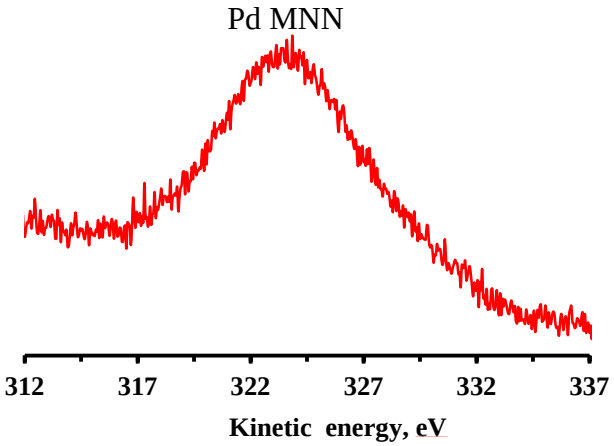

Figure 4-4: Pd MNN transition Auger peak of model catalysts surface.

It was expected that the palladium would be immobilized on the thiolated surface by this process since previous attempts to run the Suzuki-Miyaura reaction using SBA-15 mesoporous silica, and functionalized with MPTMS, were successful.[11,16,32] However, the emergence of a new species of palladium and sulfur identified by the XPS, made us more interested to better understand their growth pattern. In this effort, MPTMS functionalized surfaces were dipped into the $Pd(OAc)_2$ solution of different concentration for different time periods. Figure 4-5 shows the Pd 3d XPS peaks of the $Pd(OAc)_2$ immobilized surfaces with different concentration and times. Immobilization of palladium was successful with as low as 0.1 mM concentration for 1 hour

deposition time. It is interesting to note that, with the increase of concentration and deposition time, the intensity of the state 2 peak also increased.

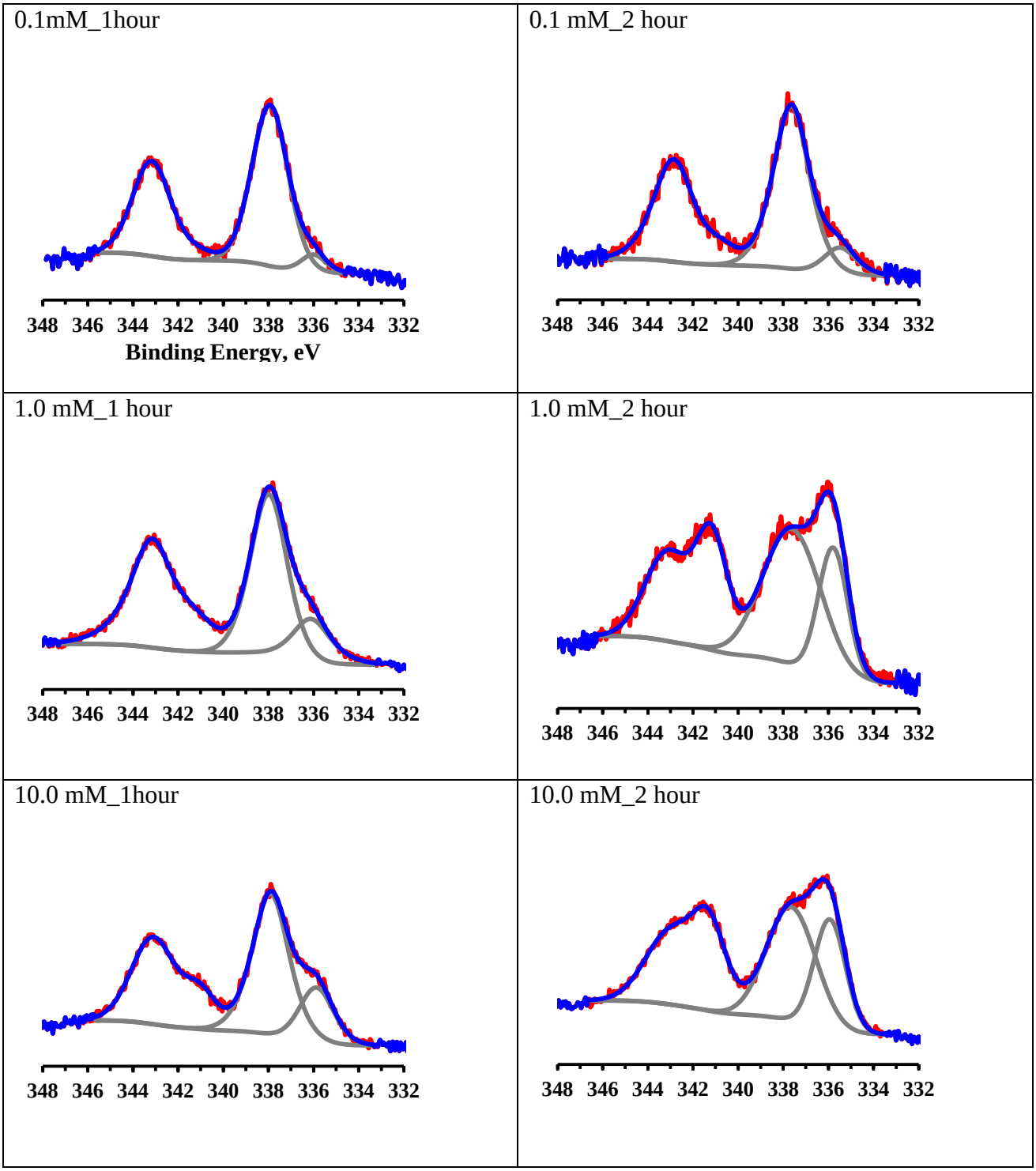

Figure 4-5: Pd 3d XPS peaks of freshly prepared model Pd catalysts

In the case of sulfur, the intensity of the new peak at higher binding energy also increased with increasing concentration and longer deposition times. The corresponding S 2s peaks are shown in figure 4-6. This interesting trend drives us to investigate this phenomenon more closely.

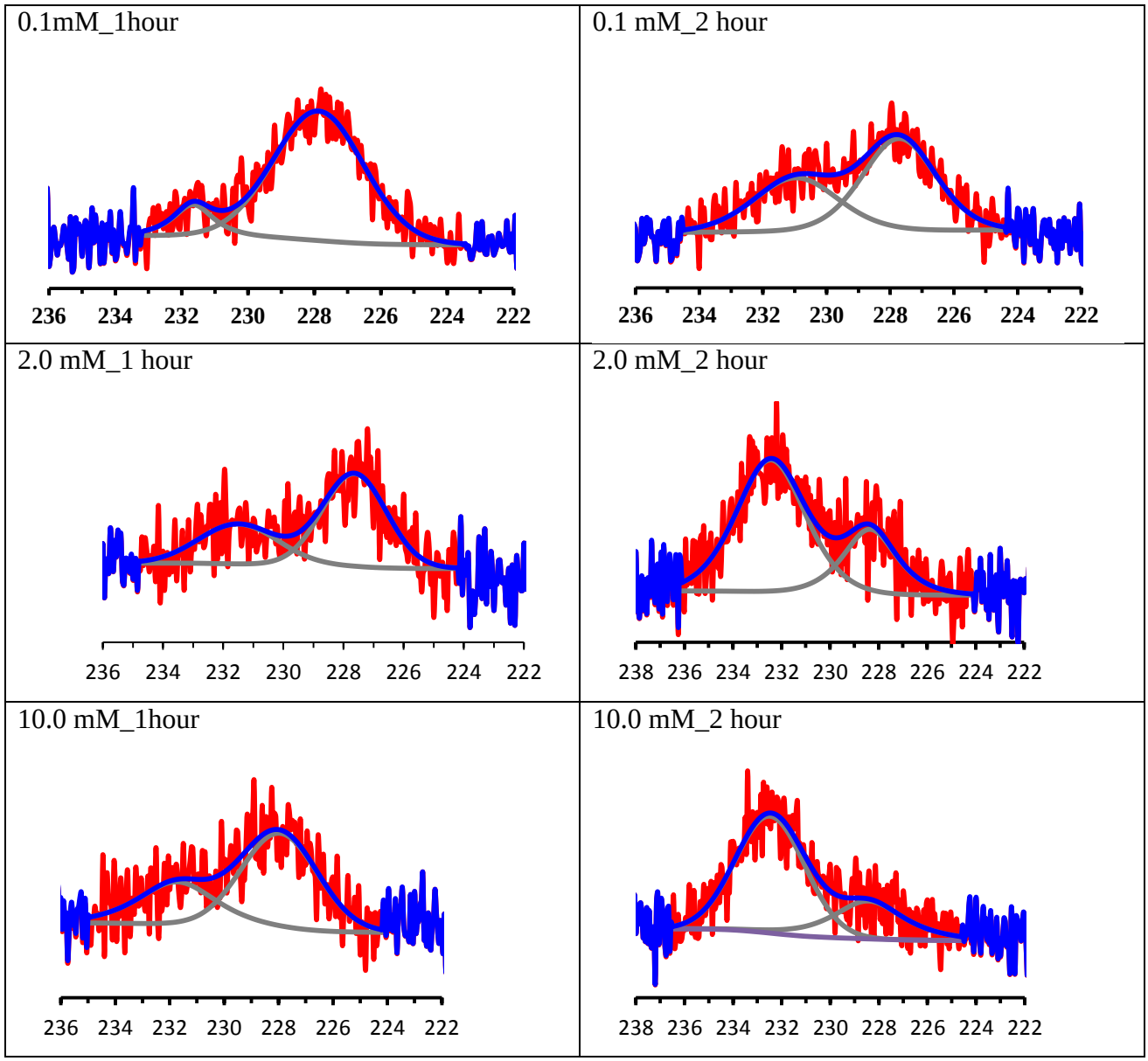

Figure 4-6: S 2s XPS peaks of freshly prepared model Pd catalysts

Next, a large number of palladium catalysts were prepared. It is seen from Figure 4-5 that at 0.1 mM concentration and 1 hour deposition time, the new peak of Pd (State 2) was not very prominent. Since we designed our experiment starting with a very short deposition time, we considered 1 mM concentration of $Pd(OAc)_2$ solution in THF as the standard concentration. Therefore, thiol functionalized surfaces were immersed into the 1 mM $Pd(OAc)_2$ solution from 5 minutes to 5 hours. Thus prepared surfaces were characterized using XPS and AES. Figure 4-7 and 4-8 show the XPS peaks of palladium and sulfur respectively. MPTMS has a strong affinity for palladium, which can be seen from the XPS peaks of Pd 3d. Even after 5 minutes exposure to solution, the presence of palladium on the thiolated surface was identified by the XPS. It is seen from the figures (Figure 4-7) that the new peak of Pd (State 2) appeared after 20 minutes of deposition time and its intensity gradually increased over time. Interestingly, the new peak of S (at higher binding energy) was identified even after 5 minutes exposure.

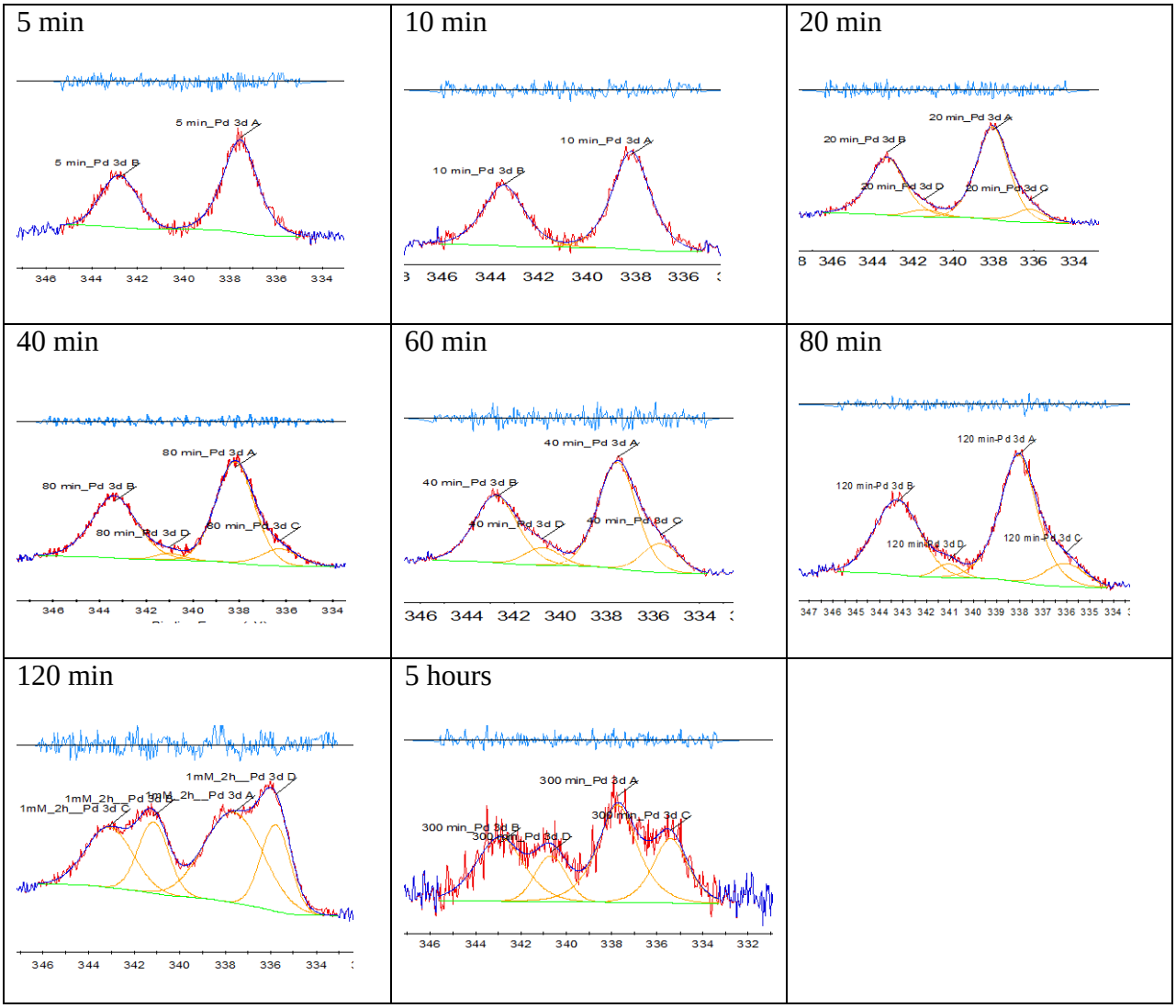

Figure 4-7: Pd 3d XPS peaks of the model catalysts prepared using different deposition time.

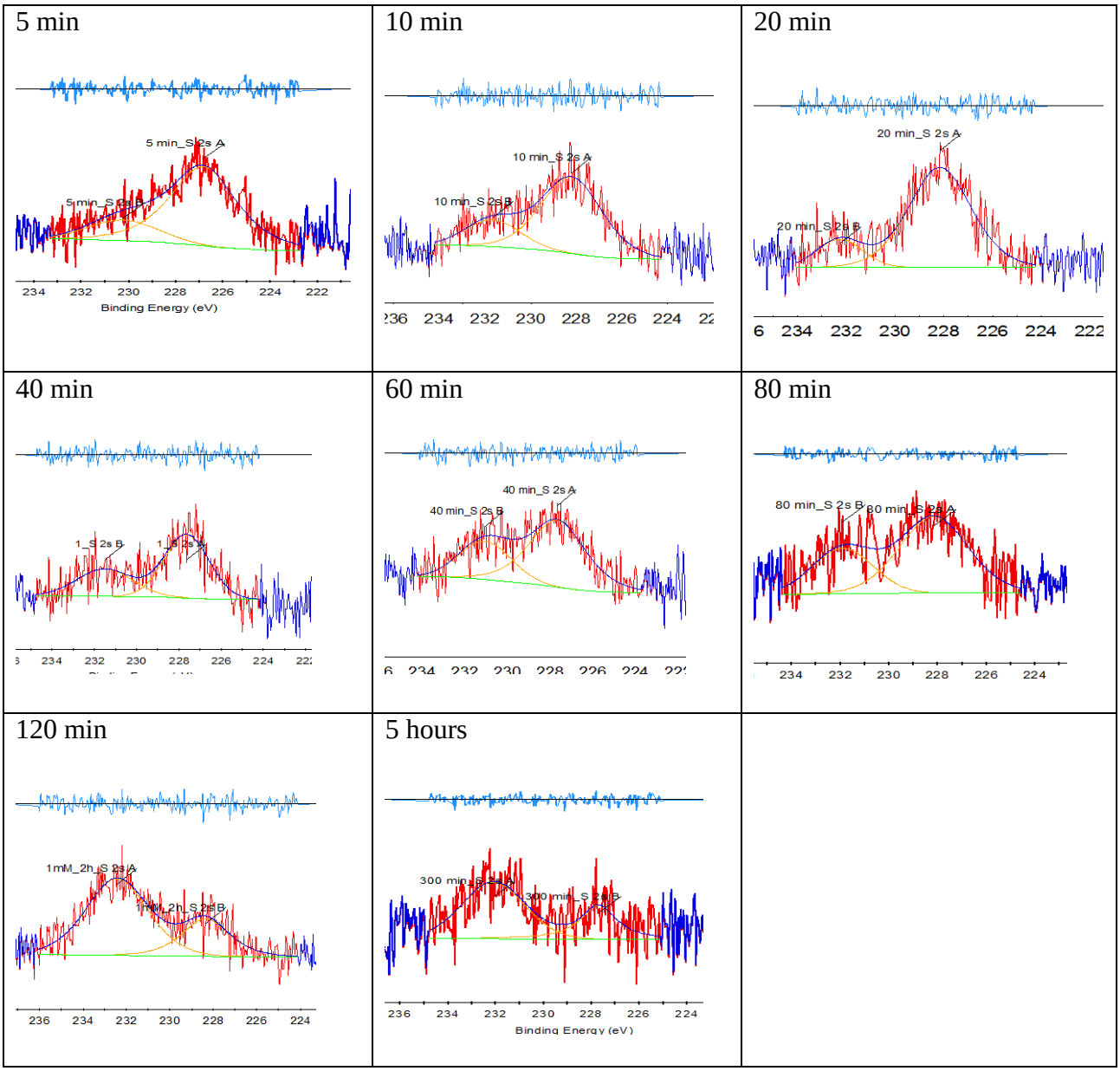

Figure 4-8: S 2s XPS peaks of the model catalysts prepared using different deposition time.

Using XPS data a more comprehensive determination can be made regarding the chemical species present on the surface and a quantitative analysis made of the surface under examination. Table 4-3 summarizes the binding energies of C 1s, O 1s, Pd 3d, and S 2s of XPS

peaks and Pd $M_4N_{45}N_{45}$ Auger peaks of the surfaces immobilized with $Pd(OAc)_2$ at different deposition times. The calculated Auger parameters are also included in the same table.

Table 4-3: XPS peak positions of different elements present on model Pd catalysts as a function of Pd deposition time.

Name	**5min**	**10min**	**20 min**	**40 min**	**60 min**	**80 min**	**120 min**	**5 hours**
C 1s-1	285.0	285.0	285.0	285.0	285.0	285.0	285.0	285.0
C 1s-2	286.9	287.1	286.9	287.0	287.1	286.7	287.1	287.3
Si 2p-1	99.3	99.3	99.2	99.1	99.2	99.2	99.0	99.4
Si 2p-2	102.5	102.7	102.6	102.5	102.4	102.6	102.3	102.8
O 1s	532.1	532.5	532.4	532.1	532.2	532.4	532.2	532.5
S 2s-1	227.8	228.2	228.2	227.7	227.6	228.2	228.2	227.7
S 2s-2	231.2	231.7	232.3	231.0	231.5	231.9	232.2	232.1
Pd $3d_{5/2}$-1	337.6	338.2	338.0	337.5	337.8	338.2	337.6	337.7
Pd $3d_{5/2}$-2			336.2	335.7	335.6	336.3	335.6	335.6
Auger Peak	325.6	324.4	324.8	325.7	325.2	324.6	325.8	326.1

S 2s binding energies ranged from 227.6 to 228.2 eV for lower binding energy peaks (denoted as S-1) and for the higher binding energy peaks it was from 231.0 – 232.3 eV (denoted as S-2). S-1 peaks of S 2s are at a binding energy corresponding to a thiol on the surface.[33] But the form of S-2 sulfur is not as clear. Pd 3d binding energies ranged from 335.4 to 338.2 eV,

state 1 Pd peaks in the 337.5 – 338.2 eV binding energy range and state 2 Pd peaks reside in the binding energy range of 335.6-336.2 eV. The C 1s peak (Figure 4-9) at 285 eV is due to the presence of aliphatic carbon chain and the peak at higher binding energies (at around 287.0 eV) corresponds to the carbonyl carbon from $Pd(OAc)_2$. This suggests the presence of an acetate group on the surface, likely due to the presence of $Pd(OAc)_2$.

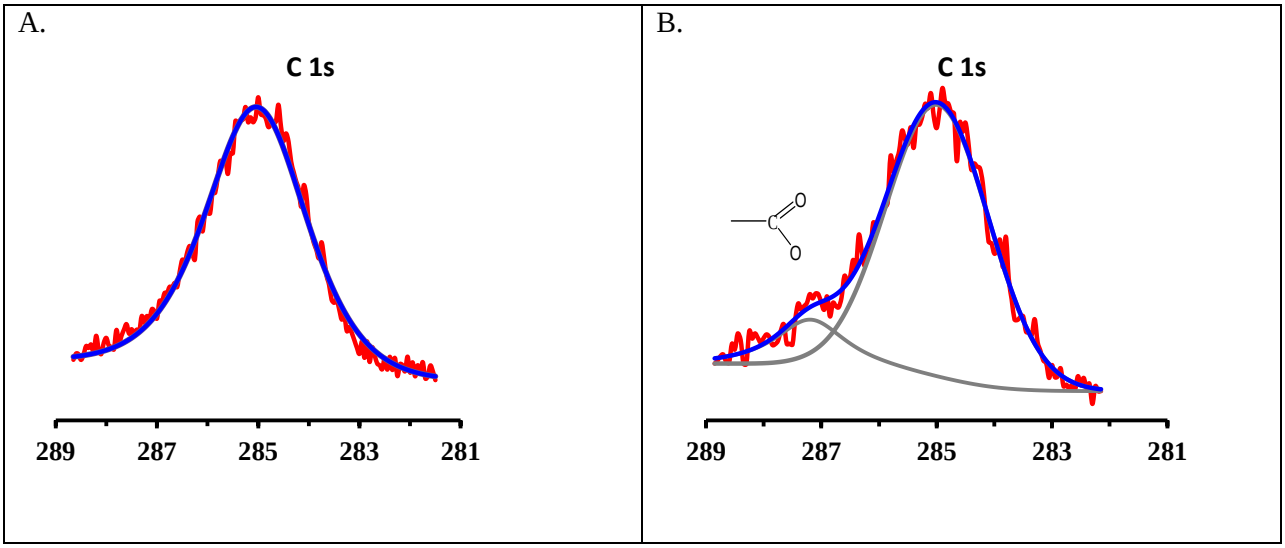

Figure 4-9: XPS peaks of C1s, (A) before Pd loading, and (B) after Pd loading.

Quantitative analysis of the elements present on the prepared palladium catalysts was also performed. Table 4-4 presents the percentage of Pd and S on each surface. These were calculated based on the peak area of each element and atomic sensitivity factors.[33] However, in general the quantity of Pd increased with increasing deposition time. We also compared the intensity of the state 1 Pd peak with those of state 2 and S peaks. It is seen from the table that the relative amount of the State 2 Pd peak becomes greater at longer deposition time. A similar observation is made for the S-2 peak compared to the S-1 peak. But when we compared the total amount of Pd with

S, we see that these values (Pd:S) are changing as well. Literature reports show that, in this type of catalyst, catalytic activity and leaching was calculated as a function of S to Pd ratio.[21] They found the highest yield for the catalysts with S:Pd ratio of 2.1 and that at this ratio and above resulted in minimum leaching. In our case, the S:Pd ratios for those catalysts exposed to solution for 60 minutes or greater are close to 2. This is consistent with each Pd atom being bound to two S atoms. Therefore, we used our model catalyst in the Suzuki-Miyaura reaction that was prepared with 60 minutes deposition time.

Table 4-4: Elemental analysis of the catalyst surfaces.

Name	**% Pd**	**% S**	**S : Pd**	**Pd (State 1 : state 2)**	**S-1 : S-2**
5 min	0.5	3.0	**5.7**		4.1
10 min	0.7	2.6	**3.9**		4.0
20 min	1.4	2.7	**1.9**	7.3	3.3
40 min	1.6	2.5	**1.6**	4.0	5.0
60 min	1.3	2.8	**2.1**	3.3	2.0
80 min	1.1	2.3	**2.0**	6.1	1.9
120 min	1.6	3.2	**2.0**	2.1	2.0
5 hours	0.4	1.4	**3.9**	1.8	0.5

Water contact angle measurements were also carried out after Pd deposition. Figure 4-10 shows the water contact angles of Si wafers after each step of preparation. It is clear that after Pd loading on the thiolated surface, the water contact angle changed from 71±2° to 98±2° i.e. the surface became more hydrophobic. Wenzel[34] defined the relationship between surface roughness and wettability i.e the chemically hydrophobic surface will become even more hydrophobic if the surface roughness is increased. Therefore, an increase of contact angle value is likely due to the presence of acetate groups and increased surface roughness.

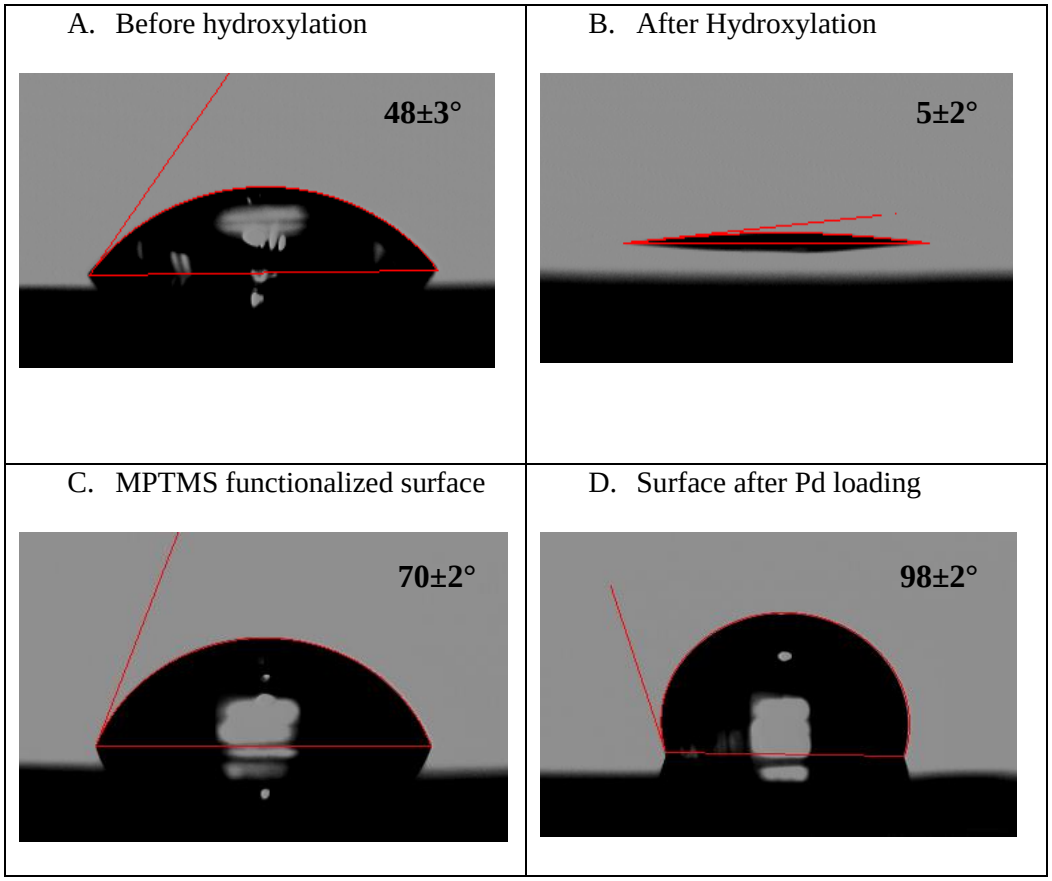

Figure 4-10: Measured water contact angle of Si wafer substrate before and after modification.

4.3.1.2 Suzuki-Miyaura reaction

The catalytic ability of the prepared model catalysts were investigated using those in the Suzuki-Miyaura reaction. In the Suzuki-Miyaura reaction (Scheme 1), the catalysts were able to activate the aromatic halides under mild reaction conditions (60-70°C). The results of Suzuki cross-coupling reaction are given in table 4-5. Reaction conversion was calculated using the GC-MS results. The highest yield achieved was 22% with 1-iodo-4-methylbenzene. This low yield is due to the smaller surface area of the model Pd catalysts compared to the mesoporous silica supported Pd catalysts. The model catalysts were further analyzed by XPS to investigate the changes on the surface.

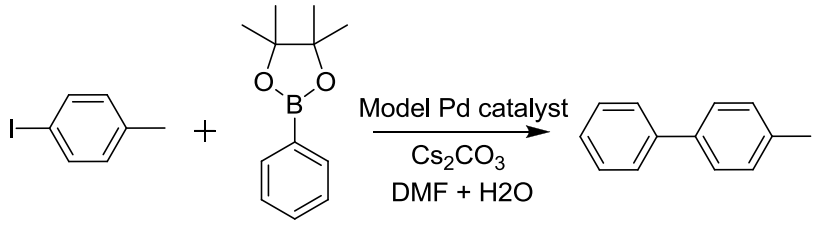

Scheme 1. The Suzuki-Miyaura cross-coupling reaction.

Table 4-5: Suzuki-Miyaura reactions using the model Pd catalyst.

	Substrate	Boronic Acid	Base	Solvent	Time	Temp.	Yield
1	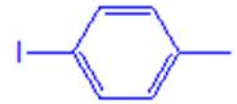	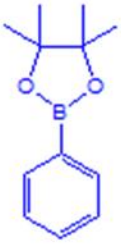	Cs_2CO_3	DMF 1.8mL + H_2O 0.2mL	18h	65-70°C	**22%**
2	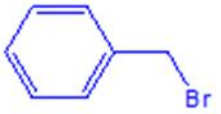						6%
3	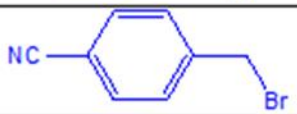						4.5%
4	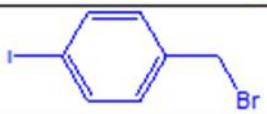						1%
5	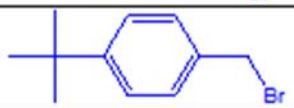						2%
6	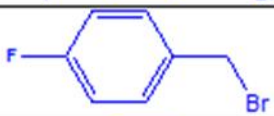						5.2%
7	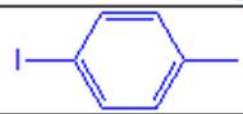		**K_2CO_3**				Trace

Model catalysts were also characterized after using them in the Suzuki-Miyaura coupling reaction. Table 4-6 shows the XPS binding energies catalysts before and after using in the coupling reaction.

Table 4-6: XPS binding energies (eV) of the model Pd catalysts before and after reaction.

XPS peak Name	**Fresh Catalyst Peak BE**	**Used Catalyst Peak BE**
C1s	285.0	285.0
C1s-1	287.1	
Pd3d-1	337.6	337.2
Pd3d-2	335.6	335.8
S2s-1	227.9	228.0
S 2s-2	231.9	231.8
Si2p-1	99.4	98.7
Si2p-2	102.7	102.6
O1s	532.4	533.0
Cs3d		726.6
I3d		619.7
Pd MNN	325.2	325.9
α´	662.9	663.1
	660.8	661.7

Figure 4-11 shows the AFM images of the model Pd catalysts before and after using in the coupling reaction. It is seen from the images that following reaction the surface roughness is reduced. This would be consistent with leaching of the Pd during the reaction.

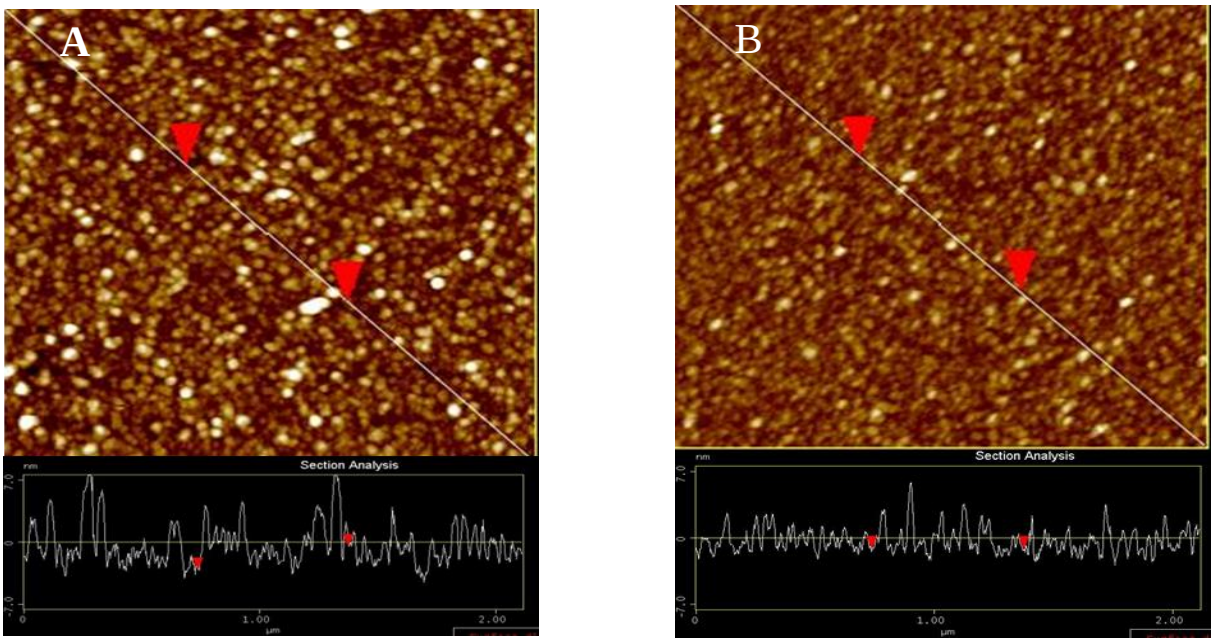

Figure 4-11: AFM images of the model catalysts (A) before and (B) after Suzuki-Miyaura coupling reaction.

So far, in this chapter, the conditions of making a model heterogeneous Pd catalyst on Si wafer surface have been discussed. The model Pd catalyst prepared here successfully used in the Suzuki-Miyaura coupling reaction. However, the nature of the new peaks of Pd and S, the change of the catalyst surface after the reaction, and the influence of State 1 and State 2 in the cross-coupling reaction are not fully explored. The following discussion is an effort to better understand these new species as well their contribution to the organic coupling reaction. In this effort, the influence of the solvent in the catalyst preparation has also been discussed.

4.3.1.3 Part Two: Controlled experiment of Model Pd-Catalysts

In this part, model heterogeneous Pd catalysts were prepared with a range of deposition conditions, summarized in table 4-1. This has been done in an effort to determine the effect of deposition condition on both the physical characteristics of the catalyst, and its activity. Scheffé's simplex-lattice experimental design[35] for three components was used in this study. Because, detailed study of a chemical process using a typical single factor experiment often requires a large number of experimental runs. In addition, many single-factor dependencies often cannot be combined into one. This experimental design is a special type of response surface experiment in which the variable factors are temperature, the amount of THF in THF-ethanol mixture, and time; the response is a continuous function of the proportions of each factor. In such a problem with 3 variables, a simplex-lattice is a uniformly spaced set of points in a regular-sided figure with 3 vertices (triangle) in 2 dimensions[36] that can be visualized by a ternary plot. The visualization clearness and simplicity of interpretation of such diagram result in wide use of this experimental design especially in materials science.[37]

Thus, in order to obtain an insight of how several factors simultaneously affect the characteristics of the catalyst, we used Scheffé's experimental design methodology[22] to explore the influence of three independent variables: temperature, solvent composition and exposure time. In the following, these results are presented as ternary diagrams. Figure 4-12 represents a schematic ternary diagram. The dashed line outside the triangle represents the direction of each parameter and the lines inside the triangle with arrow display how to read the corresponding values.

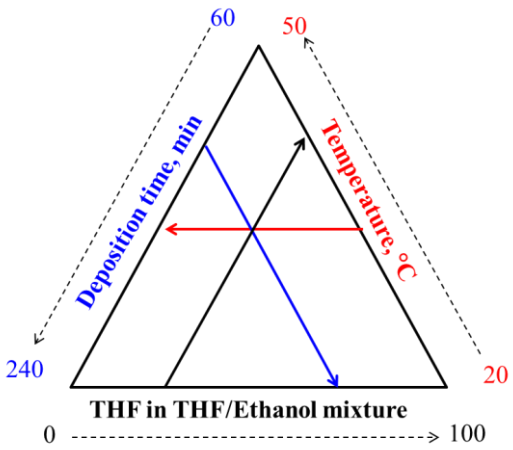

Figure 4-12: A schematic guideline to read the data in the ternary diagram.

The fresh model catalysts were then used to catalyze the Suzuki-Miyaura cross-coupling reaction of iodotoluene with phenylboronic acid pinacol ester (Scheme 1). After the reaction, the catalyst surfaces were characterized by XPS in order to track the changes occurred as a result of the reaction. The dependence of the yield of coupling product (4-methylbiphenyl) in typical Suzuki–Miyaura cross-coupling reaction on the conditions of catalyst preparation is shown in Figure 4-13A. It is important to highlight that the conditions mentioned in Figure 4-13 and in the following ternary diagrams refer to the Pd deposition onto the MPTMS-terminated substrate, i.e. the catalyst preparation conditions; they do not refer to the conditions under which the Suzuki-Miyaura reaction itself was carried out. The experimental section describes the condition of the Suzuki-Miyaura reaction, which remain the same for all the reactions.

A catalyst prepared at low temperature in pure THF for 1 hour shows fair efficiency. It is seen from the ternary diagram that when both the amount of ethanol in THF-ethanol mixture and the temperature are increased, but the time of catalyst preparation remains minimal (1 hour), the

efficiency of the catalyst increases. Thus, the product yield is near 15% when the catalyst was prepared at 35°C in 50 vol% THF/ethanol during 1 hour. The highest yield is observed when the catalyst was prepared at 50°C in pure ethanol during 1 hour. The increase of deposition time at slightly elevated temperatures has almost no influence on the efficiency of the catalyst. However the increase of deposition time at higher temperatures and ethanol concentrations result in significant efficiency decrease. Thus a local efficiency minimum is observed when the catalyst is prepared at 38°C in 90 vol% ethanol/THF during 114 minutes.

Figure 4-13B represent the turnover numbers of the model Pd catalysts. Turnover numbers were calculated considering the amount of product per amount of loaded Pd.[38] The quantity of palladium present in the model catalysts surface was estimated from the XPS-determined S:Pd ratio, assuming that a complete SAM on silica contains 5 silane molecules per nm^2.[39 40] It is clear from Figure 4-13B that the highest turnover numbers were observed on those catalysts prepared under conditions of lower deposition temperature (23° – 38°C), higher deposition time (more than 132 minutes), and higher THF concentrations (more than 50% THF). It is interesting that highest yield was not achieved with the same conditions. However, the catalysts gave somewhat higher yields associated with the same conditions that led to high turnover number.

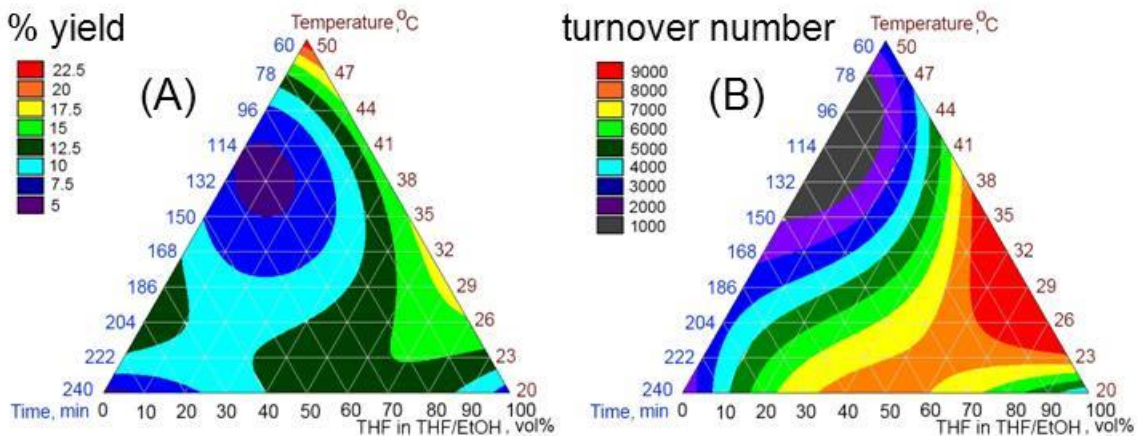

Figure 4-13: Ternary diagrams as a function of catalyst preparation conditions showing (A) %yield and (B) turnover number.

To determine what the processes take place on the surface during the palladium deposition, and acquire a deeper understanding of their further influence on the Suzuki–Miyaura cross-coupling reaction, XPS data analysis was visualized in form of ternary plots.

Each catalyst was characterized using XPS and XAES both prior to and following its use in the cross-coupling reaction. Table 4-7 contains the XPS binding energy, the Auger kinetic energy, and the Auger parameter of 10 modelcatalysts. All of the catalysts were found to have binding energies in the range of 335.7 eV to 338.2 eVand their Auger kinetic energies were in the range of 324.0 to 326.2 eV. State 1 Pd species were found in the range of 337.8 to 338.2 eV and corresponding Auger parameter were in the range of 662.1 to 664.3 eV. The binding energy of state 2 Pd was found to be in the range of 335.7 – 336.1 eV and corresponding calculated Auger parameter (α') were in the range of 660.1 to 662.0 eV. Therefore, it is evident that the nature of Pd species (state 1 and state 2) is different.

Table 4-7: Binding energies (eV) and kinetic energies (eV) of fresh the model Pd catalysts

Fresh Pd Catalysts					
Sample #	**XPS BE**		**Auger KE**	**α´1**	**α´2**
	Pd-1	**Pd-2**	**Pd MNN**		
1.0	337.9	335.7	326.1	664.0	661.8
2.0	338.0	336.0	324.0	662.0	660.0
3.0	338.2	335.7	324.8	663.0	660.6
4.0	338.0	335.8	325.5	663.4	661.2
5.0	337.8	335.7	324.3	662.1	660.0
6.0	338.1	335.8	326.2	664.3	662.0
7.0	338.0	335.8	325.6	663.6	661.4
8.0	338.2	335.9	324.5	662.7	660.4
9.0	338.0	335.7	325.5	663.5	661.2
10.0	338.0	335.7	324.7	662.7	660.4
Average	338.0 ± 0.2	335.8 ± 0.1	325.1 ±1.1	663.1 ± 1.1	661.0 ± 1.0

Table 4-8 represent the XPS and AES data of the catalyst after using in the Suzuki-Miyaura coupling reaction. Pd $3d_{5/2}$ peaks of all of the used catalysts in our study were recordedin the range of 335.8 to 338.1 eV. It is interesting to note that following the reaction the position of Pd $3d_{5/2}$ peaks of both the Pd states were shifted. State 1 Pd species were found to be

in the range of 337.1 to 338.1 eV and state 2 Pd species were found in the range of 335.8 to 336.5 eV.

Table 4-8: Binding energies (eV) and kinetic energies (eV) of used the model Pd catalysts and their Auger parameter values.

Used Pd Catalysts					
Sample #	**XPS BE**		**Auger KE**	**α´1**	**α´2**
	Pd-State 1	**Pd- State 2**	**Pd MNN**		
1.0	337.8	335.8	325.3	663.1	661.1
2.0	337.7	336.1	325.5	663.2	661.6
3.0	337.9	336.5	325.9	663.8	662.4
4.0	337.5	336.1	326.6	665.1	662.8
5.0	337.1	336.1	325.5	662.6	661.6
6.0	338.0	335.8	324.9	662.9	660.7
7.0	337.7	336.4	325.2	662.9	661.6
8.0	337.9	336.6	325.5	663.4	662.1
9.0	337.3	336.2	325.4	662.7	661.6
10.0	337.7	336.1	325.5	663.2	661.6
Average	337.8 ± 0.3	336.2 ± 0.25	325.5 ± 0.4	663.3 ± 0.7	661.7 ± 0.6

Table 4-9 contains the quantitative data of the model catalysts before and after reaction. The data from the table gives us an idea about the catalytic activity of the model catalysts and the

leaching phenomena. The highest yield recorded was 22%, this small number is likely due to the smaller surface area of the catalyst. The turn over number was also calculated (table 4-9). The table also contains the ratio of State 1 and State 2 Pd species in the fresh model catalysts. There was a huge loss of Pd during the reaction as seen from the table and the most lost species corresponds to State 2 Pd. Some of the catalysts were also reused in the second run. All of the catalysts were found to be active in their second run.

Table 4-9: Quantitative analysis of the model catalysts before and after reaction.

Sample #	**S:Pd ratio**		**Yield, %**		**Turn Over Number (TON)**		**Surface Pd Concentration (nmol/cm^2)**		**State 1 / State 2**
	Fresh Catalysts	**Used Catalysts**	**After First Run**	**After Second Run**	**After First Run**	**After Second Run**	**Fresh Catalysts**	**Used Catalysts**	
1	0.4	2	22	6	3700	5040	2.08	0.42	2.0
2	1.8	3.2	16	5	12100	6720	0.46	0.26	6.1
3	0.4	1.2	5	5	8400	2520	2.08	0.69	1.0
4	0.7	3.4	11	3	3230	4280	1.19	0.24	1.0
5	1.7	3	8	7	5710	8820	0.49	0.27	1.5
6	1.1	2.8	4		1900		0.76	0.3	1.3
7	1.6	3	6		4047		0.52	0.28	1.0
8	1.2	2.6	14		7083		0.69	0.32	5.7
9	2.1	5	9		7968		0.4	0.16	2.5
10	1.5	4.1	12		7588		0.55	0.2	1.2

Figure 4-14 shows the Pd 3d XPS spectrum of Sample 1, before and after use in the Suzuki cross-coupling reaction. Model catalysts surfaces (fresh and used) were also compared to

the XPS spectrum of the $Pd(OAc)_2$ and to the spectrum of a sample catalyst exposed to a solution of 1-iodo-4-methylbenzene in DMF solvent at reaction temperature (i.e. reaction conditions but with only one of the two reactants present). The Pd $3d_{5/2}$ spectrum of $Pd(OAc)_2$ was found at 338.5 eV, consistent with previous reports for this compound.[41] It is clear from the spectra that the model catalysts clearly possesses two chemical states of Pd. Interestingly, both states of Pd shiftedafter the reaction, and in addition they shifted in the opposite direction. Similar spectra were obtained from the remaining catalyst samples (Complete list of binding energies is given in table 4-7 & 4-8).

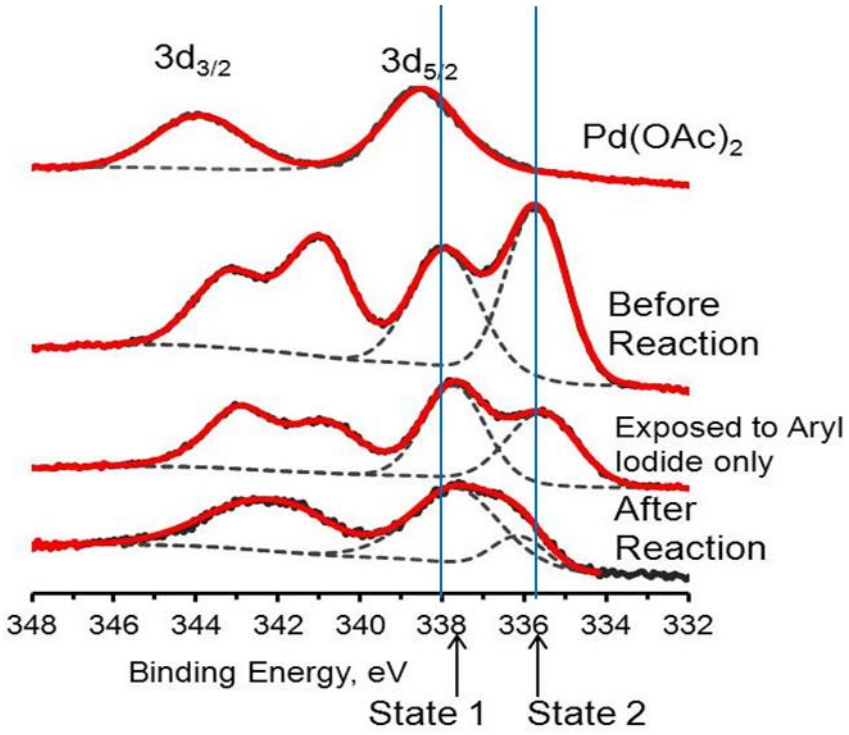

Figure 4-14: Pd 3d X-ray photoelectron spectra of the Suzuki-Miyaura coupling catalysts.

In all catalysts samples, the position of the two Pd peaks was similar but there were significant differences of the relative intensities of these two chemical states of Pd. The relative

intensities of State 1 Pd (higher binding energy peak) with respect to State 2 Pd (lower binding energy peak) on the unused catalysts are presented in the ternary diagram (Figure 4-15A). It is seen from the figure that state 1 dominates lower right corner of the diagram, where the catalysts were prepared under low temperature deposition conditions in the solutions of high THF concentrations. These catalysts also led to high turnover numbers and relatively higher % yields in the cross-coupling reactions. State 2 Pd dominates on the catalysts prepared under higher temperature (30° - 40°C) in the solutions where THF concentrations are 70% or lower amounts. The catalysts where State 2 dominates give the highest turnover numbers and higher yield as well. It is important to note that, upon reaction, the total amount of Pd in all catalysts samples decreases, as indicated in figure 4-15B. This ternary diagram shows the ratio of the total Pd $3d_{5/2}$ signal before and after reaction. In Figure 4-15B, the bigger values are in the upper left corner indicate the higher loss of Pd and smaller values are in the lower right corner of the diagram indicate the smallest loss of Pd. Therefore, the smallest loss of Pd is associated with the catalysts prepared under low temperature and high THF concentration, where essentially State 1 Pd dominates. So, State 1 Pd is preferentially retained on the surface relative to State 2, following the cross-coupling reaction.

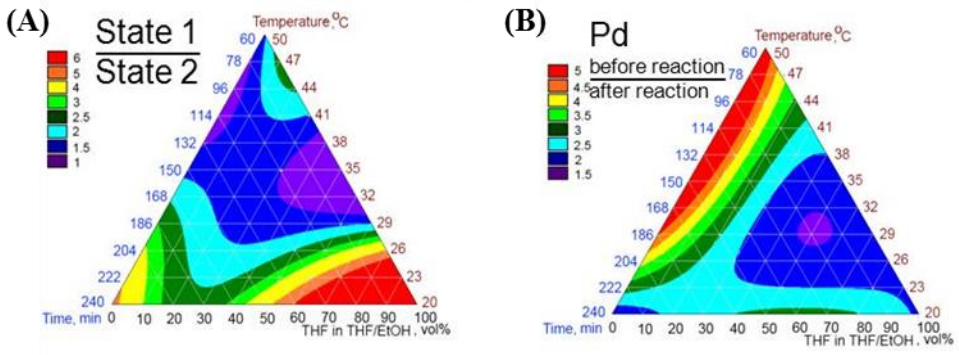

Figure 4-15: Ternary diagrams as a function of catalyst preparation conditions showing (A) the ratio of the Pd $3d_{5/2}$ peak area of State 1 and State 2 prior to reaction and (B) ratio of the total Pd $3d_{5/2}$ peak area before and after reaction.[31]

Since the Pd on the model catalysts surfaces are attached to the Si surface through the MPTMS ligand, the nature of S was investigated with similar importance. For each model catalyst S 2s photoelectron spectra was collected. Representative S 2s spectra exposed in different conditions are shown in figure 4-16. Figure 4-16A shows the S 2s spectra of bare MPTMS-modified surface (i.e. prior to Pd deposition), a sample catalyst (sample 1) exposed to a solution of 1-iodo-4-methylbenzene in DMF solvent at reaction temperature, before and after use in the Suzuki cross-coupling reaction. The total S:Pd atomic ratio of the catalyst (as determined from the relative intensities of the S 2s and Pd $3d_{5/2}$ XPS peak areas) prior to reaction are presented in the ternary diagram and shown in the figure 4-16B. It is seen from this figure that the higher S;Pd ratio is associated with the lower part of the ternary diagram. The catalyst have higher S:Pd ratio generally associated with the same sample preparation conditions that lead to higher turnover numbers and dominance of Pd State 1on the catalyst surface.

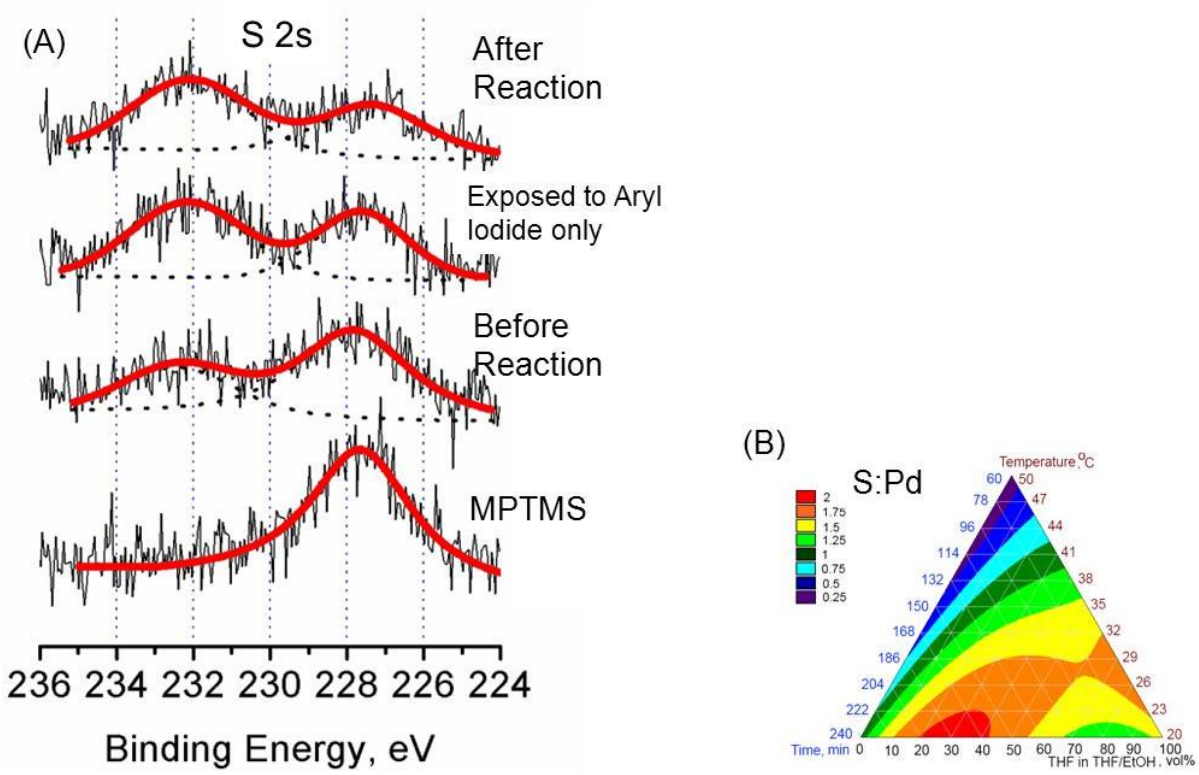

Figure 4-16: (A) S 2s X-ray photoelectron spectra of the Suzuki-Miyaura coupling catalysts; (B) Ternary diagram as a function of catalyst preparation conditions showing the S:Pd atom ratio on the catalyst prior to reaction, as determined using XPS.[31]

Before immobilizing Pd on the MPTMS modified surface, the S 2s spectrum shows the presence of a single S state, at a binding energy of 227.7 eV. After Pd loading, the initial S 2s peak remains in the same position with reduced intensity and a second peak at binding energy of 231.7 eV is observed. While this higher binding energy state generally appeared to become stronger in intensity following the cross-coupling reaction, the relatively low signal-to-noise of the S 2s spectra precluded any full analysis using the ternary diagrams as was carried out for Pd.

A number of reports of Pd XP spectra on catalysts supporting the Suzuki-Miyaura reactions are available in the literature and these have largely focused on thiol-terminated silica and mesoporous silica-supported catalysts such as SBA-15-SH or MCM-21-SH.[9-11,16,21,42] In those catalysts, the presence of either one or two chemical states of Pd have been reported and they are more likely in binding energies to those of State 1 and State 2 observed in the current model catalyst here. Typically State 1 and State 2 have been assigned as Pd(II) species and Pd(0) species respectively.[32a] The shifts in binding energy may also take place while the catalyst has undergone reaction. In these cases, $Pd(OAc)_2$ has been used as the starting material from where Pd got down on the surface and THF has been used as the solvent. The use of alcohols as a deposition solvent has been reported.[43] The use of ethanol has also been reported as a reducing agent as well as the solvent which led to Pd(II) reduction and the formation of Pd(0) species in the form of nanoparticles.[44] In the current experiment, the influence of THF/ethanol solvent mixtures has been explored. On the other hand, in the case of reducing $PdCl_2$ or $Pd(acac)_2$ using H_2 on carbon black or MgO supports, peaks similar in binding energy to State 2 have also been observed, and again have been assigned to Pd(0) species.[45]

Therefore, to better understand the nature of the various forms of Pd present on our model catalyst, and provide some insight into these previous reports, the Wagner plot concept was used here. The Wagner plot has been made by plotting our current XPS data in the X-axis and XAES data in the Y-axis. A number of well-characterized compounds have also been put together in the same Wagner plot. The Wagner plot in Figure 4-17 is a plot of the XAES kinetic energy data versus XPS binding energy for a given species. The calculated Auger parameter (α') is shown as diagonal lines in the figure. More information about the Wagner plot and the Auger

parameter are available in Ch. 2. For systems noted above, in many cases the lack of XAES data preclude their inclusion in the Wagner diagram. In the Wagner plot (Figure 4-17), the data collected in the current experiments are presented as the colored data points and the black points represent data previously reported in the literature, including data from the SBA-15-SH-supported Pd catalysts previously described by our group.[16]

The Wagner plot shows that State 1 is at higher binding energy and State 2 at lower binding energy. The filled green circle is the position of State 1 before reaction and open circle is after reaction, showing a shift to the lower binding energy. State 2 shifted in the opposite direction after the reaction. We compared our data with several other species: metallic Pd, which is evidently in the Pd(0) oxidation state and PdO which is formally a +2 oxidation state. We have also compared to the $Pd(OAc)_2$, which is the species from which Pd was initially deposited on the surface. It is seen from the Wagner plot that State 1 peaks do not bear close relation with the $Pd(OAc)_2$. So, evidently $Pd(OAc)_2$ reacts once it is deposited on the surface.

In the Wagner plot, the position of State 1 Pd appears close to the region corresponds to the Pd species that has been previously observed by our group on SBA-15-SH supported Pd catalyst. At that time, it was assigned as a "Pd (II)" species: either unreacted $Pd(OAc)_2$ or some form of thiol/acetate complex. I also compared State 1 with a series of Pd-thiol compounds; $PdCl_2(DMSO)_2$, $Pd_6(SEt)_{12}$, and $Pd_4(OAc)_4(SEt)_4$. XPS binding energy and Auger kinetic energy are close to those we have observed for the compound $Pd_4(OAc)_4(SEt)_4$ (figure 4-17). In $Pd_4(OAc)_4(SEt)_4$, the Pd centre is surrounded by two (monodentate) acetate and two thiol ligands.[27] All these compounds involve S coordinate to Pd. All of these clusters are in the same

area but none of these are exactly the same. However, all the data cluster in the same region, suggesting that State 1 involves coordination of a Pd atom to the S. Following reaction, State 1 shifted to the lower binding energy. A similar situation was observed and reported in the previous work from our group on the real catalyst (the SBA-15-SH supported Pd). At that time, the Pd peak after the reaction had originally been assigned to the Pd nanoparticles[16], because it shifted to the lower binding energy, i.e. more metallic. But given the presence of the State 2 peak at even lower binding energy, we need to revise that assignment. Instead, the slight shift upon reaction likely reflects the loss of acetate from the surface, and the consequent greater co-ordination of the Pd(II) species to sulfur. As S is more polarizable, the shift to lower binding energies is consistent with an increase in extra-atomic relaxation, as described in Eq. 2.5 earlier in this thesis.

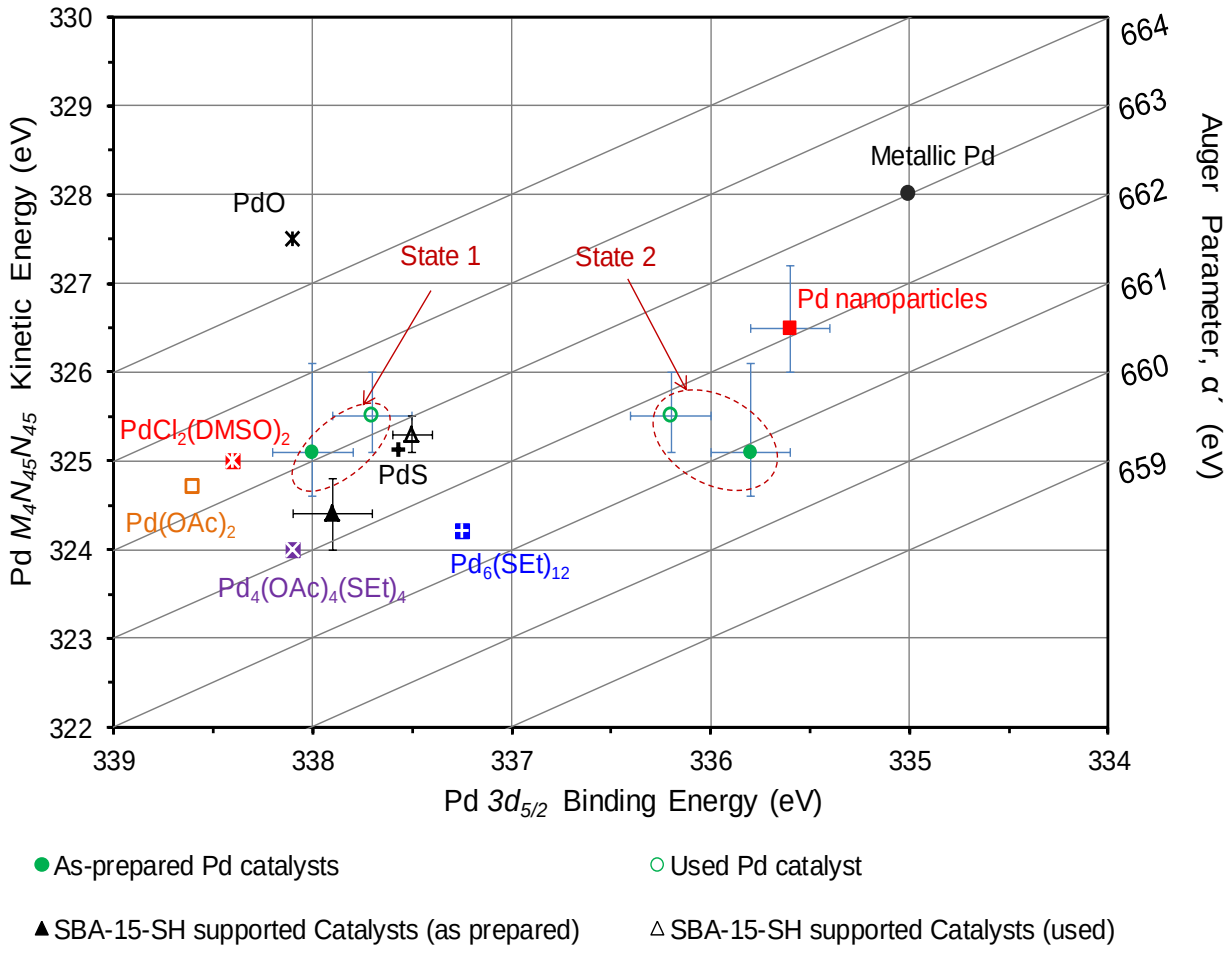

Figure 4-17: Wagner chemical state plot for Pd $3d_{5/2}$ XPS and Pd MNN Auger electron spectroscopy data. Colored symbols represent data reported here; black symbols are data reported previously elsewhere. Two chemical states were observed for the model catalysts used here, denoted state 1 and state 2. In the case of the SBA-15-SH catalysts (triangles) and the model catalyst developed here (circles), measurements were carried out on multiple samples prepared under differing conditions. The error bars reflect the range of binding energy and Auger kinetic energy values observed.[31]

State 1 cannot correspond to a Pd nanoparticle on the model catalyst here: as will be discussed below, there is strong evidence from both XPS and SEM data that it is State 2 that corresponds to Pd nanoparticles on the surface. After using in the cross-coupling reaction, the binding energy and Auger kinetic energy of State 1 correspond closely to those of PdS (Figure 4-17); probably Pd undergoes further loss of acetate ligands upon participating in the coupling reaction. As catalysts in which State 1 is the main Pd species present exhibit high turnover numbers and generally higher yields, and State 1 is preferentially retained on the catalyst surface following the coupling reaction, State 1 must correspond to the active Pd species in the Suzuki-Miyaura coupling reaction. A species similar in binding energy to State 1 was previously observed using Pd foil as the catalyst.[17] This was attributed to insertion complex of the aryl iodide to Pd. In case of the model Pd catalysts, exposure of the catalyst to the aryl iodide alone under reactions conditions resulted in a relatively unchanged Pd 3d spectrum (figure 4-15A), a trace quantity of iodine was observed in the I 3d XPS spectrum (figure 4-18) suggesting the formation of an oxidative addition product.

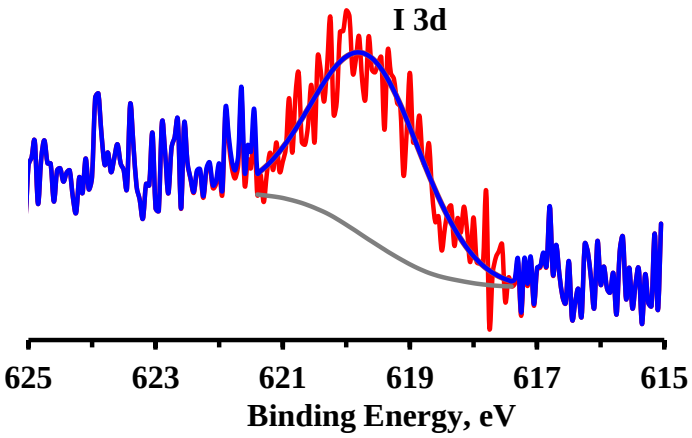

Figure 4-18: I 3d XPS peak on the model Pd catalyst after using in the cross-coupling reaction.

The State 2 species demonstrates a similar binding energy to those values previously reported in the literature as corresponding to a "Pd(0)" species and generally assigned to metallic Pd, or to Pd nanoparticles. Therefore, the model catalyst surface was characterized by the SEM and the images with particles size distribution are shown in figure 4-19. It is seen from the images that fresh catalysts contain Pd nanoparticles with the average diameter of 14 nm and following reaction the average particles diameter is reduced to 10 nm. This is consistent with the XPS data: following reaction, the particles shrink in size, leading to the observed decrease in the overall Pd signal, as seen in the ternary diagram in Figure 4-15B. Following reaction the XPS peak also shifts to higher binding energy, as the smaller particles provide a less polarizable environment for the ionized Pd atom, leading to reduced stabilization of the core hole, and eventually more reduced R_{ea} value than the larger Pd nanoparticles.

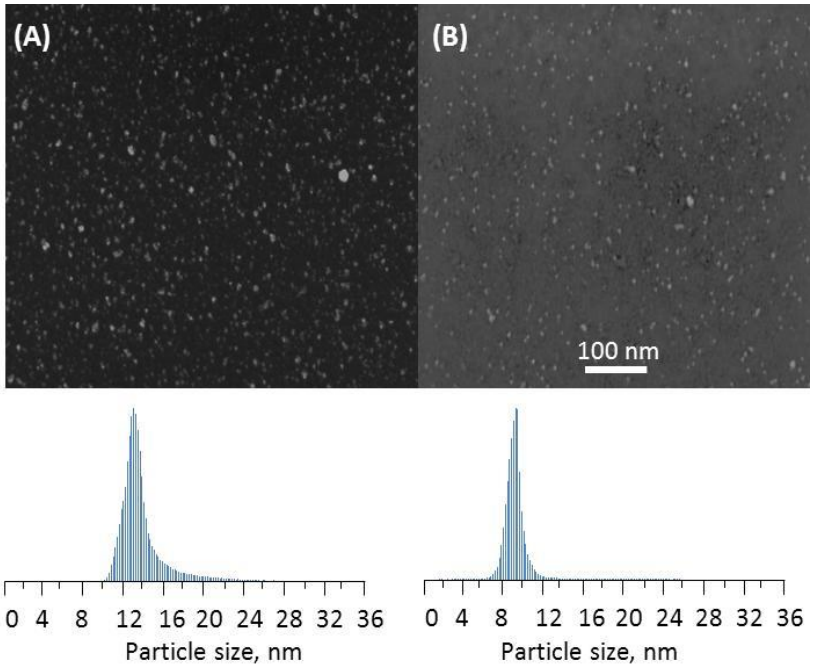

Figure 4-19: SEM images of the model catalyst surfaces (A) prior and (B) subsequent to use in the Suzuki-Miyaura coupling reaction. The accompanying histograms show the particle size distribution.[31]

There are relatively few data available on sulfur XP spectra for thiol-supported Pd catalysts used in Suzuki-Miyaura reactions. However, the S 2s peak at 227.7 eV is from the thiol on the surface itself, indicating that unreacted S sites remain on the surface. The intensity of this peak was reduced once Pd was immobilized. The presence of unreacted S is inconsistent with previous reports on mesoporous silica catalysts, in which only one S chemical state was observed under any given conditions.[16,32a] The presence of unreacted S sites likely due to the substrate preparation methods: as illustrated earlier, the C:S area ratio at the surface indicated that the surface MPTMS molecules were not completely hydrolyzed; however, any degree of cross-

linking on the surface might lead to SH groups being overlaid by further MPTMS, making these SH sites unavailable for bonding with Pd. The S peak at 232 eV is at a binding energy not commonly reported in the literature: to the best of our knowledge, this kind of S peak has only been reported once before, for a Pd catalyst supported on sulfur-terminated GaAs(001).[46] Similar to our model catalyst, they found that the S *1*s peak (using a synchrotron X-ray source) associated with unreacted S sites on the surface remained present following deposition of Pd. They also observed a second state, shifted some 7 eV to higher binding energies, and trace amounts of S species at intermediate binding energy. Nonetheless, the authors did not precisely assign these peaks. As S 2s is not the photoelectron transition routinely acquired in XPS, there is also little data available in the literature on S 2s binding energies of other species. Therefore, in order to assign the S 2s peaks on the model catalysts, the S peaks of a whole series of different S compounds were analyzed: we acquired S 2s binding energy spectra for the compounds $Pd_6(SEt)_{12}$ and $Pd_4(OAc)_4(SEt)_4$ as well as surface-bound S species of varying oxidation state. Figure 4-20 shows the S XP spectra of sample one and others as prepared surfaces.

It is seen from Figure 4-20 that the S 2s binding energy for the new peak does not correspond well to that in $Pd_6(SEt)_{12}$ and $Pd_4(OAc)_4(SEt)_4$. The oxidation state of S in these two compounds is formally -2. The position of R-S-S-R and R-S-Ac also do not correspond with the new peak of the model catalysts. The S oxidation states of surface-bound disulfide (R-S-S-R) or alkylthioacetate are formally -1 and -2 respectively. But the sulfonate-terminated surface exhibit a peak at a binding energy higher that the new peak of the model catalyst and the compound has a formal oxidation state of +6. The compound that seems closest to the binding energy for S in

the compound $PdCl_2(DMSO)_2$ in which the S of the DMSO ligand is formally in a +2 oxidation state and has been shown to be the donor site to the Pd center.[26] This is consistent with our previous inference of a +2 oxidation state of S in SBA-15-SH-supported Pd catalysts.[16]

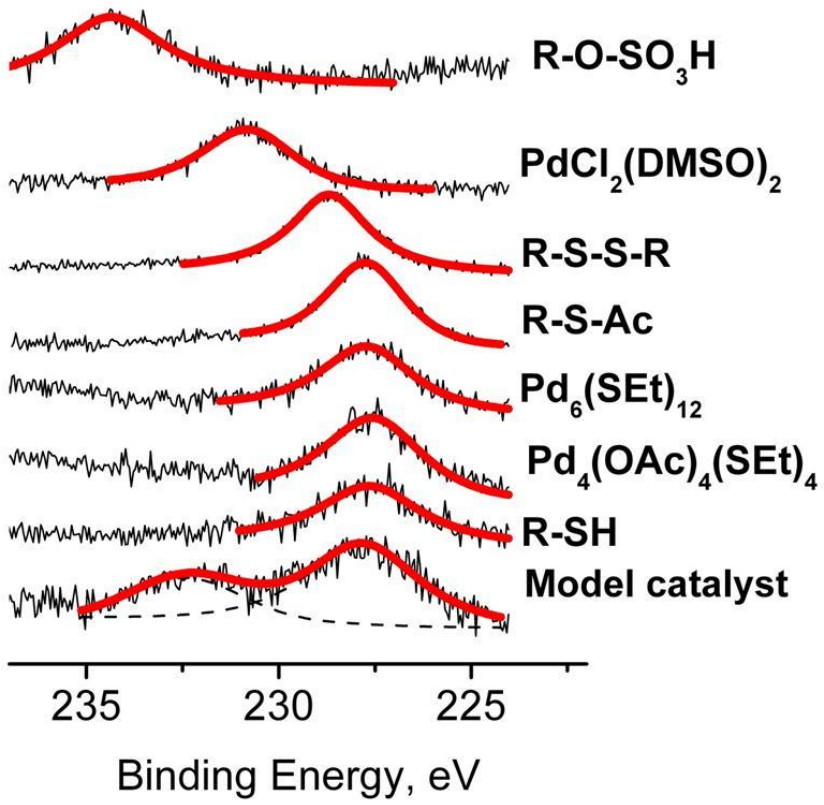

Figure 4-20: Comparative S 2s X-ray photoelectron spectra of the model catalyst with that of other compounds exhibiting Pd-S bonding ($Pd_6(SEt)_{12}$, $Pd_4(OAc)_4(SEt)_4$, and $PdCl_2(DMSO)_2$), surface-bound S species (alkylthioacetate, R-S-Ac, disulfide, R-S-S-R, sulfonate R-O-SO_3H, and thiol, R-SH) of different oxidation states.[31]

Therefore, all the Pd XPS results along with these S XPS results, suggest that when $Pd(OAc)_2$ comes in contact with the thiol terminated surface, the S species on the surface is formally oxidized. As a result, Pd gets reduced in the form of Pd nanoparticles and a S-bound Pd complex, as shown schematically in the figure 4-21. Catalysts prepared at lower temperatures and solutions of higher THF concentration lead to preferential formation of the S-bound Pd complex (State 1), which appears to be the reactive species in the Suzuki-Miyaura coupling reaction. This species also appears to be more stable than State 2. Solutions with higher ethanol concentrations generate model catalysts where the amount of deposited Pd is significantly higher, but much of this is in the form of the State 2 species, which has been assigned to the formation of Pd nanoparticles. State 2 Pd is preferentially lost when the catalyst is used in the coupling reaction due to leaching shown schematically in Figure 4-21. Pd leaching during the reaction is an undesirable phenomenon even though the leached metal is often considered to be the active species in coupling reactions.[47] This can be correlated with the relatively high %yield associated with the higher-ethanol conditions and the low turnover numbers as the Pd is rapidly lost from the surface.

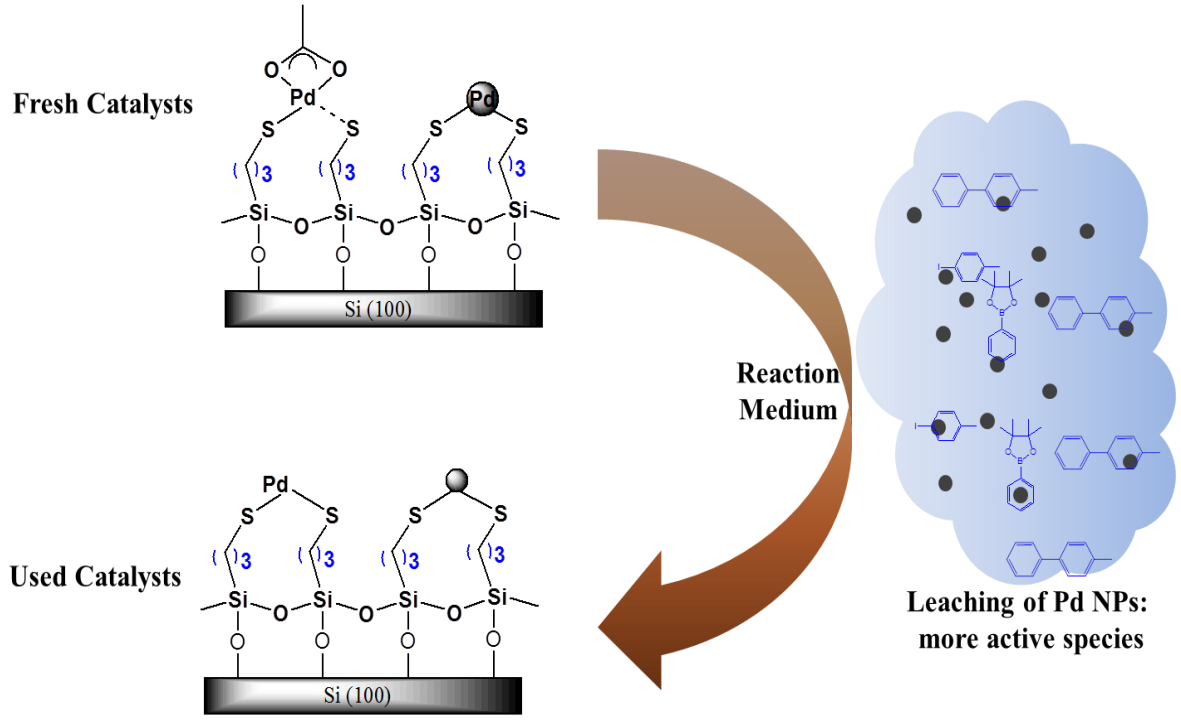

Figure 4-21: Schematic representation of Pd leaching in the reaction medium.

4.4 Conclusions

Needless to say, the Suzuki-Miyaura coupling reaction is one of the most successful synthetic routes for making carbon-carbon bond. While homogeneous Pd catalysts dominate in this field, better understanding of the heterogeneous one still remains a big challenge. This challenge can be addressed by obtaining a clearer picture of processes that take place on the heterogeneous Pd catalyst surface during this reaction, and particularly what Pd species are present and their role in the reaction mechanism. Since the presence of heavy metals is strictly regulated in pharmaceutical ingredients, leaching of Pd into solution must be minimized. Pd is a costly material requires minimization of waste also. In this current approach, model heterogeneous Pd catalyst has been prepared by immobilizing $Pd(OAc)_2$ on a thiol-terminated,

oxidized single-crystal Si(100) substrate. In the first part of this chapter, the deposition condition of Pd on the thiolated surface (single solvent: THF) was optimized and in the second part a more systematic approach with two-solvent (THF and ethanol) system was used to better understand the catalyst and catalytic system. In part one, model catalysts were successfully used in a number of cross-coupling reactions using a variety of substrates (table 4-4). These model catalysts do not exhibit catalytic behavior as efficient as those based on mesoporous silica, presumably due to their relatively small surface area. However, these model Pd catalysts made it easy to better understand the relation of catalytic activity with surface morphology and composition.

XPS data and Wagner plots have shown the presence of two chemical states of Pd on the surface. Similarly two species of S are observed on the surface by XPS. One of the chemical states of Pd was in the form of S-bound Pd(II) species in which the surface-grafted S ligand is formally in a +4 oxidation state and the second state was associated with formation of Pd nanoparticles on the surface. SEM results have shown that the nanoparticle's size decreased following the cross-coupling reaction presumably due to leaching of Pd into solution. The shift of binding energy of the nanoparticles following reaction may be correlated to changes in the extra-atomic relaxation term. Because smaller particles exhibit a less polarizable environment which stabilize the core hole of ionized Pd less effectively. This model system also helps finding that S-bound Pd complex (State 1) was more stable with highest turnover number than that of Pd nanotarticles (State 2). Therefore, it can be summarized that S-bound Pd is most effective catalyst, less prone to undesirable leaching.

4.5 References

(1) Seechurn, C.; Kitching, M. O.; Colacot, T. J.; Snieckus, V. *Angew. Chem. Int. Ed.* **2012**, *51*, 5062.

(2) Garrett, C. E.; Prasad, K. *Adv. Synth. Catal.* **2004**, *346*, 889.

(3) Markham, A.; Goa, K. L. *Drugs* **1997**, *54*, 299.

(4) Yusuf, S. *Am. J. Cardiol.* **2002**, *89*, 18A.

(5) Matheron, M. E.; Porchas, M. *Plant Dis.* **2004**, *88*, 665.

(6) De Vos, D. E.; Dams, M.; Sels, B. F.; Jacobs, P. A. *Chem. Rev.* **2002**, *102*, 3615.

(7) Polshettiwar, V.; Molnar, A. *Tetrahedron* **2007**, *63*, 6949.

(8) Toebes, M. L.; van Dillen, J. A.; de Jong, Y. P. *J. Mol. Catal. A: Chem.* **2001**, *173*, 75.

(9) Shimizu, K.; Koizumi, S.; Hatamachi, T.; Yoshida, H.; Komai, S.; Kodama, T.; Kitayama, Y. *J. Catal.* **2004**, *228*, 141.

(10) Ji, Y. Y.; Jain, S.; Davis, R. J. *J. Phys. Chem. B* **2005**, *109*, 17232.

(11) Crudden, C. M.; Sateesh, M.; Lewis, R. *J. Am. Chem. Soc.* **2005**, *127*, 10045.

(12) Houpis, I. N.; Huang, C. K.; Nettekoven, U.; Chen, J. G.; Liu, R. M.; Canters, M. *Org. Lett.* **2008**, *10*, 5601.

(13) Chemler, S. R.; Trauner, D.; Danishefsky, S. J. *Angew. Chem. Int. Ed.* **2001**, *40*, 4544.

(14) Roy, S.; Plenio, H. *Adv. Syn. Catal.* **2010**, *352*, 1014.

(15) Cookson, J. *Platinum Met. Rev.* **2012**, *56*, 83.

(16) McEleney, K.; Crudden, C. M.; Horton, J. H. *J. Phys. Chem. C* **2009**, *113*, 1901.

(17) MacQuarrie, S.; Horton, J. H.; Barnes, J.; McEleney, K.; Loock, H. P.; Crudden, C. M. *Angew. Chem. Int. Ed.* **2008**, *47*, 3279.

(18) Kohler, K.; Kleist, W.; Prockl, S. S. *Inorg. Chem.* **2007**, *46*, 1876.

(19) Zhao, F. Y.; Shirai, M.; Ikushima, Y.; Arai, M. *J. Mol. Catal. A: Chem.* **2002**, *180*, 211.

(20) Reetz, M. T.; Westermann, E. *Angew. Chem. Int. Ed.* **2000**, *39*, 165.

(21) Webb, J. D.; MacQuarrie, S.; McEleney, K.; Crudden, C. M. *J. Catal.* **2007**, *252*, 97.

(22) Scheffe, H. *Journal of the Royal Society. Series B* **1958**, *20*, 344.

(23) Draper, N. R.; Pukelsheim, F. *Statistical Papers* **1996**, *37*, 1.

(24) Myers, R. H.; Montgomery, D. C. *Response Surface Methodology: Process and Product Optimization Using Designed Experiments.*; John Wiley & Sons: New York, 1995.

(25) Morandi, S.; Caselli, E.; Forni, A.; Bucciarelli, M.; Torre, G.; Prati, F. *Tetrahedron: Asymmetry* **2005**, *16*, 2918.

(26) Price, J. H.; Williamson, A. N.; Schramm, R. F.; Wayland, B. B. *Inorg. Chem.* **1972**, *11*, 1280.

(27) Stash, A. I.; Levashova, V. V.; Lebedev, S. A.; Hoskov, Y. G.; Mal'kov, A. A.; Romm, I. P. *Russ. J. Coord. Chem.* **2009**, *35*, 136.

(28) Stash, A. I.; Perepelkova, T. I.; Noskov, Y. G.; Buslaeva, T. M.; Romm, I. P. *Russ. J. Coord. Chem.* **2001**, *27*, 585.

(29) Shen, C. M.; Su, Y. K.; Yang, H. T.; Yang, T. Z.; Gao, H. J. *Chem. Phys. Lett.* **2003**, *373*, 39.

(30) Aida, T.; Akasaka, T.; Furukawa, N.; Oae, S. *Bull. Chem. Soc. Jpn.* **1976**, *49*, 1441.

(31) Hanif, M. A.; Ebralidze, II; Horton, J. H. *App. Surf. Sci.* **2013**, *280*, 836.

(32) (a) MacQuarrie, S.; Nohair, B.; Horton, J. H.; Kaliaguine, S.; Crudden, C. M. *J. Phys. Chem. C'* **2010**, *114*, 57; (b) Nohair, B.; MacQuarrie, S.; Crudden, C. M.; Kaliaguine, S. *J. Phys. Chem. C'* **2008**, *112*, 6065.

(33) Moulder, J. F.; Stickle, W. F.; Sobol, P. E.; Bomben, K. D. *Handbook of X-ray Photoelectron Spectroscopy*; Physical Electronic Inc.: Minnesota, 1992.

(34) Wenzel, R. N. *Industrial and Engineering Chemistry* **1936**, *28*, 988.

(35) Scheffé, H. *Journal of the Royal Statistical Society. Series B (Methodological)* **1957**, *20*, 344.

(36) Myers, R. H.; Montgomery, D. C. *Response Surface Methodology: Process and Product Optimization Using Designed Experiments*; John Wiley & Sons: New York, 1995.

(37) (a) Wei, H.; Fu, Z.; Mu, J.; Guo, R. C. *Adv. Mat. Res.* **2011**, *284-286*, 219; (b) Takeshita, E. V.; Piantola, F. A.; de Souza, S. M. A. G. U.; Nunes, R. C. R.; de Souza, A. A. U. *J. Appl. Polym. Sci.* **2012**; (c) Krupko, O. V.; Okrepka, G. M.; Shcherbak, L. P. *Funct. Mat.* **2011**, *18*, 224.

(38) Palencia, H.; Garcia-Jimenez, F.; Takacs, J. M. *Tetrahedron Lett.* **2004**, *45*, 3849.

(39) Bunker, B. C.; Carpick, R. W.; Assink, R. A.; Thomas, M. L.; Hankins, M. G.; Voigt, J. A.; Sipola, D.; Boer, M. P. d.; Gulley, G. L. *Langmuir* **2000**, *16*, 7742.

(40) Soto-Cantu, E.; Cueto, R.; Koch, J.; Russo, P. S. *Langmuir* **2012**, *28*, 5562.

(41) Nefedov, V. I.; Salyn, Y. V.; Moiseev, II; Sadovskii, A. P.; Berenbljum, A. S.; Knizhnik, A. G.; Mund, S. L. *Inorganica Chimica Acta* **1979**, *35*, L343.

(42) Cai, M. Z.; Xu, Q. H.; Huang, Y. X. *J. Mol. Catal.A-Chem.* **2007**, *271*, 93.

(43) Yang, H.; Han, X.; Li, G.; Ma, Z.; Hao, Y. *J. Phys. Chem. C* **2010**, *114*, 22221.

(44) Wang, L.-C.; Haung, C.-Y.; Chang, C.-Y.; Lin, W.-C.; Chao, K.-J. *Microporous Mesoporous Matter.* **2008**, *110*, 451.

(45) Wali, A.; Muthukumaru Pillai, S.; Kaushik, V. K.; Satish, S. *Appl. Catal., A* **1996**, *135*, 83.

(46) Hoshiya, N.; Isomura, N.; Shimoda, M.; Yoshikawa, H.; Yamashita, Y.; Iizuka, K.; Tsukamoto, S.; Shuto, S.; Arisawa, M. *ChemCatChem* **2009**, *1*, 279.

(47) Richardson, J. M.; Jones, C. W. *J. Catal.* **2007**, *251*, 80.

Chapter 5

XPS and Wagner plots as a tool for characterizing Pd nanoparticles: an extra-atomic relaxation effect study.

5.1 Introduction

Though nanoparticles research is mostly focused on coinage metals, mostly those of gold, interest in studying the properties of other transition metal nanoparticles is also growing. Transition metal nanoparticles are of great interest because of their unique properties unlike their bulk materials and from the discrete atoms. In the second half of the 20th century, use of transition metal nanoparticles in catalysis became popular in reactions such as hydrogenation, hydrosilylation, and hydration of unsaturated substrates and redox reactions including water splitting and photocatalytic hydrogenation.[1] Among the reported reactions, there were some pioneering applications of nanoparticles. For example, in 1940 the F. F. Nord group reported the nitrobenzene reaction[2], while in 1970 the G. Parravano[3] group reported AuNPs catalysts in hydrogen atom transfer between benzene and cyclohexane and oxygen atom transfer between CO and CO_2. Catalysis is considered as the central field of nanoscience and nanotechnology.[4] Research efforts in palladium nanoparticle synthesis have intensified because of the important role played by palladium in catalysis.[5] Due to the high surface area to volume ratio of nanoparticles, the potential use of metal nanostructures including Pd nanoparticles in catalysis has become an important platform of research for the scientific community since the 1990s.[6] Palladium nanoparticles are of great importance in variety of catalytic applications; particularly in hydrogenation[7], selective oxidation of methane to methanol[8] as well as selective oxidation of

alcohols to aldehydes[9], isomerization of allyl alcohol to propanol[10], ketones[11] and esters,[12] and carbon-carbon bond formation.[13] [14] [15] [16] Furthermore, the application of Pd nanoparticles goes beyond catalysis to hydrogen storage and sensing applications.[17] Each of abovementioned applications requires very specific shape, size distribution,[18] as well as specific coating (or stabilizing organic molecules), and understanding of how these parameters influence the electronic state of the metal. Significant advances have been made in the last two decades in the field of nanoparticles. It was reported that catalytic activity and selectivity are largely affected by the size of the particles.[19] [20] El-Sayed reported the shape-dependence of nanocatalysis, synthesizing platinum nanoparticles of tetrahedral and cubic shapes by using the hydrogen reduction procedure and polyacrylate as the stabilizing agent.[21] It was also reported that catalytic activity increases with decreasing the size of the nanoparticles.[22] PVP-capped Pd nanoparticles (3.0-6.6 nm) were reported to be effective catalysts in the Suzuki cross-coupling reaction.[23] Ganesan *et al* reported the monodispersed thioether-stabilized Pd nanoparticles (1.7 nm to 3.5 nm) synthesized by varying reaction temperature, reaction time, solvent, and carbon chain length of the thioether.[24] With the increasing applications of nanoparticles, tunable control of size and dispersion becomes indispensable. Therefore, it is necessary to investigate the physical, chemical and electronic properties of Pd nanoparticles, i.e. precise control of the particle size and their size dependent properties.

The focus of this chapter is the synthesis, stabilization, and characterization of palladium nanoparticles. One of the primary goals is to better understand the change of electronic properties with the size of the nanoparticles. Developing and understanding of the connection amongst the structure, size, electronic properties, and chemistry of nanoparticles is a challenging task. My current study is an effort to better understand the properties of Pd nanoparticles using

advanced surface analytical techniques. Nanoparticles are routinely characterized by transmission electron microscope (TEM), X-ray diffraction (XRD), and ultra-violet visible spectroscopy (UV-Vis) methods. Previous work from our group used XPS and Auger parameter as a tool for characterizing silica supported Pd catalysts.[16,25] It was reported that the shift of binding energy in XPS peaks provide important information regarding oxidation state of Pd complexes as well as formation Pd nanoparticles. In chapter 4, model heterogeneous Pd catalyst has been prepared using functionalized Si wafer as the support. Two types of Pd species were identified in the model catalyst: S-bound Pd(II) complex and Pd nanoparticles. It was found that in used catalyst (used in the Suzuki-Miyaura reaction), the size of the nanoparticles reduced and as a result corresponding XPS peaks shifted to the higher binding energy. This shift is likely due to the extra-atomic relaxation effect. The chapter will serve two purposes: (1) acquiring knowledge of making mono-dispersed Pd nanoparticles with narrow size distribution and (2) supporting the statements made in Ch.4 regarding the binding energy shift of Pd nanoparticles (State 2).

Nanoparticles can be prepared by reducing a molecular precursor such as metal salt with the help of a reducing agent and stabilized by a molecular stabilizer. A typical preparation for Pd is given in the following equations (5-1 and 5-2).

$$PdCl_4^{2-}(aq) + N(C_8H_{17})_4^{+}(org) \longrightarrow N(C_8H_{17})_4^{+}\,PdCl_4^{2-}(org) \qquad 5\text{-}1$$

$$m PdCl_4^{2-}(org) + n(C_{12}H_{25})_2S\,(org) + xme^{-}(aq) \longrightarrow Pd_m[(C_{12}H_{25})_2S]_n\,(org) + 4Cl_m^{-}\,(aq) \qquad 5\text{-}2$$

One of the most widely used method of modern nanoparticles synthesis, inspired by the 150-year old method of Faraday (the formation of AuNPs by reducing tetrachloroaurate $[AuCl_4]$- using phosphorous as the reducing agent)[26] and improved and popularized by Schiffrins group in 1990s[27], involves the reduction of metal precursor such as $HAuCl_4$ or Na_2PdCl_4 by $NaBH_4$ in a two-phase system (organic solvent-water) in presence of a phase transfer reagent, $[N(C_8H_{17})_4]Br$, and followed by addition of a stabilizer (as for example thiol for Au-nanoparticles and for Pd-nanoparticles (4-dimethylamino)pyridine).[5] Metal nanoparticles can also be synthesized by the vaporization of the atomic metal or of metal(0) complex. Another approach to nanoparticles synthesis is known as the polyol method: the thermal decomposition of metallic(0) precursors in the presence of alcohol as the solvent, and stabilizing polymers. There are many articles and reviews describing the various preparation routes for nanoparticles[17,28] and herein I will not cover all aspects in detail. I will focus on rather the preparation of different sizes of nanoparticles and their characterization using mainly XPS and related theories, after a brief survey of the basic features of nanoparticles synthesis.

Reproducibility of nanoparticles with a predetermined size, shape, and composition is an important challenge in the nanoparticles research area. Nanoparticles are thermodynamically unstable with respect to agglomeration; they need to be stabilized kinetically using a protective stabilizer.[17] Nanoparticle stabilization is achieved by the equilibrium of the van der Waals attractive forces and the electrostatic repulsive forces. Stabilization is governed by a number of processes such as electrostatic stabilization, steric stabilization, and electrosteric stabilization. Electrostatic stabilization is by the anions adsorbed on the surface and steric stabilization is governed by the presence of bulky groups. Stabilization also occurs by a combination of these two

methods known as electrosteric stabilization.[29] Figure 5-1 schematically represents the stabilization process by electrostatic and steric mechanism. Electrostatic stabilization consists of adsorption of ions on the metal surface leading to the form an electrical double layer. This double layer makes a Coulombic repulsion force between individual particles, thus preventing agglomeration. Steric stabilization occurs by creating a layer of material (stabilizer) such as polymers or surfactants surrounding the metal cluster, which provide a steric barrier sufficient to prevent close contact of metal particle centers.

(a) (b)

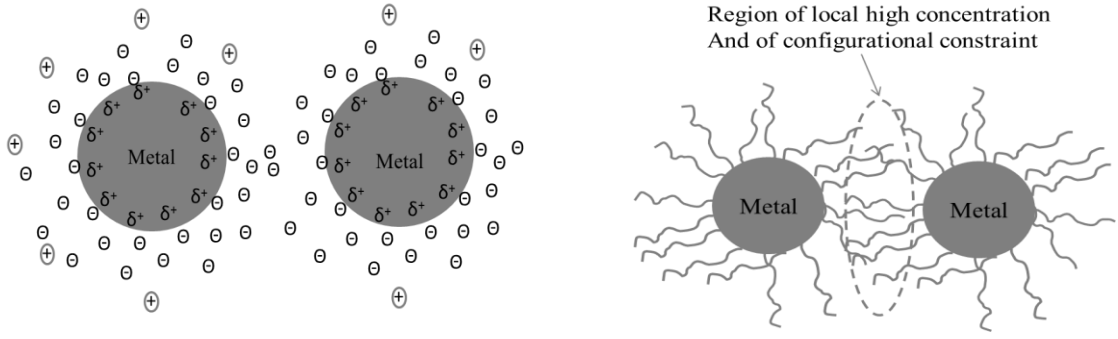

Figure 5-1: Schemtic representation of (a) electrostatic stabilization and (b) steric stabilization of metal colloids. [Figure reproduced from literature.[28b]]

Nanoparticles stabilization is not merely spontaneous. If nanoparticles stabilize by themselves then the size control and the dispersion may become problematic. This can be solved by using extra stabilizing agents or stabilizers. Stabilizers inhibit overgrowth and aggregation of nanoparticles. Stabilizers can also be used to control the structural characteristics of the resulted nanoparticles in a particular manner. The commonly used stabilizers for nanoparticles stabilization are: organic ligands, surfactants, polymers and dendrimers.[17]

Ligands: Organic ligands having a heteroelement with an accessible lone pair are widely used as a stabilizer for palladium nanoparticles.[17] The organic chain of the ligand helps prevent agglomeration and the heteroatom acts to bind the ligand to the surface of the metal. In Pd or Au nanoparticles sulfur containing ligands act as an efficient stabilizer because of their strong interaction with noble and platinum group metals. Brust *et al*. demonstrated the use of thiol as a stabilizer for gold nanoparticles in a two-phase (water-toluene) system using $NaBH_4$ as the reducing agent.[27] Thiolated ligands have also been used by some researchers.[28c]

Polymers: Polymers are widely used as stabilizers for NPs because of their bulk steric framework and ability to bind weakly to the NP surface by the heteroatom, playing the role of ligands.[30] Figure 5-2 presents the chemical structure of two commonly used polymer stabilizers. The most widely used polymer stabilizer is poly(N-vinyl-2-pyrrolidone) (PVP) since it meets both steric and ligand requirements.

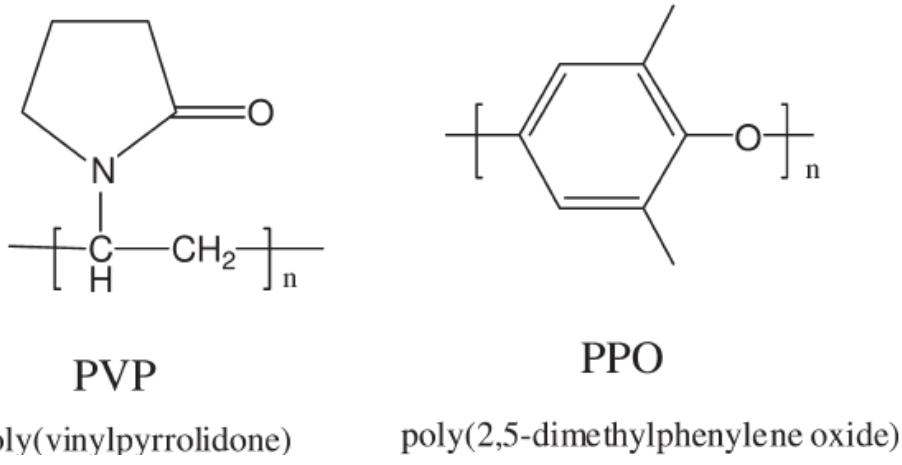

Figure 5-2: Two major polymeric stabilizers.

The synthesis of Pd nanoparticles using different stabilizers are shown in figure 5-3.[17] Sulfur based ligands show strong interaction to the platinum group metals. Common sulfur based ligands include, thiols, thioether, and thioesters. While thiols are the most commonly used ligands, surprisingly there are very few other sulfur-based ligands have been reported in the literature. In our present work, we chose dodecyl sulfide as the stabilizing agent for Pd nanoparticles synthesis. The longer chain length of dodecyl sulfide offers the advantage of giving rise to smaller nanoparticles with narrow size distribution, greater surface accessibility for catalysis application, and post-synthetic modification or tailoring of nanoparticles such as ligand displacement reactions.

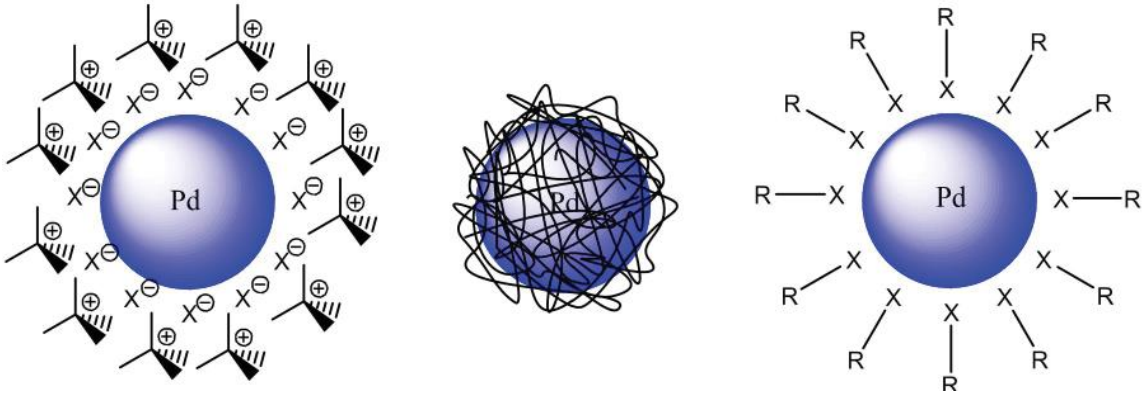

Figure 5-3: Stabilization of Pd nanoparticles using (a) surfactants; (b) polymers; and (c) ligands [Figure reproduced from literature[17]]

Polymers are widely used to stabilize Pd nanoparticles because of their low cost and solubility in a range of solvents. Here, PVP (N-vinyl-2-pyrrolodone) has been used to stabilize Pd nanoparticles. Stabilization by PVP is achieved by ligation of nanocluster surface atoms, at

least in part, and physically incorporating an organic matrix to the nanosystem that prevents agglomeration of nanoparticles by sterically discouraging their direct contact.[29]

The main objective of my present study was to synthesize well dispersed smaller size (1-10 nm) stabilized Pd nanoparticles and detailed characterizations of those to better understand the shift of XPS binding energies due to the initial or final state effect of Pd nanoparticles of different sizes. In this approach, Auger electron spectroscopy, Auger parameters and the Wagner plot concept, together with TEM were used to obtain complementary information.

5.2 Experimental Section

Materials

All chemicals were of analytical grade and used without further purification. $PdCl_2$, dodecyl sulfide, ethylene glycol (EG), and $NaBH_4$ were purchased from Sigma-Aldrich. HCl (1.0 N standardized solution) was purchased from Alfa Aesar,. Polyvinylpyrolidone (PVP) with an average molecular weight of 10000, was also purchased from Sigma-Aldrich.

5.2.1. Palladium Nanoparticles Synthesis

A number of schemes were used to synthesize Pd nanoparticles. Schemes that gave better results are described below:

Scheme 1: This procedure is based on the polyol method.[31] Pd nanoparticles were synthesised by thermal decomposition of Pd-salts. $PdCl_2$ (0.03 g) was dissolved in 15 ml of ethylene glycol (EG). The mixture was stirred for 20 minutes at 90°C. The solution then started turning into black and PVP (0.08g) dissolved in EG (10 ml) was added and again stirred for 2 hours at a high temperature (90°C). The solution became dark black in colour, indicating the formation of Pd nanoparticles.

Scheme 2: Palladium nanoparticles were prepared from $PdCl_2$ by the method demonstrated by Brust *et al.*[27] Here, dodecyl sulfide was used as a stabilizer in the two-phase preparation. $PdCl_2$ (0.24 mM) was mixed with 10 ml diluted HCl (0.5 M). Then 0.30 g tetraoctyl ammonium bromide (TOABr, a phase transfer catalysts) in 20 ml toluene was added to the Pd solution and stirred vigorously for 20 mins. 0.5 mM of dodecyl sulfide mixed in 5 ml toluene was added to the Pd solution and stirred for 20 mins. An aqueous solution of $NaBH_4$ (1 mM, in 5 ml water) was added to the Pd solution to reduce Pd(II) ions to Pd(0). Within a few seconds the color of the solution turned into black confirming the formation of Pd(0). Stirring was continued for 2 hr for allowing forming docecylsulfide stabilized Pd nanoparticles. Figure 5-4 schematically shows the preparation of Pd nanoparticles..

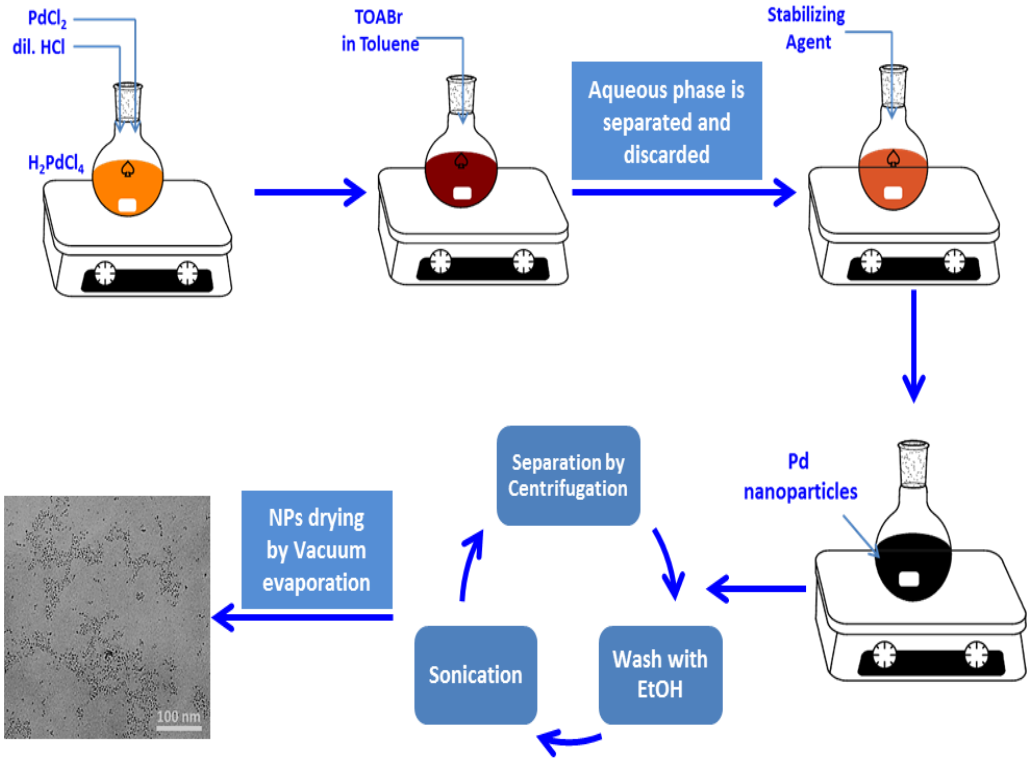

Figure: 5-4: Preparation of the palladium nanoparticles by reduction of $PdCl_2$ salt. A schematic of the various preparation stages discussed in the text.

Scheme 3: In the Pd nanoparticle synthesis protocol, $PdCl_2$ (0.28 mmol) was mixed with 10 ml diluted HCl (0.5 M) solution and stirred vigorously to form H_2PdCl_4, forming an orange color. Then PVP (0.03 g) was dissolved in 10 ml EG and added to the Pd solution with continuous stirring. After 30 minutes, an aqueous solution of $NaBH_4$ was added there slowly, and in a few moments the color of the solution turned black indication the formation of Pd nanoparticles.

In each scheme, Pd nanoprticles were separated by centrifugation. To remove the remaining residues/compounds, nanoparticles were washed (and dispersed by sonication) 3

times with ethanol/toluene and separated by centrifugation each time. Then the resulting Pd nanoparticles were dried using vacuum evaporation techniques.

Sample preparation: For the XPS analysis, samples were prepared by dispersing the nanoparticles into solution using 30 minutes sonication and then drops of the nanoparticle dispersion was placed on aluminum foil cups and dried in ambient condition. For the TEM analysis, one drop of the nanoparticles dispersion was placed on a copper grid and dried in ambient condition before inserting in the instrument chamber.

5.3 Result and Discussion

This section consists of two parts: 1) optimization of Pd nanoparticles synthesis protocol and 2) controlled synthesis of Pd nanoparticles. To optimize the synthesis protocol, different schemes were used. Schemes were developed based on established protocols with some modification where needed. Optimization was achieved by tuning the reaction parameters such as time, temperature, solvents, and amount of reagents.

5.3.1 Optimization of Pd nanoparticles synthesis protocol

Conditions were optimized to acquire mono-dispersed Pd nanoparticles with narrow size distribution. During the nanoparticles synthesis, when reducing agent was added to the $PdCl_2$ and stabilizer containing solution, the color of the solution turned to black from orange-red in a few seconds. This color change phenomenon suggests the reduction of Pd(II) to Pd(0) in the form of Pd nanoparticles.

Freshly prepared palladium nanoparticles samples were characterized by XPS and AES. The position of the Pd $3d_{5/2}$ XPS peak confirms the conversion/reduction of Pd(II) to Pd(0). Figure 5-5 shows the high resolution XPS and Auger peaks of $PdCl_2$ and Pd nanoparticles synthesized using scheme 1. Figure 5-7A and 5-7B represent the Pd 3d XPS peak of $PdCl_2$ powder and palladium nanoparticles, respectively. For $PdCl_2$ powder, Pd 3d XPS peak was found at 338.3 eV binding energy. In the Pd nanoparticles, the Pd 3d peak shifted to 335.0 eV,

confirming the reduction of Pd to Pd(0) oxidation state. No other peaks were present in the 336-338 eV regions confirming that a single state of palladium was present.

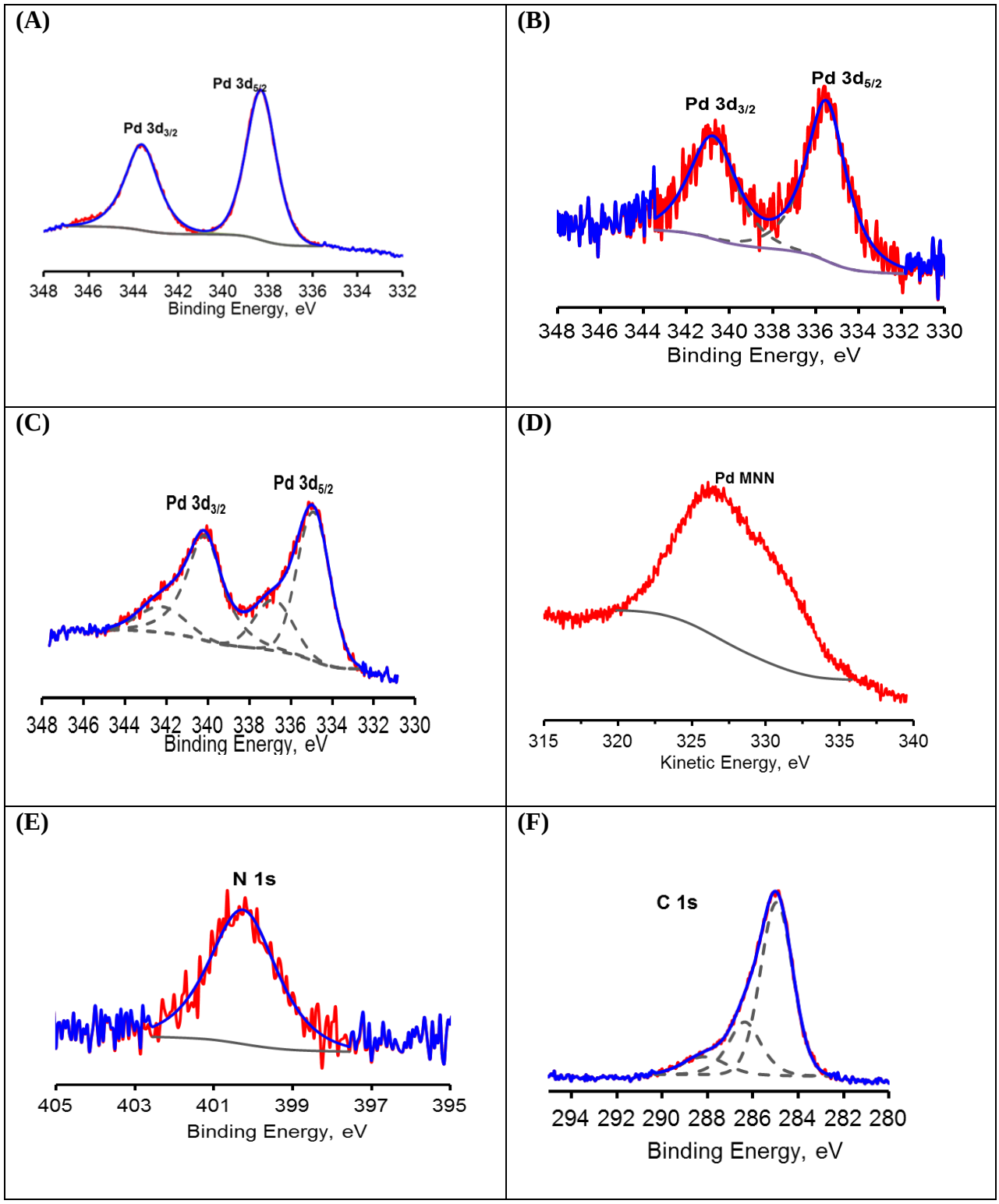

Figure 5-5: Representative XPS spectra of Pd nanoparticles synthesized by scheme 1.

Figure 5-7C is the Pd 3d peak of nanoparticles prepared in a different batch where two peaks of Pd were observed. The higher binding energy peak (at around 337.0 eV) along with the peak at 335.0 eV represents the incomplete conversion. This new peak suggests a number of possibilities: not all Pd(II) ions were reduced to Pd(0); formation of an intermediate state consisting of Pd complexes or oxides; or incomplete washing and separation. Changing the amount of EG and reduction time sometimes reduced the intensity of this intermediate peak; however, reproducibility was challenging using Scheme 1.

The Pd MNN Auger peak was recorded for Pd nanoparticles (Figure 5-7D) and used for determining the Auger parameter. XPS also confirms the presence of stabilizing agent on the nanoparticle surface. The presence of PVP on the nanoparticles surfaces was confirmed from the N 1s and C 1s spectra, as shown in figures 5-7E and 5-7F respectively. The N 1s peak at 400.2eV is consistent with the known spectra of nitrogen within the PVP structure.[32] In the C 1s spectra, three types of carbon: C-C (285.0 eV), C-N (286.5 eV), and C-O (288.5 eV) were recorded that corresponds to the three types of carbon in the PVP structure (figure 5-2).

Pd nanoparticles were analyzed by TEM to measure the size and dispersion of the nanoparticles. Figure 5-6 shows the TEM micrographs of Pd nanoparticles synthesized using scheme 1. It is seen from the figure that the nanoparticles are not well dispersed but rather are agglomerated with a wide size distribution. This suggests that the EG alone may not be an efficient reducing agent, only partially reducing Pd(II) species, and leading to agglomeration and/or uneven size distribution.

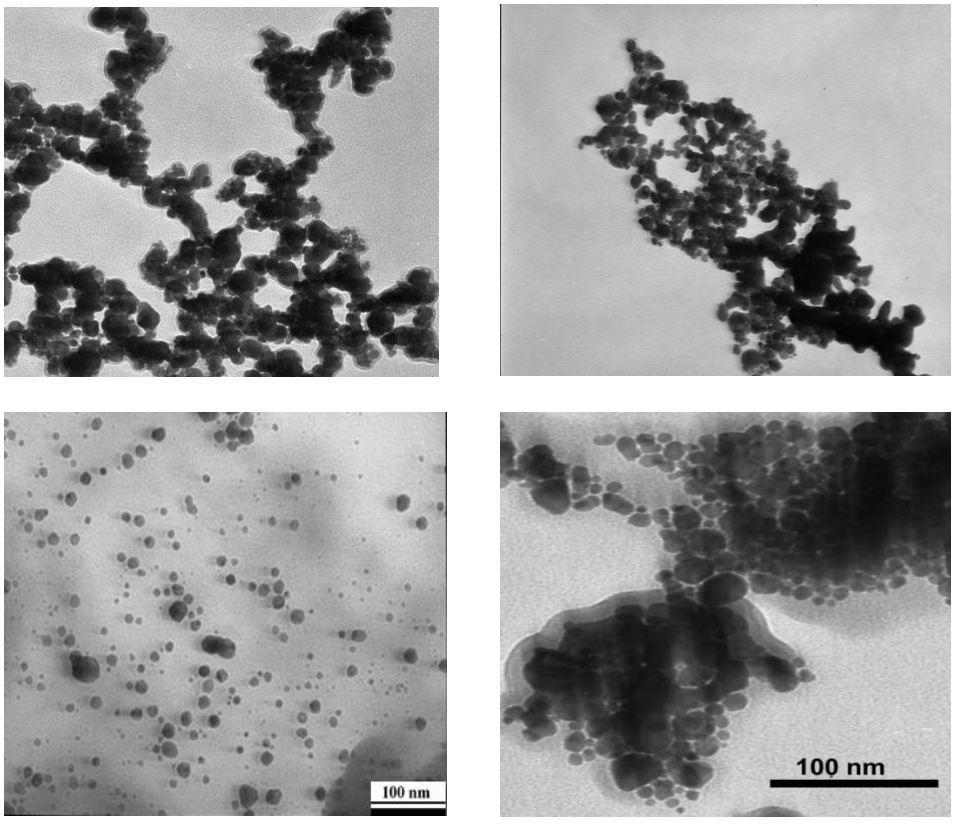

Figure 5-6: TEM micrographs of Pd NPs synthesised using scheme 1.

While scheme 1 was partially successful in synthesizing Pd nanoparticles, schemes 2 and 3 showed much greater reproducibility. Each scheme was repeated to check the reproducibility. Table 5-1 summarizes the XPS and AES binging energies of Pd nanoparticles synthesized using the three different schemes. Pd 3d binding energies of Pd nanoparticles were found in the range of 335.2 to 335.5 eV and corresponding Auger peaks were found in the range of 326.0 eV to 327.0 eV. These Pd 3d binding energies correspond to the Pd metal, in the form of Pd nanoparticles. The N 1s peaks at 400.0 eV and 399.7 eV were found for nanoparticles synthesized in Scheme 1 and 3, respectively, suggesting that the nanoparticles are stabilized by PVP. Similarly, in Scheme 2, S 2p peak was recorded at 163.0 eV corresponds to the sulfur of dodecylsulfide.

Table 5-1: Binding energies of Pd NPs synthesized using different schemes.

Name	**Peak Binding Energy (eV)**				
	Pd $3d_{5/2}$	Pd MNN	C 1s	N 1s	S 2p
PdCl2	338.31	325.14	285		
Scheme 1	335.2	327.0	285, 286.2, 288.6	400.0	
Scheme 2	335.2	326.8	285.0, 286.3		163.0
Scheme 3	335.4	326.0	285, 286.0, 288.8	399.7	

Representative XPS spectra of Pd nanoparticles stabilized by dodecyl sulfide are shown in figure 5-7. It is seen from the figure that Pd is in Pd(0) oxidation state in the form of nanoparticles, and C 1s and S 2p peaks are in the desired binding energy regions. From this it can be assumed that Pd nanoparticles have been successfully synthesized and they are capped by dodecyl sulfide.

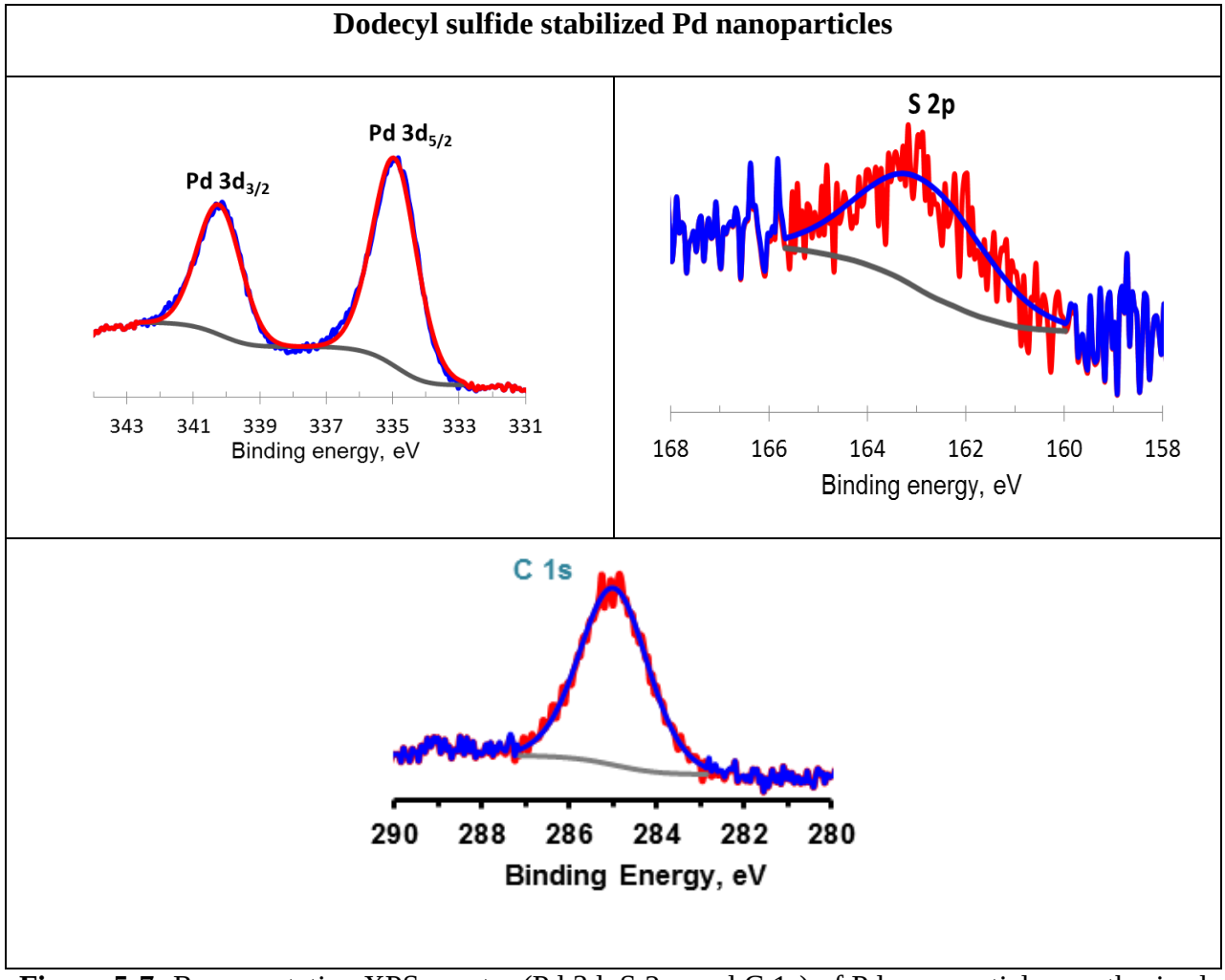

Figure 5-7: Representative XPS spectra (Pd 3d, S 2p, and C 1s) of Pd nanoparticles synthesized by scheme 2.

Formation of nanoparticles was also investigated using TEM. Figure 5-8 is the TEM micrograph of Pd nanoparticles synthesized using Scheme 2. It is seen from the image that nanoparticles are well-dispersed with narrow size distribution, a necessary condition if we are to acquire a correlation to XPS data and form a Wagner plot.

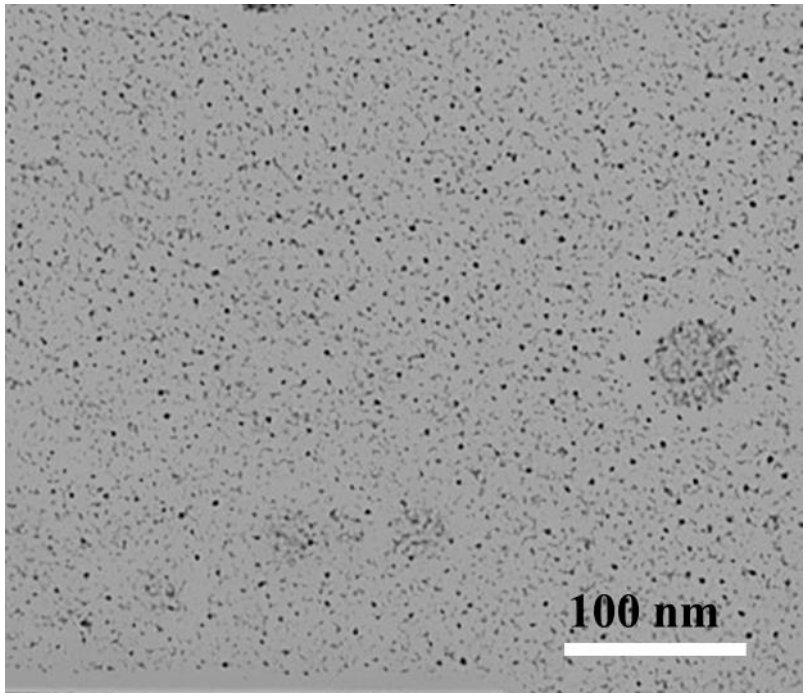

Figure 5-8: TEM image of Pd nanoparticles synthesized using Scheme 2.

Pd nanoparticles synthesized using PVP as the stabilizing agent (Scheme 3) were also characterized in same fashion. Figure 5-9 represents the Pd 3d, N 1s, and C 1s XPS peaks of Pd nanoparticles synthesised using Scheme 3. All these XPS peaks confirm the successful synthesis of PVP stabilized Pd nanoparticles. The N 1s peak and three peaks of C 1s again indicated the presence of PVP on the Pd nanoparticles surface. Furthermore, the TEM image (figure 5-10) confirms the formation of well-dispersed Pd nanoparticles. It is seen from the TEM image that the nanoparticles are in a narrow size distribution.

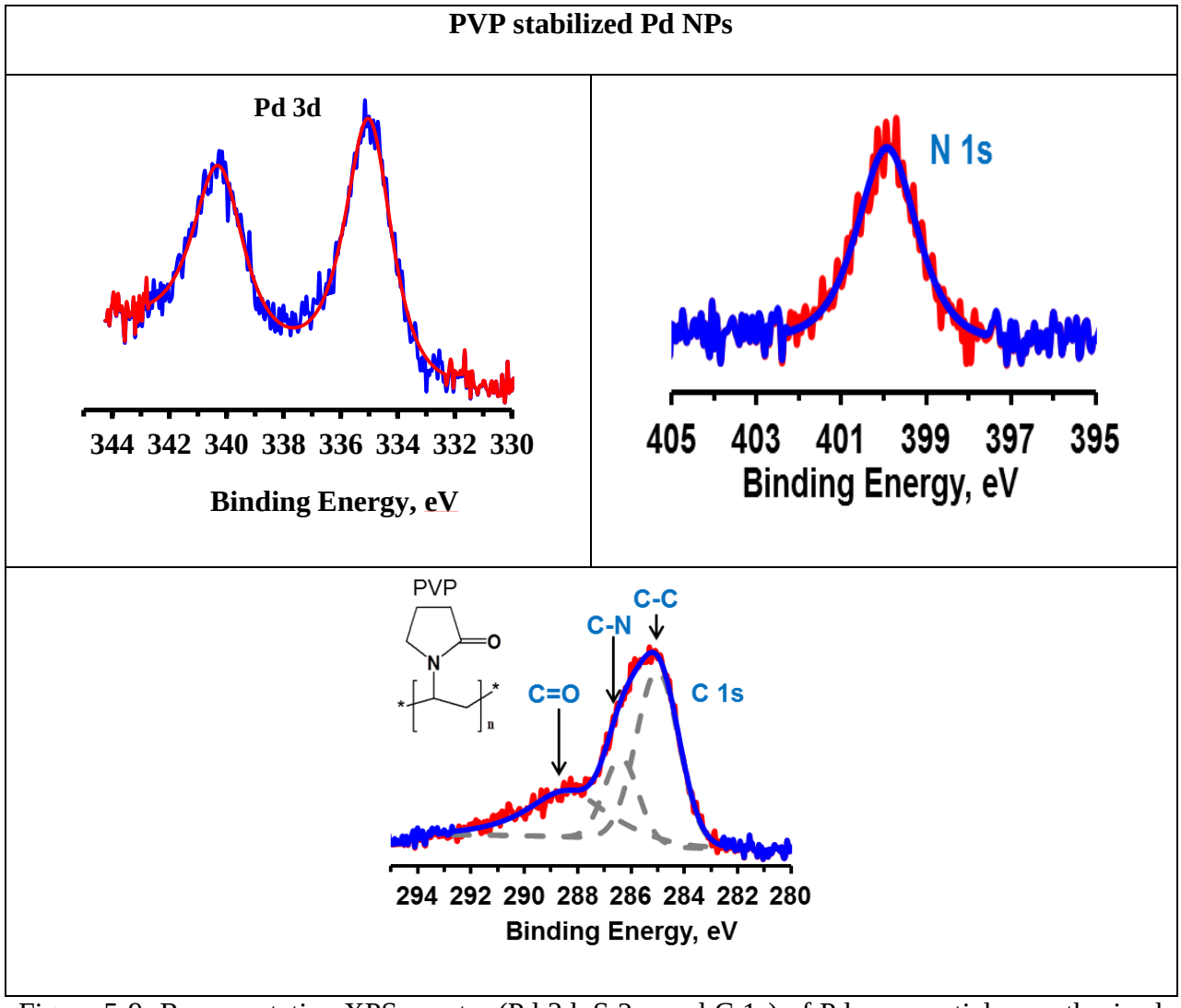

Figure 5-9: Representative XPS spectra (Pd 3d, S 2p, and C 1s) of Pd nanoparticles synthesized by scheme 2.

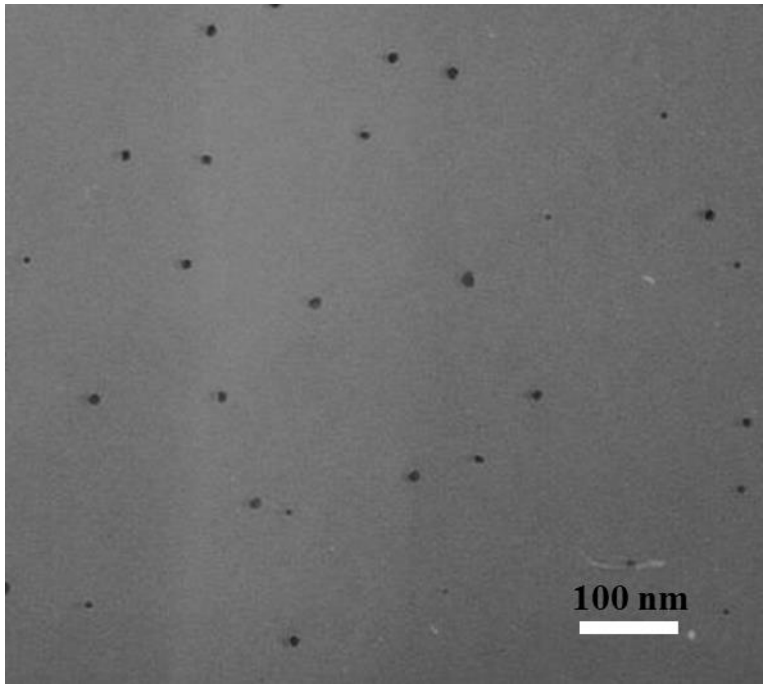

Figure 5-10: TEM image of PVP protected Pd nanoparticles. Image represents the presence of well dispersed Pd nanoparticles with narrow size distribution.

From the above results and discussion, it has been found that Pd nanoparticles can be synthesized using both schemes 2 and 3. The sulfur based stabilizing agent, dodecyl sulfide, and the polymeric stabilizing agent, PVP, both successfully stabilizeed the Pd nanoparticles with well dispersion and narrow size distribution. The following part of the results and discussion concentrates on tailoring the size of the nanoparticles and their characterization using surface analytical techniques.

5.3.2 Controlling nanoparticles size distributions

In this part of the chapter, synthesis of different sizes of Pd nanoparticles and their characterization will be will be discussed. Controlling the size of the nanoparticles can be achieved by varying reaction time[33], and the concentration of the stabilizing agent. The size of Pd nanoparticles has a dramatic influence on the catalytic activity.[34] Our primary goal here was to obtain a range of samples of varying particle size in order to explore the effect of particle size on both the Pd 3d binding energy and Auger parameter. Here, the sizes of the nanoparticles were controlled by varying the concentration of stabilizing agents. Selection of the nanoparticle stabilizing agent is crucial since it provides the first degree of protection of nanoparticles from agglomeration and leaching. In this experiment, we once again used dodecyl sulfide and polyvinylpyrrolidone (PVP). PVP has shown promise in stabilizing larger (2-11 nm) Pd nanoparticles with an evidence of superior size and shape tuning.[35] Pd nanoparticles stabilized by dodecylsulfide or PVP have both been reported to be active in catalytic reactions including the Suzuki reaction.[20,29]

The size of the nanoparticles was tuned by controlling the concentration of stabilizing agent. Table 5-2 summarizes the concentration of dodecyl sulfide and PVP used to synthesis different sizes of Pd nanoparticles. Dodecyl sulfide nanoparticles are named as X, Y, and Z and PVP stabilized nanoparticles are named as A, B, and C. Experiments were performed leaving other parameters including amount of the Pd salt and the reducing agent, and the reaction temperature constant.

Table 5-2: Concentration of stabilizing agents and the sizes of Pd nanoparticles.

Sample name	Stabilizing agent	Amount of stabilizing agent, mM	Nanoparticles Size, nm (Measured by TEM)
X	Dodecyl sulfide	2.0	1.5-2.5
Y		0.5	2.5-4
Z		0.12	4-5.5
A	PVP	0.009	2-4
B		0.003	5.5-7
C		0.001	8-11

Since TEM is the most widely used method of measuring nanoparticles size and dispersion, the Pd nanoparticles synthesized here were investigated using TEM. The TEM micrographs of Pd nanoparticles stabilized by dodecyl sulfide and PVP are shown in Fig 5-11 and 5-12 respectively. Accompanying histograms represent the size distribution of Pd nanoparticles. It is seen from figure 5-11 that nanoparticles were well dispersed with a narrow size distribution. The average particles sizes were found in the ranges of 1.5-3 nm for the sample X (highest concentration of stabilizing agent), 2-4 nm for the sample Y, and 4-5.5 nm for the sample Z (lowest concentration of stabilizing agent). It is important to note that the core size of the nanoparticles increased with decreasing the concentration of stabilizing agent. Furthermore, size distribution is narrow for smaller nanoparticles, suggesting that the lesser amounts of stabilizing agent control the size of the particles less effectively.

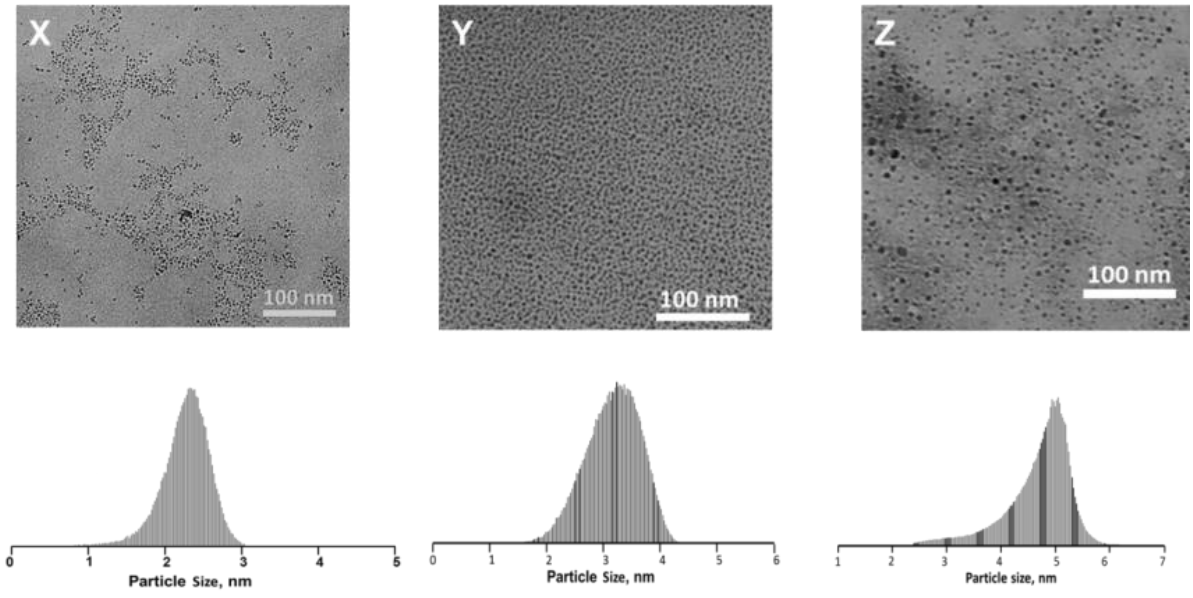

Figure 5-11: TEM images of dodecyl sulfide protected palladium nanoparticles synthesized with different molar concentration of dodecyl sulfide (X) 2.0 mM, (Y) 0.5 mM and (Z) 0.12 mM. The accompanying histograms show the particle size distribution.

For PVP stabilized Pd nanoparticles, in figure 5-12, the sizes of particles were found in the ranges of 1.5-4 nm for sample A (highest concentration of PVP), 5.5-7 nm for sample B, and 8-11 nm for sample C (least concentration of PVP). Like dodecyl sulfide protected Pd nanoparticles, the size of the nanoparticles increases with decreasing stabilizing agent concentration. Both dodecyl sulfide and PVP protected the Pd nanoparticles effectively, preventing agglomeration and allowing an even dispersion on the TEM grid. However, polymer protected NPs result in a somewhat wider size distribution than dodecyl sulfide. This can be attributed to the fact that PVP protects the Pd nanoparticles from agglomeration by forming a protective layer around the nanoparticles; which is basically by physisorption. On the other

hand, dodecyl sulfide forms chemical bond (Pd-S) with the Pd nanoparticles and thus protects from agglomeration.

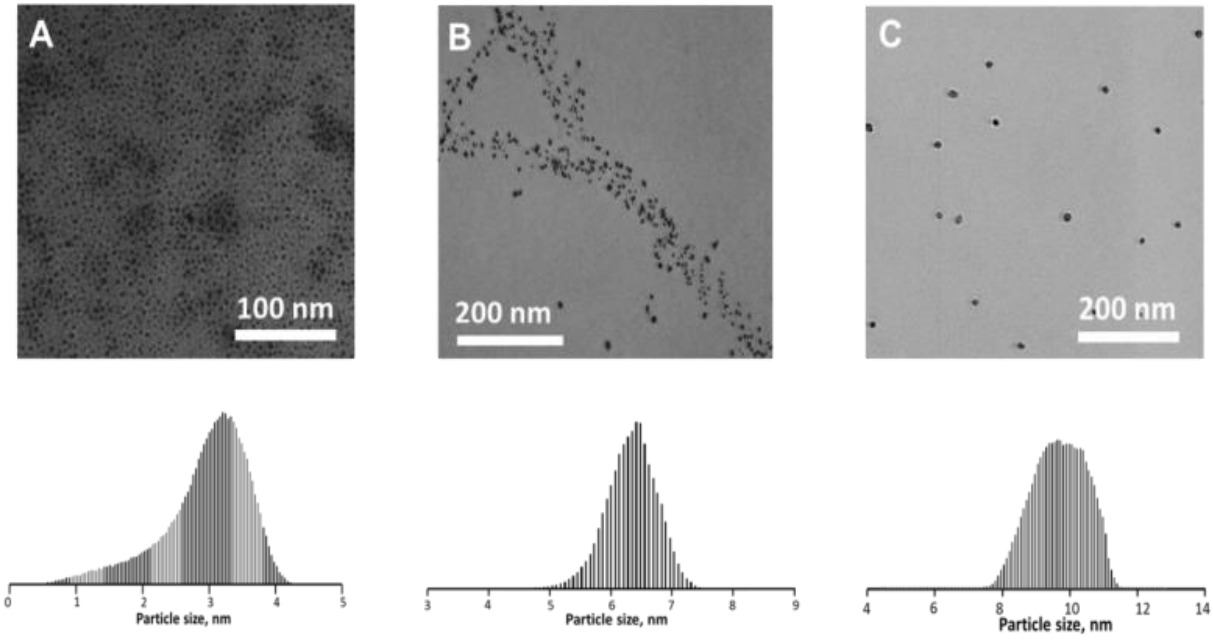

Figure 5-12: TEM images of dodecyl sulfide protected palladium nanoparticles synthesized with different molar concentration of dodecyl sulfide (A) 0.009 mM, (B) 0.003 mM and (C) 0.001 mM. The accompanying histograms show the particle size distribution.

UV-Vis spectroscopy was also used to analyze the Pd nanoparticles. Figure 5-13 shows the UV-visible spectra of aqueous $PdCl_2$ solution and colloidal suspension of Pd-nanoparticles stabilized by dodecyl sulfide and PVP. The reduction of Pd(II) ions in $PdCl_2$ to Pd(0) in Pd-nanoparticles was identified. Here, reference peak of $PdCl_2$ situated at 440 nm and this peak was completely absent in Pd nanoparticles samples. A broad continuous absorption indicating the reduction of Pd(II) ions to Pd nanoparticles. This result is consistent with the XPS data i.e. complete reduction of Pd(II) ions to Pd (0).

(A) (B)

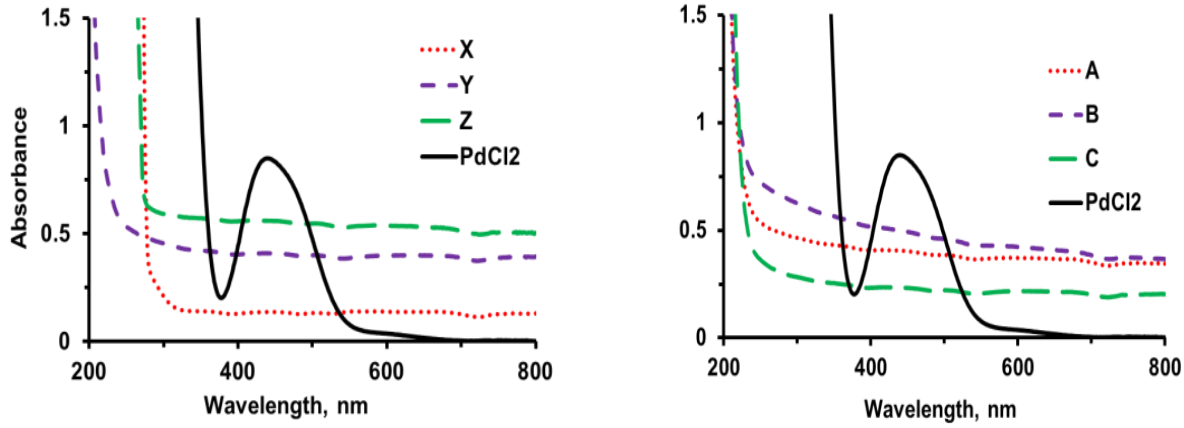

Figure 5-13: UV-visible spectra of Pd-nanoparticles (a) dodecyl sulfide stabilized Pd nanoparticles, (b) PVP stabilized Pd nanoparticles. The preparation scheme for the particles corresponding to spectra labelled A-C and X-Z are indicated in Table 5-2.

Pd nanoparticles were also characterized by XPS and AES. Table 5-3 summarizes the binding energy of Pd 3d peak, the kinetic energy of Pd MNN peak, and calculated Auger parameter of dodecyl sulfide and PVP stabilized Pd nanoparticles. Figure 5-14 and 5-15 represent the Pd 3d XPS spectra of dodecyl sulfide and PVP protected Pd nanoparticles respectively. The Pd $3d_{5/2}$ peaks of dodecyl sulfide stabilized Pd nanoparticles were found in the binding energy range of 335.0 - 335.5 eV and corresponding Auger peaks were in the kinetic energy range of 327.7 – 326.8 eV (Table 5-3). These values are consistent with the formation of Pd nanoparticles in the form of a Pd(0) oxidation state.

Sample X with smaller size nanoparticles gave a peak at 335.5 eV whereas sample Z with biggest nanoparticles showed XPS peak at 335.0 eV. The binding energies shift towards higher values with a decrease in particle size (Table 5-2).

Table 5-3: XPS and Auger data of dodecyl sulfide and PVP stabilized Pd nanoparticles.

Sample name	**Amount of stabilizing agent, mM**	**XPS peak position,(eV) Pd $3d_{5/2}$**	**Auger Peak position,(eV) $M_4N_{45}N_{45}$**	**Auger Parameter, (eV) α'**
X	2.0	335.5	326.8	662.3
Y	0.5	335.4	327.1	662.5
Z	0.12	335.0	327.7	662.7
A	0.009	335.4	326.0	661.4
B	0.003	335.1	326.8	661.9
C	0.001	334.9	327.6	662.5

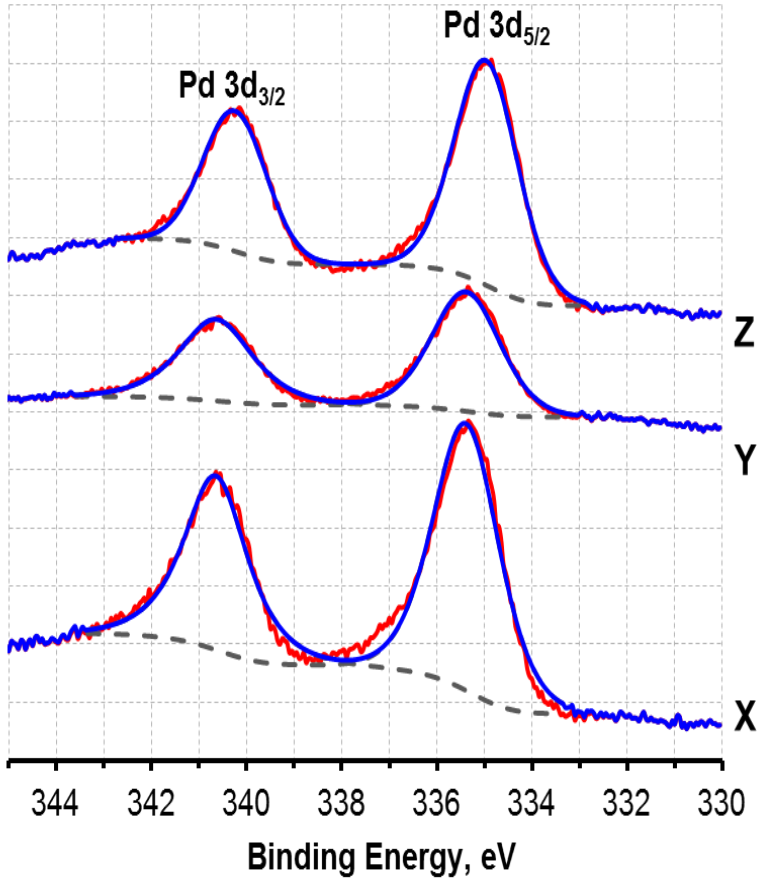

Figure 5-14: Pd 3d XPS spectra of dodecyl sulfide protected palladium nanoparticles synthesized with different molar concentration of dodecyl sulfide (X) 2.0 mM, (Y) 0.5 mM, and (Z) 0.12 mM.

Significantly, the same trend was also observed for PVP protected Pd nanoparticles. In Figure 5-15, it is seen that Pd $3d_{5/2}$ peaks were in the binding energy range of 334.9 – 335.4 eV and corresponding Auger kinetic energies were in the range of 327.6 – 326.0 eV (Table 5-3).

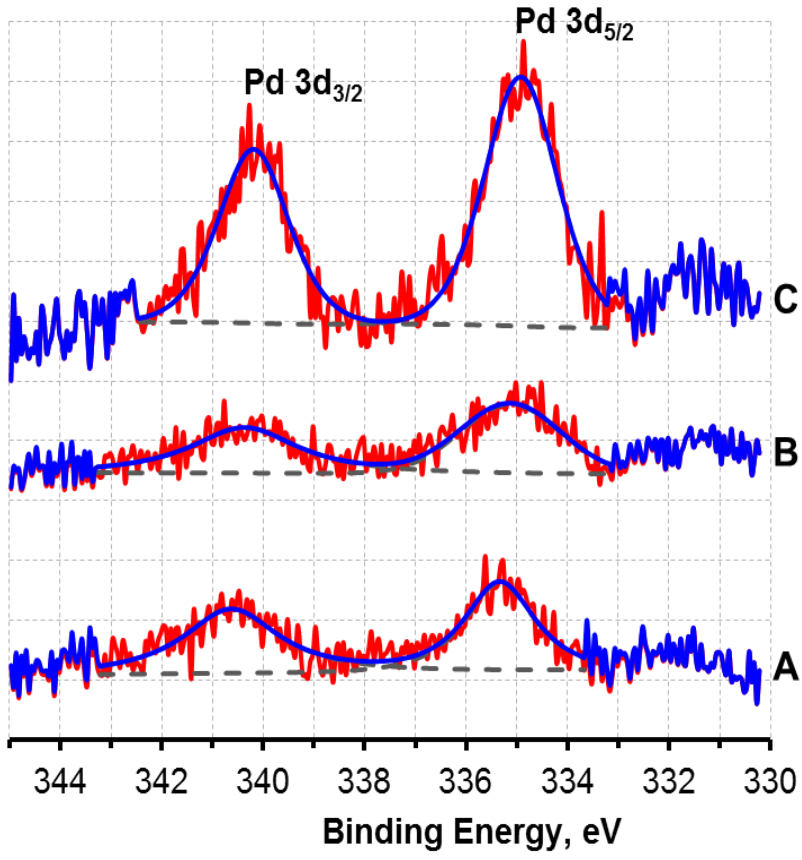

Figure 5-15: Pd 3d XPS spectra of PVP protected palladium nanoparticles synthesized with different molar concentrations of PVP (A) 0.009 mM, (B) 0.003 mM and (C) 0.001 mM.

The XPS peak positions (BE) of different Pd nanoparticles with their sizes are plotted in a two-dimensional graph and presented in figure 5-16. It is seen from the figure that smaller nanoparticles give peak at higher binding energy and larger nanoparticles give peak at lower binding energy. This is true for both types of Pd nanoparticles prepared here.

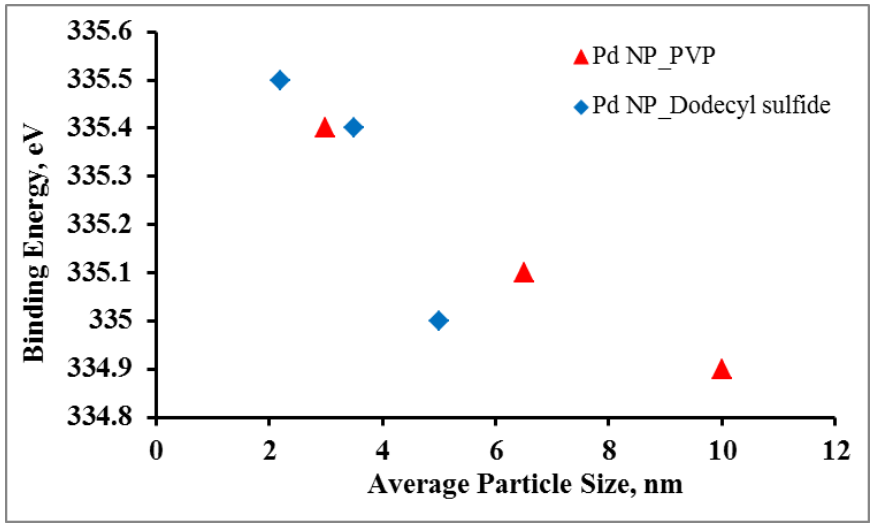

Figure 5-16: Change of binding energies of Pd nanoparticles with sizes.

While there are a number of reports of XPS data in the literature of Pd nanoparticle characterization, there are no reports AES and Auger parameter as a characterization tool for nanoparticles known to the author, other than those previously reported by our research group.[16,25] Auger parameters were calculated using the XPS binding energy (BE) of (Pd 3d) and the Auger kinetic energy (KE) of (Pd MNN), also reported in Tables 5-3. The Auger parameter offers the advantage of charge correction and also provides a better indication of charge shift than XPS alone. To gain better insight into the Pd nanoparticles electronic properties, the XPS, AES, and Auger parameter data were used in the Wagner plot (Figure 5-17). In figure 5-17, data points A, B, C, X, Y, Z, and $PdCl_2$ were taken using the data reported here. It is seen from the figure that both types of nanoparticles show same trend i.e. nanoparticles shifted to the lower binding energy as the sizes increases.

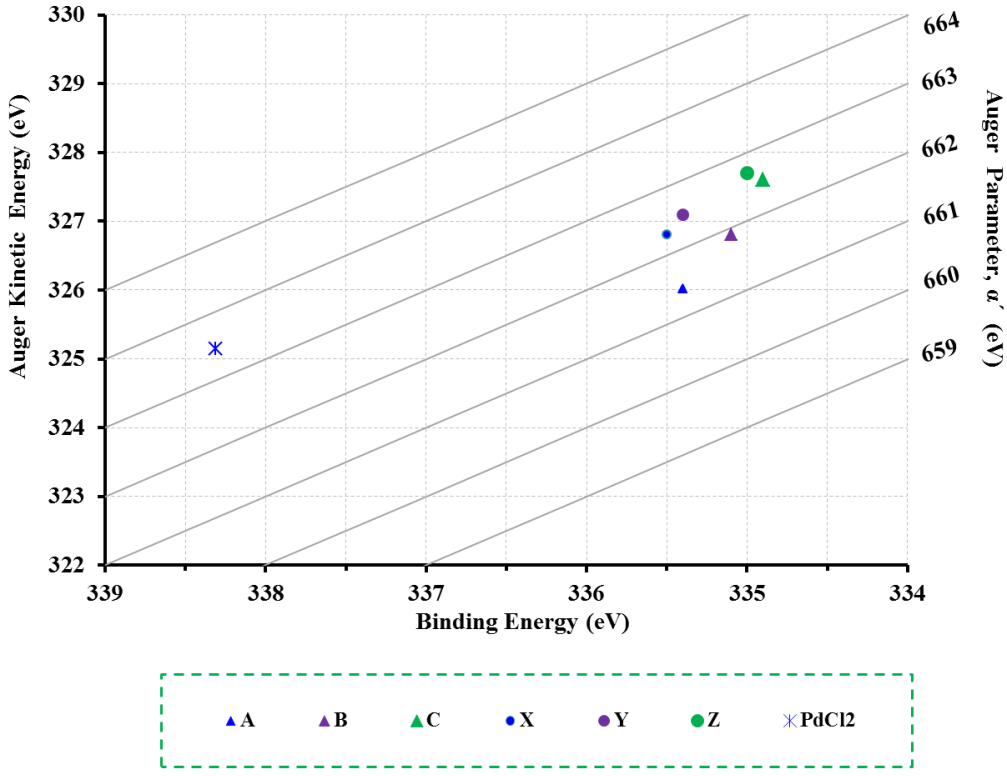

Figure 5-17: Wagner chemical state plot for Pd $3d_{5/2}$ XPS and Pd MNN Auger electron spectroscopy data. Triangle symbols represent data of PVP stabilized nanoparticles of different sizes and circle symbols represent data of dodecyl sulfide stabilized nanoparticles of varying sizes.

These shifts of binding energies can be explained further by comparing the Wagner plot data from Ch. 4. Figure 5-18 is the Wagner plot made combining the data from Ch. 4 with the current data. In Ch. 4, the Pd 3d shifts of SBA-15-SH-Pd catalysts were discussed. It was conjectured that small Pd nanoparticles were formed following the Suzuki reaction, resulting in a shift of binding energy to lower values. In that case, model Pd catalysts (Si wafer-supported thiol Pd) were also described in chapter 4. The shift of BE of Pd nanoparticles to higher BE following

reaction indicated a loss of Pd due to leaching, resulting less extra atomic relaxation. As a result the Pd 3d XPS peak was observed at higher BE. The positions corresponding to PdO and PdS species in the Wagner plot of Figure 5-18 are far from Pd nanoparticle's region. Therefore, there is no evidence of PdO or PdS formation during the synthesis of Pd nanoparticles.

Therefore, these shift of binding energies of nanoparticles can be explained as the fact that the bigger nanoparticles having higher electron density/ more polarizable electrons, tends to move towards the core-hole and stabilize it more effectively than the smaller nanoaprticles with less dense electron density/ less polarizable electrons. So, even though the initial state effect or oxidation number of all nanoparticles are constant, Pd(0), depending on the size of the nanoparticles, extra-atomic relaxation energies varies and appeared in different positions in the Wagner plot (shifts of binding energy depends on both initial state effect and final state effect, see equation 2-8). It was reported that the Pd-Pd interatomic distance expands with decrease in particle size.[33] So, smaller Pd nanoparticles having higher Pd-Pd interatomic distance will exerts less polarization effect than bigger particles having small Pd-Pd interatomic distance. As a result, bigger particles experience more extra-atomic relaxation that reduces the binding energy in XPS.

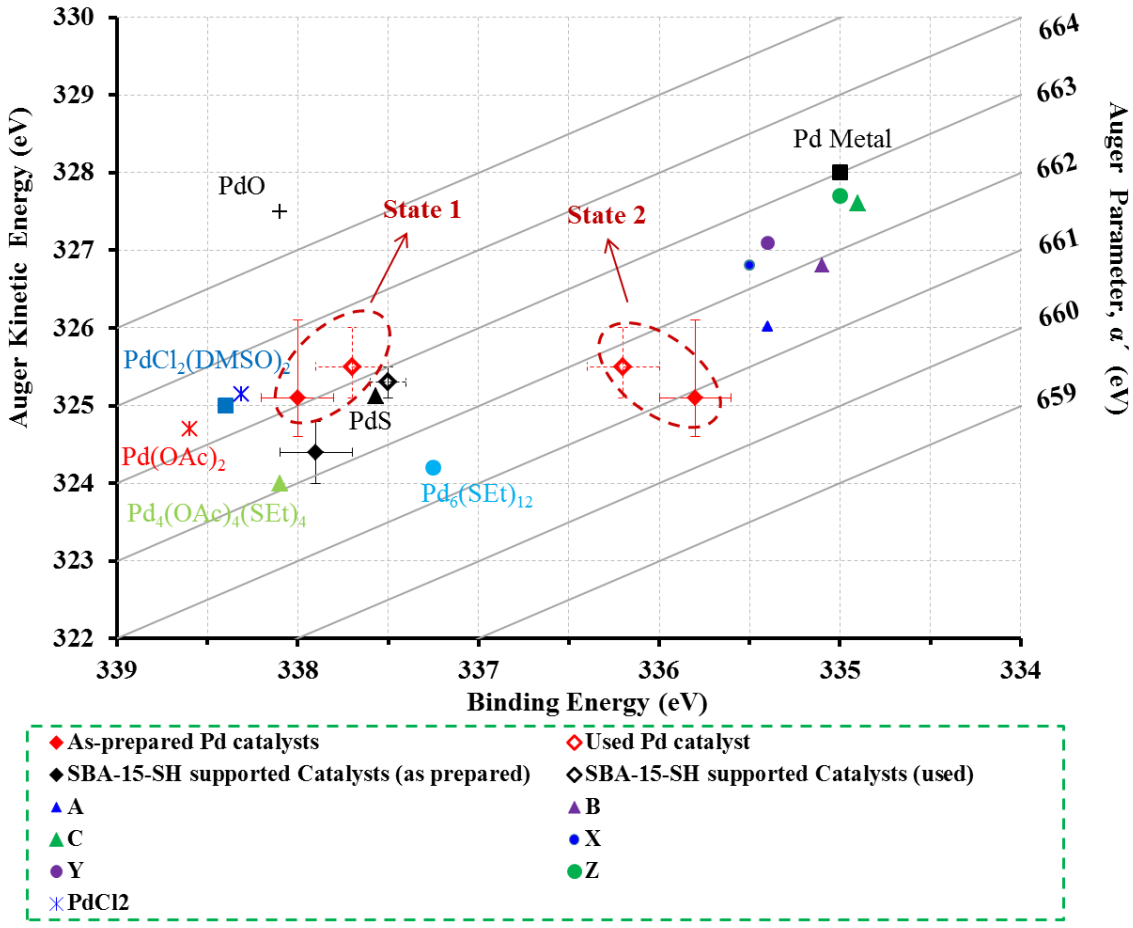

Figure 5-18: Wagner chemical state plot for Pd $3d_{5/2}$ XPS and Pd MNN Auger electron spectroscopy data. All symbols represent data reported here except the symbols representing $PdCl_2$ and Pd nanoparticles, data reported previously in Ch. 4.

The polarization effect is more prominent in the case of PVP protected nanoparticles than that of dodecyl sulfide protected Pd nanoparticles. This can be explained by considering the effect of the extra-atomic relaxation term in Equation [2-8]. The $\Delta\varepsilon$ term should be similar for both cases, as this is dependent only on oxidation state. However, the shift of Auger parameter is higher for PVP protected nanoparticles (ΔBE_{PVP} = 1.1 eV) than that of dodecyl sulfide

nanoparticles ($\Delta BE_{R\text{-}S\text{-}R}$ = 0.4 eV). The corresponding calculated extra-atomic relaxation energies are $\Delta R_{ea(pvp)}$ = 0.55 eV and $\Delta R_{ea(R\text{-}S\text{-}R)}$ = 0.2 eV. Again, difference between smallest and biggest particles is 4.0 nm for dodecyl sulfide protected nanoaprticles ($\Delta Size_{R\text{-}S\text{-}R}$ = 4.0 nm) and it is 9.0 nm for PVP protected nanoparticles ($\Delta Size_{PVP}$= 9.0 nm). These data explain the fact of increased polarizability for PVP protected nanoparticles. Here, dodecyl sulfide protected and PVP protected Pd nanoparticles do not fall on the same trend-line. There could be many possibilities such as two different stabilizing agents likely form different bonding with the Pd nanoparticles surface to prevent agglomeration, so the surrounding environments of the core holes were different, and the concentrations of stabilizing agents were also not identical.

Comparing the Wagner plots and TEM images (Figure 5-11 and 5-12) it can be summarized that changing the concentration of stabilizing agent does control over the size of the Pd nanoparticles; different sizes of nanoparticles do generate different polarizing effect surrounding the core-hole results different extra-atomic relaxation effect, and extra-atomic relaxation effect does control over shift of binding energy. Finally, it is clear that while XPS is very important tool for characterizing nanoparticles, a consideration of binding energy alone is insufficient to determine the true electronic state of the metal species.

5.4 Conclusion

Pd nanoparticles have been synthesized successfully using three different schemes. In the Scheme 1 EG acted as both solvent and reducing agent. XPS and TEM results show that EG was not able to completely reduce Pd(II) ions to Pd(0). Both the Scheme 2 and 3 were able to successfully synthesize Pd nanoparticles. It has been found from this study that XPS and related theories can be used as a major tool for characterizing nanoparticles which will also enable us to better understand about the surface functionalities of the nanoparticles. Efficiency of Pd nanoparticles in catalysis and other applications largely depends on the size of the nanoparticles and properties of surface functionalities of nanoparticles. TEM micrographs and corresponding histograms gave information about the size of the nanoparticles and their dispersion. The XPS results tells us the formation of Pd nanoparticles by looking the position of peaks and also able to identify the stabilizing agents; here dodecyl sulfide and PVP were identified by observing the S 2p, N 1s, and C 1s peaks. The Wagner plot provided information and helped better understand the shift of binding energies of different sizes of Pd nanoparticles and their relationships with polarizability of the surrounding medium by comparing with other reference species. Finally, it can be summarized that the shift of binding energy is directly related to the final state effect (extra atomic relaxation effect) i.e. increasing particles size experiencing higher screening/ polarization of electron from their surroundings, resulting decreasing of binding energy.

5.5 References

(1) *Nanoparticles and catalysis*; Astruc, D., Ed.; Wiley-VCH: Weinheim, 2008.

(2) (a) Rapino, L. D.; Nord, F. F. *J. Am. Chem. Soc.* **1941**, *63*, 2745(b) Kavanagh, K. E.; Nord, F. F. *J. Am. Chem. Soc.* **1943**, *65*, 2121.

(3) Cha, D. Y.; Parravano, G. *J. Catal* **1970**, *18*, 320.

(4) Grunes, J.; Zhu, A.; Somorjai, G. A. *Chem. Commun.* **2003**, 2257.

(5) Didier Astruc; Feng Lu; Aranzaes, J. R. *Angew. Chem. Int. Ed.* **2005**, *44*, 7852.

(6) Semagina, N.; Kiwi-Minsker, L. *Catal. Rev. Sci. Eng.* **2009**, *51*, 147.

(7) Rahi, R.; Fang, M. F.; Ahmed, A.; Sanchez-Delgado, R. A. *Dalton Trans.* **2012**, *41*, 14490.

(8) Ab Rahim, M.; Forde, M. M.; Hammond, C.; Jenkins, R. L.; Dimitratos, N.; Lopez-Sanchez, J. A.; Carley, A. F.; Taylor, S. H.; Willock, D. J.; Hutchings, G. J. *Topics in Catalysis* **2013**, *56*, 1843.

(9) Enache, D. I.; Edwards, J. K.; Landon, P.; Solsona-Espriu, B.; Carley, A. F.; Herzing, A. A.; Watanabe, M.; Kiely, C. J.; Knight, D. W.; Hutchings, G. J. *Science* **2006**, *311*, 362.

(10) Sadeghmoghaddam, E.; Lam, C.; Choi, D.; Shon, Y.-S. *J. Mater. Chem.* **2011**, *21*, 307.

(11) Mifsud, M.; Parkhomenko, K. V.; Arends, I.; Sheldon, R. A. *Tetrahedron* **2010**, *66*, 1040.

(12) Wojcieszak, R.; Ghazzal, M. N.; Gaigneaux, E. M.; Ruiz, P. *Catal. Sci. Tech.* **2014**, *4*, 738.

(13) Astruc, D. *Inorg. Chem.* **2007**, *46*, 1884.

(14) Perez-Lorenzo, M. *J. Phys. Chem. Lett.* **2012**, *3*, 167.

(15) Miyaura, N.; Yamada, K.; Suzuki, A. *Tetrahedron Lett.* **1979**, *20*, 3437.

(16) Hanif, M. A.; Ebralidze, II; Horton, J. H. *Appl. Surf. Sci.* **2013**, *280*, 836.

(17) Cookson, J. *Platinum Met. Rev.* **2012**, *56*, 83.

(18) Boutonnet, M.; Logdberg, S.; Svensson, E. E. *Current Opinion in Colloid & Interface Science* **2008**, *13*, 270.

(19) Chen, S.; Huang, K.; Stearns, J. A. *Chem. Mater.* **2000**, *12*, 540.

(20) Narayanan, R.; El-Sayed, M. A. *J. Am. Chem. Soc.* **2003**, *125*, 8340.

(21) Ahmadi, T. S.; Wang, Z. L.; Green, T. C.; Henglein, A.; ElSayed, M. A. *Science* **1996**, *272*, 1924.

(22) Li, Y.; Boone, E.; El-Sayed, M. A. *Langmuir* **2002**, *18*, 4921.

(23) Li, Y.; Hong, X. M.; Collard, D. M.; El-Sayed, M. A. *Org. Lett.* **2000**, *2*, 2385.

(24) Ganesan, M.; Freemantle, R. G.; Obare, S. O. *Chem. Mater.* **2007**, *19*, 3464.

(25) McEleney, K.; Crudden, C. M.; Horton, J. H. *J. Phys. Chem. C* **2009**, *113*, 1901.

(26) (a) Faraday, M. *Philos. Trans. R. Soc.* **1857**, *147*, 145(b) Daniel, M. C.; Astruc, D. *Chem. Rev.* **2004**, *104*, 293.

(27) Brust, M.; Walker, M.; Bethell, D.; Schiffrin, D. J.; Whyman, R. *J. Chem. Soc. Chem. Commun.* **1994**, 801.

(28) (a) Ozkar, S.; Finke, R. G. *J. Am. Chem. Soc.* **2002**, *124*, 5796; (b) Aiken, J. D.; Finke, R. G. *J. Mol. Catal. A Chem.* **1999**, *145*, 1; (c) Chen, L. J.; Wan, C. C.; Wang, Y. Y. *J. Colloid Interface Sci.* **2006**, *297*, 143.

(29) Ott, L. S.; Finke, R. G. *Coord. Chem. Rev.* **2007**, *251*, 1075.

(30) *Fine Particles Sciences and Technology - From Micro-toNew Particles*; Toshima, N., Ed.; Dordrecht: Kluwer, 1996.

(31) Park, B. K.; Jeong, S.; Kim, D.; Moon, J.; Lim, S.; Kim, J. S. *J. Colloid Interface Sci.* **2007**, *311*, 417.

(32) Huang, H. H.; Ni, X. P.; Loy, G. L.; Chew, C. H.; Tan, K. L.; Loh, F. C.; Deng, J. F.; Xu, G. Q. *Langmuir* **1996**, *12*, 909.

(33) Shen, C. M.; Su, Y. K.; Yang, H. T.; Yang, T. Z.; Gao, H. J. *Chem. Phys. Lett.* **2003**, *373*, 39.

(34) Narayanan, R.; El-Sayed, M. A. *Topics in Catalysis* **2008**, *47*, 15.

(35) Cheong, S. S.; Watt, J. D.; Tilley, R. D. *Nanoscale* **2010**, *2*, 2045.

Chapter 6

Substitution of the stabilizing agents of Pd nanoparticles with N-heterocyclic carbene (NHC).

6.1 Introduction

The oldest and best-studied known nanomaterial is gold nanoparticles, mostly prepared by borohydride reduction in the presence of thiol capping agent in an organic solvent using a two-phase liquid system.[1] The application of nanoparticles has become increasingly important in medicine, material chemistry, and catalysis. [2] Properties of nanoparticles can be manipulated by changing the structure of the metal core itself as well as the stabilizing agents. The nanoparticles' growth dynamics can be controlled by passivation of surfactant ligands to limit the growth of the metal core.[3] Therefore, the choice of capping agent is crucial in tuning the nanoparticles' structure and properties. Recently, N-heterocyclic carbene (NHC)-derived self-assembled ultra-stable monolayers on gold surfaces have been reported by our group.[4] This work has demonstrated the strength of the Au-C bond by showing the high thermal, hydrolytic, chemical and oxidative stability which makes NHCs as exceptionally valuable alternatives to sulfur-based ligand in this role. It was reported that like thiol-based SAMs, surfaces of NHC-based SAMs can be chemically modified to alter surface properties.

NHCs have become an important donor ligands in transition metal-mediated catalysis in C-H activation, and C-C, C-H, C-N and C-O bond formation since its isolation by Arduengo *et al* in 1991.[5] NHCs are relatively stable and can be stored "on the shelf" for an extended period of time. Furthermore, NHCs with different functionalities can be prepared simply from

imidazolium precursors, which are stable in air at room temperature for indefinite time period. NHCs form strong σ-bonds to metals through the carbene lone pair. Transition metal nanoparticles protected by metal-carbon bonds have been reported. For example, synthesis of ruthenium nanoparticles stabilized by virtue of the carbene fragments formed by the reduction of diazo derivatives, gold and platinum nanoparticles stabilize by using diazonium derivatives as precursor.[6]

Palladium nanoparticles have the potential to be used as catalytic materials as well as some other applications such as hydrogen storage and sensing.[7] Therefore, research interest in the synthesis of Pd nanoparticles and their properties studies is growing. Nanoparticles properties can be tuned by changing the surface functionalities. Generally Pd nanoparticles are prepared using polymeric or sulfur based ligands.[7] Little attention has been paid to preparing Pd nanoparticles that are stabilized by palladium-carbon covalent bonds. NHCs have been shown to be versatile and tunable ligands in Au and Pd catalysis that can alter a mechanistic pathway or increase the selectivity of the electrophilic metal atom via simple modifications to substituents.[8] The binding energy of a Pd-S bond is 380 kJ mol^{-1} whereas the Pd-C single bond energy is 436 kJ mol^{-1}.[9] Therefore, fundamentally it will be of great interest to examine the ligand exchange or substitution of capping agent dodecyl sulfide by NHCs. Since this worked well with Au^4 this effort has been made to understand how this work may for Pd. This is the primary motivation of the work described here. Therefore, if NHC-protected Pd nanoparticles can be prepared, it is expected that that it would possess similar catalytic properties. Chechik *et al* prepared NHC-protected Pd nanoparticles.[10] They treated the trioctylphosphine-protected Pd nanoparticles with carbene, Bis-*tert*-butylimidazol-2-ylidene. However, stability of the nanoparticles was a

problem. Recently, the first example of NHC stabilized Pd nanoparticles with long term stability was reported.[11] These nanoparticles were synthesized by a ligand exchanged protocol using long chained NHCs.

It was reported that NHC-protected Au nanoparticles have limited stability in solution and form an irreversible aggregation of nanoparticles which leads to the formation of NHC-metal complexes.[10] The NHC-protected Pd nanoparticles are considered to be a potential candidate in catalysis and the protocol of their preparation is not well established yet. Efforts have been made here to better understand the preparation of NHC-protected Pd nanoparticles and their surface properties. Due to its sensitivity to air and water, NHCs are unlikely to withstand the reducing conditions required for nanoparticles synthesis. Hence, NHCs will be incorporated into the Pd nanoparticles shell by ligand exchange, i.e. by substituting the ligands protecting the nanoparticles. In this case, NHCs and/or NHC-precursors will be used because the later having enhanced stability under ambient conditions. Primarily, Pd nanoparticles will be synthesised using dodecyl sulfide as a stabilizing agent. The longer chain length of dodecyl sulfide offers the advantage of giving rise to smaller nanoparticles with narrow size distribution, greater surface accessibility for catalysis application, and post-synthetic modification or tailoring of nanoparticles, such as ligand displacement reactions.

6.2 Experimental Section

Materials

All chemicals were of analytical grade and used without further purification. $PdCl_2$, tetraoctyl ammonium bromide, dodecyl sulfide, and $NaBH_4$ were purchased from Sigma-Aldrich. HCl from Alfa Aesar, 1.0 N standardized solution.

Methods

6.2.1 Pd nanoparticles synthesis: Pd nanoparticles were prepared following the procedure (scheme 2) described in chapter 5.

6.2.2 Functionalization of dodecylsulfide stabilized Pd nanoparticles by NHCs

The resulting dodecyl sulfide stabilized Pd nanoparticles were treated with a carbene (IPrBenz: 1,3-dihydro-1,3-bisisopropylbenzimidazol**)** solution. 6 mg of the dodecyl-stabilized Pd nanoparticles were dispersed in 2 ml toluene by sonication for 5 minutes. A 10 mM solution of NHC (IPrBenz : 1,3-dihydro-1,3-bisisopropylbenzimidazol**)** was prepared in 2 ml isopropanol. 2 ml of the Pd nanoparticle dispersion and 2 ml of the NHC solution were then mixed together. The reaction was performed at room temperature for 24 hours with vigorous stirring. Following reaction, nanoparticles were separated by centrifugation. Then the nanoparticles were washed in toluene by sonication and separated by centrifugation for three times to remove loosely bound or mobile reagents.

6.3 Result and Discussion

The ability of NHCs to substitute a stable capping agent from the Pd nanoparticles surface were tested by treating the dodecyl sulfide protected Pd nanoparticles with representative NHCs. The following (figure 6-1) NHC (1) and its precursors (2-4): IMes **(***1*, 1,3-dihydro-1,3-bis(2,4,6-trimethylphenyl)imidazole-2-ylidene**)**, IPrBenz **(***2*, 1,3-dihydro-1,3-bisisopropylbenzimidazol-3-ium hydrogen carbonate**)**, IPrBenzCF3 **(***3*, 1,3-di(propan-2-yl)-5-(trifluoromethyl)-1*H*-benzimidazol-3-ium hydrogen carbonate**)**, and IPrBenzBr **(***4*, 5-bromo-1,3-di(propan-2-yl)-1*H*-benzimidazol-3-ium hydrogen carbonate**)** were all found to react with the surfaces of Pd nanoparticles.

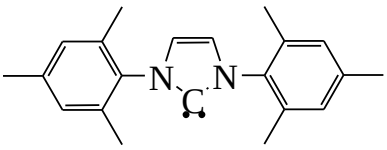

1

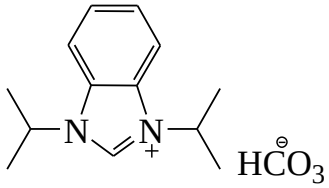

2

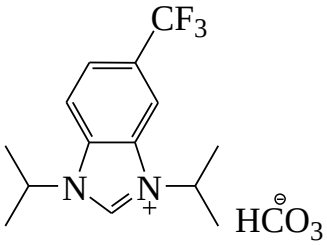

3

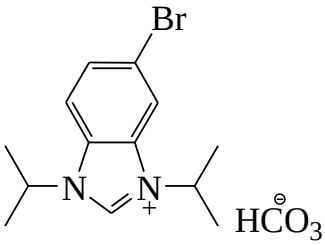

4

Figure 6-1: Representative N-heterocyclic carbene (1) and carbene precursors (2-4) used to functionalize Pd nanoparticles.

The synthetic process of substituting dodecyl sulfide from the Pd nanoparticles surface by N-heterocyclic carbene has been schematically shown in figure 6-2. There could be a number of

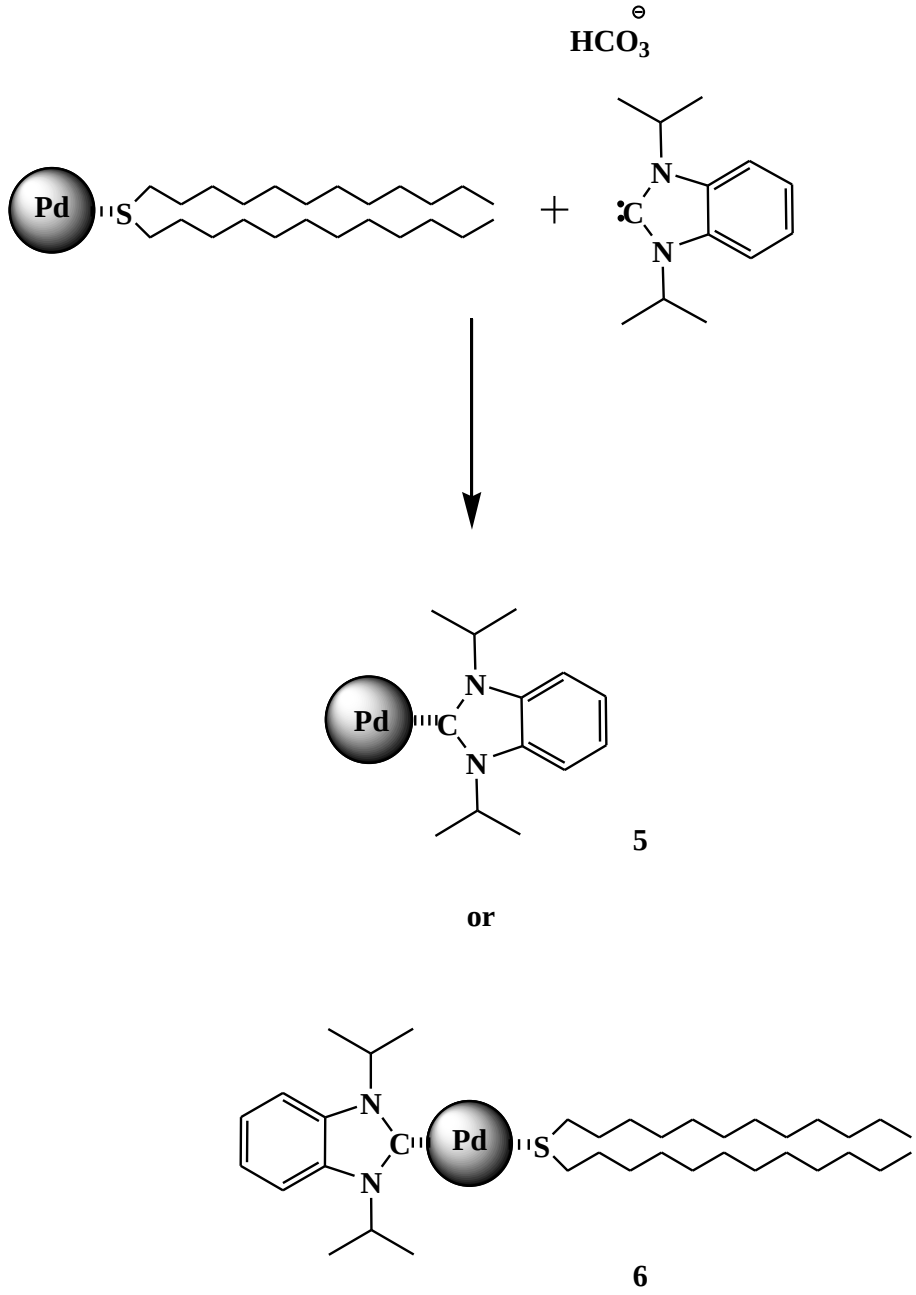

Figure 6-2: Ligand exchange of Pd nanoparticles; dodecyl sulfide protected Pd nanoparticles, reaction with N-heterocyclic carbene. 5 denotes the fully substituted Pd nanoparticles and 6 represents partially substituted product.

possibilities in the outcome of this reaction. For example, NHC would successfully replace the dodecyl sulfide giving rise to the product 5, or dodecyl sulfide might be partially substituted by the NHC, giving rise to product 6, or there will be a mixture of completely, partially substituted products, and unreacted compounds.

Substitution of dodecyl sulfide by NHC 1 and NHC 2 were analysed by XPS. Figure 6-3 shows the XPS spectrum of Pd 3d, S 2p, and N 1s of nanoparticles substituted by NHC 1 and 2. It is seen from the figure that following the substitution process the chemical state of Pd remain unchanged since single Pd $3d_{5/2}$ peak was recorded at 335.07 eV and 335.44 eV respectively. Then, the presence of a N 1s peak confirms the ability of NHC 1 and NHC 2 to substitute dodecyl sulfide from the Pd nanoparticles surfaces. For both cases S 2p spectra were recorded, indicating the presence of residual sulfur on the nanoparticles surface. This means it was not possible to completely remove all S compounds by the NHCs. The XPS peak position and the relative peak intensities were also calculated and presented in table 6-1. The C:S ratio on the Pd nanoparticles surface have changed before and after the NHC treatment. The C:S ratio increases in both cases due to the loss of sulfur compound from the nanoparticles surface by the NHC. Again the calculated N:S ratio gives information about the amount of NHCs on the nanoparticles surface relative to the S compound.

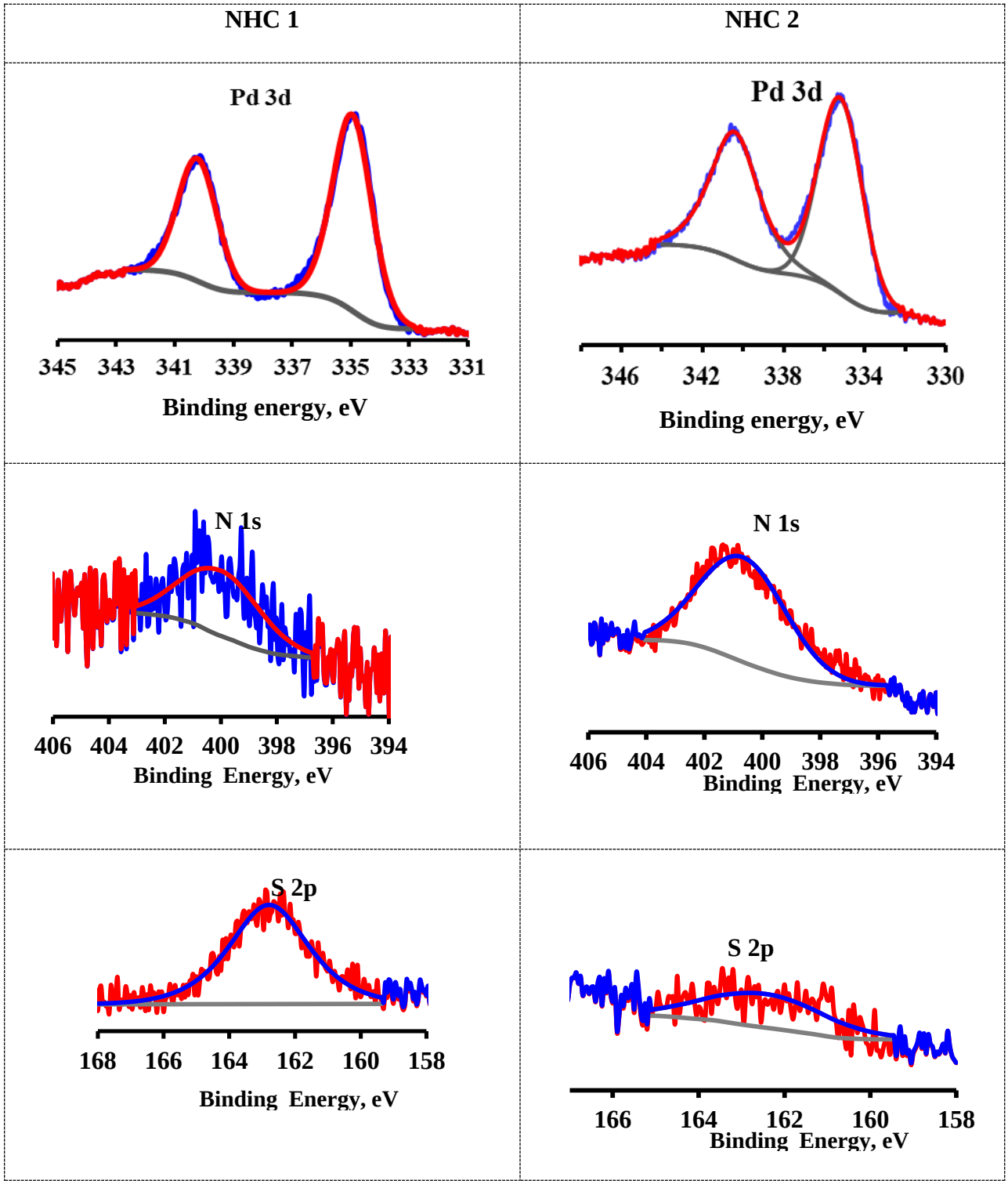

Figure 6-3: Representative Pd 3d, N 1s and S 2p XPS peaks of NHC 1 and NHC 2 treated Pd nanoparticles.

The relative intensity of the N 1s peak to the S 2p peak was higher for NHC 2 treated Pd nanoparticles, suggesting that NHC 2 is a better candidate here. This is because the sterics and electronics of carbenes play an important role in their chemical activity. Bulky and electron withdrawing mesitylene (1,3,5-trimethylbenzene) groups in NHC 1 slow down the reaction between carbene and nanoparticles surface. On the other hand, isopropyl groups in NHC 2 are not as bulky as the former one, resulting in better performance. In other sense, may be the carbene precursor is better than the plain carbene.

Table 6-1: XPS data of NHC substituted Pd nanoparticles.

Sample	**XPS Peak Position**			**N : S ratio**	**C : S ratio**	
					Before substitution	**After substitution**
	Pd 3d	**S 2p**	**N 1S**			
Pd NP-NHC 1	335.1	163.7	399.7	0.96 : 1	34 : 1	72 : 1
Pd NP-NHC 2	335.4	163.4	399.9	2.1 : 1		91: 1

Efforts have been invested to see the influence of the size of the nanoparticles in the substitution or ligand exchange process. Three different sizes of nanoparticles were synthesized following the procedure outlined in Chapter 5. As per Chapter 5, these three different types of Pd nanoparticles are denoted X, Y, and Z. Then the Pd nanoparticles were treated with NHC 2 since it was found more effective in the first experiment and characterized by XPS. Figure 6-4 shows representative the N 1s and S 2p spectra of the three different Pd nanoparticles treated by NHC 2. The N 1s and S 2p spectra show the same overall shape and peak position for each of the nanoparticles that were substituted. Again, the presence of S 2p peak in the XPS spectra, in all cases, demonstrates the presence of residual S on the nanoparticles surface. But the observed strong N 1s signal is consistent with the binding of NHC to the Pd nanoparticles surface.

Quantitative analysis of the NHC treated Pd nanoparticles is presented in table 6-2. The table also contains information about the size of the nanoparticles, and binding energies of N 1s and S 2p peak position. The C:N ratio in the X and Y nanoparticles is only slightly larger than the expected stoichiometric value of 6.5 for the NHC itself. The S signal cannot be completely removed here. These C:N ratios suggest that dodecyl sulfide itself must no longer be present in large quantities. Because the presence of dodecyl sulfide on the nanoparticles surface would contribute to the higher C:N ratio. The S might form Pd-S bond within the outer shell of the nanoparticles. However, the high C:S ratios suggest the minimum amount of S present on the nanoparticles surface.

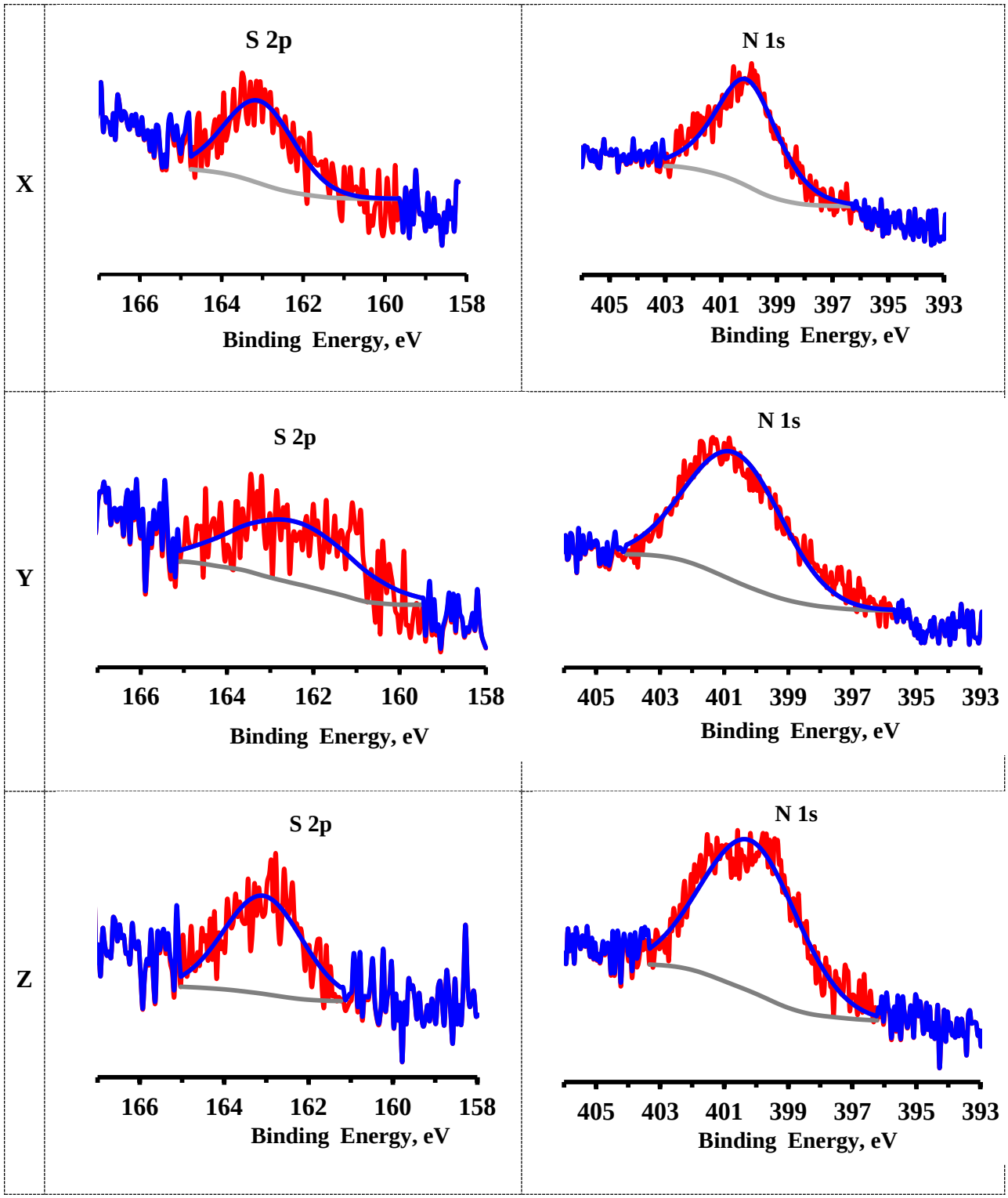

Figure 6-4: S 2p and N 1s XPS peaks of NHC treated Pd nanoparticles (X, Y, and Z)

Table 6-2: XPS results of NHC treated different sizes of Pd nanoparticles.

Pd nanoparticles sample	**Nanoparticle diameter (nm)**		**XPS Peak Position (eV)**		**N:S ratio**	**C:N ratio**	**C : S ratio**
	Before	**After**	**N 1s**	**S 2p**			
Pd NP-**X**-NHC	1.5 - 2.5	1 - 3	400.1	163.1	2.6 : 1	7.7 : 1	415 : 1
Pd NP-**Y**-NHC	2.5 - 4	1 - 4	400.6	163.5	4.8 : 1	7.3 : 1	194 : 1
Pd NP-**Z**-NHC	4 - 5.5	18 - 21	400.2	163.1	6.7 : 1	13.5 : 1	363 : 1

Efforts have been made to analyze the size of the Pd nanoparticles after NHC substitution. Figure 6-5 contains the representative TEM micrographs and corresponding size distribution histograms of NHC terminated Pd nanoparticles The images show that for the first two cases (X and Y), the resulted nanoparticles sizes remain small with some agglomeration. In the third sample (Z), the agglomeration was higher and larger nanoparticles were recorded.In all cases agglomeration was also seen in the TEM. The agglomeration is likely due to the rearrangement of the nanoparticles during the substitution process.

a. Pd NP-**X**-NHC

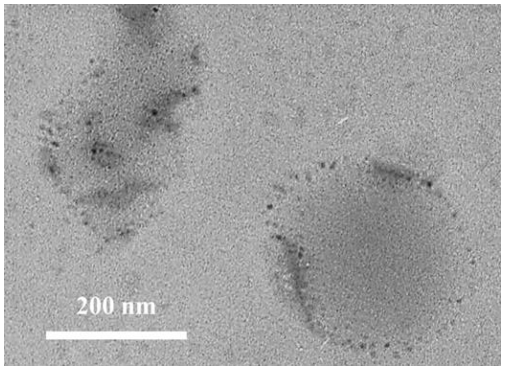

b. Pd NP-**X**-NHC

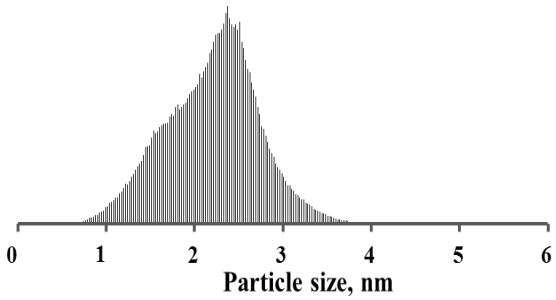

c. Pd NP-**Y**-NHC

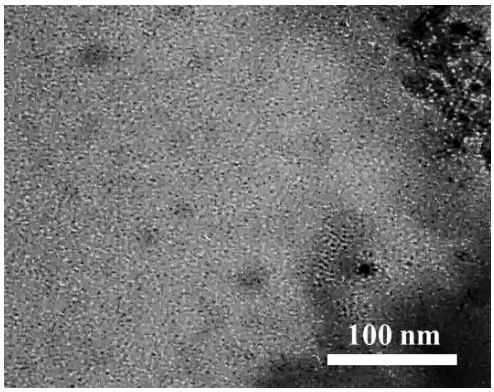

d. Pd NP-**Y**-NHC

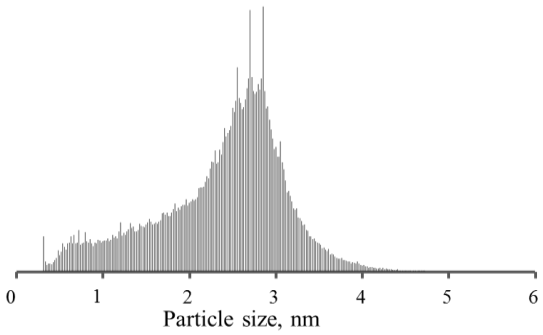

e. Pd NP-**Z**-NHC

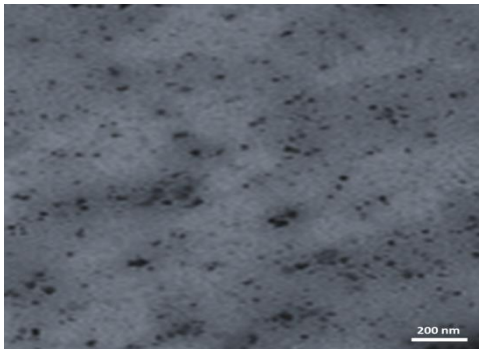

f. Pd NP-**Z**-NHC

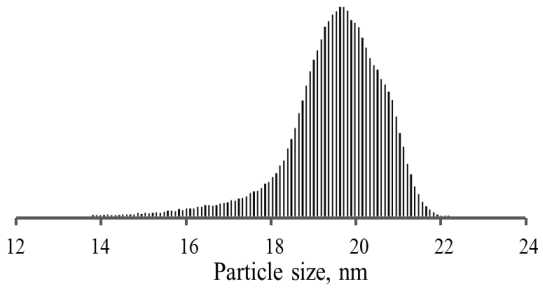

Figure 6-5: TEM images and corresponding histograms of NHC 2 treated Pd nanoparticles.

In the next experiment, Pd nanoparticles (Size = Y type) were reacted with the NHC precursor containing a marker element (fluorine and bromine). The presence of the marker species will give a better indication of the overall degree to which the NHC has been incorporated into the nanoparticle. Figure 6-6 represents the XPS spectrum of the Pd nanoparticles treated with NHC 3.

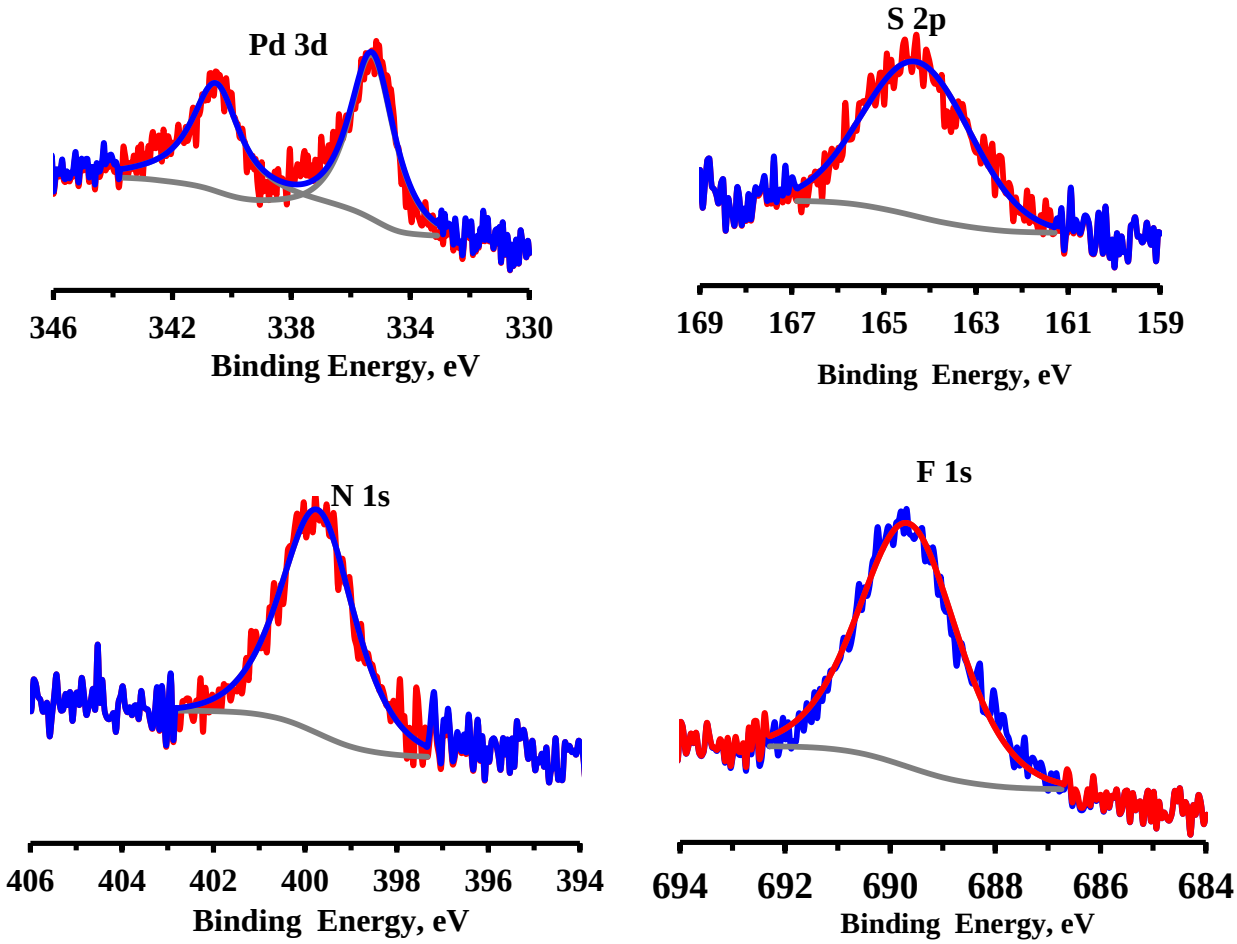

Figure 6-6: Pd 3d, S 2p, N 1s, and F 1s XPS signal of NHC 3 treated Pd nanoparticles.

The sharp Pd 3d peak indicates the consistency of the Pd nanoparticles following substitution process. Again presence of the N 1s peak tells us the formation of Pd-C bonds and

the S 2p peak indicated the presence of residual S. In addition, the presence of the F peak at 689.8 eV binding energy region confirms the presence of NHC 3 on the Pd nanoparticles surface. Similarly, for NHC 4 treated Pd nanoparticles gave Br signal as well as N signal (figure 6-7). Br 3d peak at 71.0 eV binding energy region corresponds to the presence of NHC 4 on the Pd nanoparticles surface.

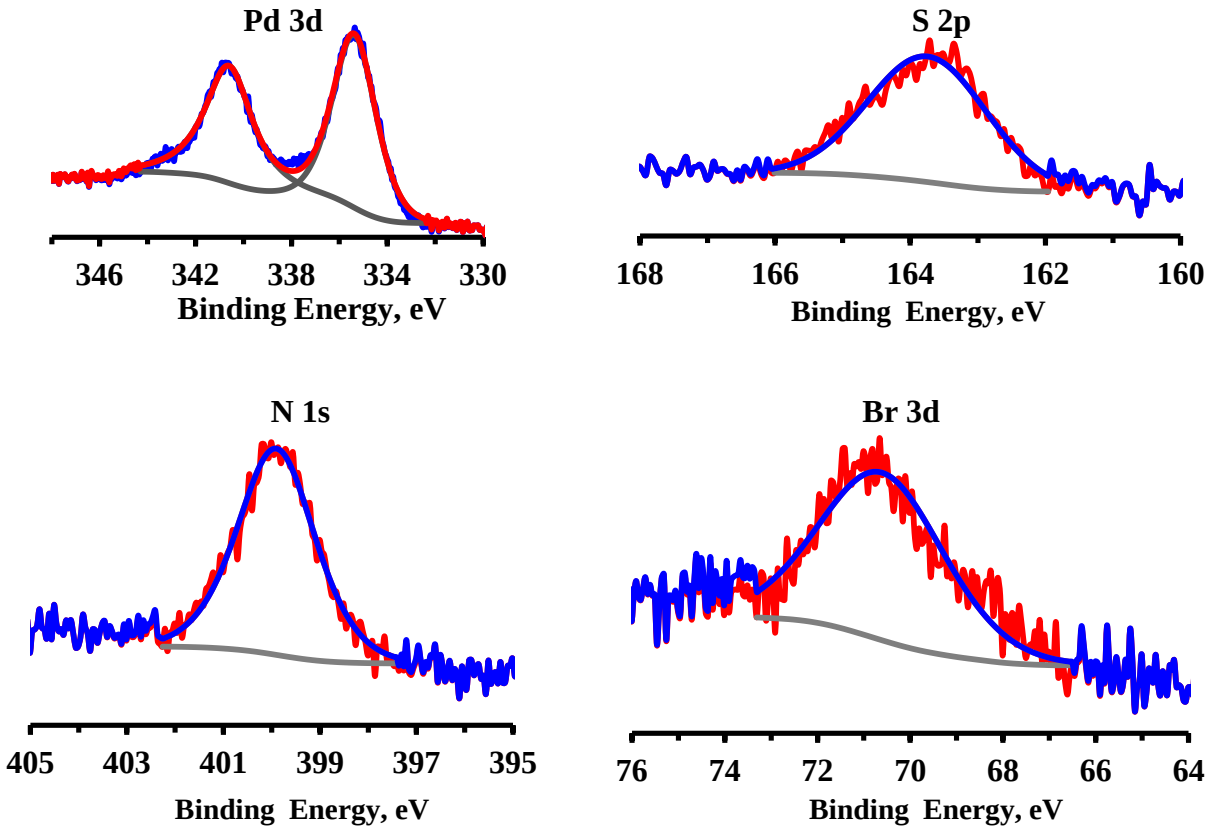

Figure 6-7: S 2p, N 1s, and F 1s XPS signal of NHC 4 treated Pd nanoparticles.

Table 6-3 presents the XPS data of Pd nanoparticles treated by NHC 3 and NHC 4. Quantitative analysis of the XPS peaks is presented here. The N:S and C:S ratios are consistent

with the previous experiment, suggesting the presence of smaller amount of S on the Pd nanoparticles surface. For NHC 3 substituted Pd nanoparticles, the N:F ratio is slightly higher than the stoichiometric value of 2.0, whereas the N:Br ratio was found a little larger high than the stoichiometric value.

Table 6-3: XPS results of NHC 3 and NHC 4 treated different sizes of Pd nanoparticles.

Pd nanoparticles sample	**XPS Peak Position**			**N : S ratio**	**C : S ratio**	**N : F / N : Br**
	N 1s	**S 2p**	**F 1s/ Br 3d**			
Pd NP-NHC 3	400.0	163.5	689.8	3.5 : 1	162 : 1	2.3 : 1
Pd NP-NHC 4	399.8	163.6	71.0	2.8 : 1	170 : 1	8.7 : 1

6.4 Conclusion

The properties of nanoparticles largely depend on the functionalities on its surface. Like Pd metal, the application of Pd nanoparticles is increasing. Here, Pd nanoparticles were treated with NHC and NHC precursor. From the preliminary results it was found that NHC precursors/ carbonate salts showed better performance in substituting S-based stabilization agent from the Pd nanoparticles surfaces. However, a control experiment with a series of plain NHCs and NHC precursors would give comprehensive information about this. It has been found, regardless of the type of NHC and size of the Pd nanoparticles, that NHC can be incorporated on the Pd nanoparticles surface and forms a Pd-C bond. The residual S was recorded on the Pd nanoparticles surface suggesting that small amount of S is likely present in the form of PdS within the outer shell of the nanoparticle. The NHC content might be improved by changing the solvent and reaction condition. Alternatively, the ability of NHCs to substitute dodecyl sulfide from the Pd surface can be analyzed by using a flat Pd foil surface (model surface that mimics the Pd nanoparticles surface). However, the preliminary data shows the potential use of NHCs as the capping agent of Pd nanoparticles which might be useful in changing the surface properties of Pd nanoparticles. As a result it will enhance the scope of the use of Pd nanoparticles in various applications.

6.5 References

(1) Daniel, M. C.; Astruc, D. *Chem. Rev.* **2004**, *104*, 293.

(2) Burda, C.; Chen, X. B.; Narayanan, R.; El-Sayed, M. A. *Chem. Rev.* **2005**, *105*, 1025.

(3) Chen, S.; Templeton, A. C.; Murray, R. W. *Langmuir* **2000**, *16*, 3543.

(4) Crudden, C. M.; Horton, J. H.; Ebralidze, I. I.; Zenkina, O. V.; McLean, A. B.; Drevniok, B.; She, Z.; Kraatz, H.-B.; J.Mosey, N.; Seki, T.; Keske, E. C.; Leake, J. D.; Rousina-Webb, A.; Wu, G. *Nat. Chem.* **2014**, *6*, 409.

(5) Herrmann, W. A. *Angew. Chem. Int. Ed.* **2002**, *41*, 1290.

(6) (a) Chen, W.; Davies, J. R.; Ghosh, D.; Tong, M. C.; Konopelski, J. P.; Chen, S. *Chem. Mater.* **2006**, *18*, 5253(b) Mirkhalaf, F.; Paprotny, J.; Schiffrin, D. J. *J. Am. Chem. Soc.* **2006**, *128*, 7400.

(7) Cookson, J. *Platinum Met. Rev.* **2012**, *56*, 83.

(8) Marion, N.; de Fremont, P.; Lemiere, G.; Stevens, E. D.; Fensterbank, L.; Malacria, M.; Nolan, S. P. *Chem. Commun.* **2006**, 2048.

(9) Lide, D. R. *CRC handbook of chemistry and physics: a ready-reference book of chemical and physical data*; CRC Press: Boca Raton, FL, 2004.

(10) Hurst, E. C.; Wilson, K.; Fairlamb, I. J. S.; Chechik, V. *New J. Chem.* **2009**, *33*, 1837.

(11) Richter, C.; Schaepe, K.; Glorius, F.; Ravoo, B. J. *Chem. Commun.* **2014**, *50*, 3204.

Chapter 7

Conclusion and Perspectives

The results in the previous chapters have addressed several issues on supported Pd catalysts and Pd nanoparticles. In this thesis, XPS has been used as the primary technique for characterization of samples. Efforts have been made to systemically understand the surface modification and characterization. After obtaining a completely hydrophilic Si wafer surfaces with –OH terminal group, a smooth overlayer of MPTMS was developed on that. This in turn acted as the support for the model Pd catalysts. In the fresh model catalysts, Pd 3d XPS peaks confirm the presence of two types of Pd species: one is a S bound Pd (II) species and another is in the form of Pd nanoparticles. The latter is found to be more active as a catalyst than the former, whereas the former was found more stable under the reaction conditions. The Wagner plot analysis showed a shift of binding energies of Pd following the Suzuki-Miyaura reaction. In addition, two types of sulfur atoms were also identified from the S 2s spectra. While S has not been well documented in this type of catalyst, an extensive study of a series of S containing compounds helped in identifying the new species of S in the model catalysts.

A good understanding has also been obtained on the synthesis of different sizes of Pd nanoparticles using PVP and dodecyl sulfide as the stabilizing agent. The XPS data gave comprehensive information about the formation of Pd nanoparticles and presence of the stabilizing agent. In addition, information about the sizes of a series of nanoparticles can be found from the XPS data. TEM confirms the proper size distribution and dispersion of Pd

nanoparticles. The shifts of binding energies of different Pd nanoparticles were documented in the Wagner plot. From this experiment, if was found that the shift of the binding energy of Pd nanoparticles is directly relate to the extra-atomic relaxation effect.Large particles experience higher screening/ polarization of electrons from their surroundings, resulting in a decrease of binding energy.

Finally, the NHC substitution experiment of Pd nanoparticles showed the ability of NHC to attach to the Pd nanoparticles surface by removing the existing S-based stabilizing agent. Better understanding the process and using NHCs with different functionalities would certainly widen the scope of the use of Pd in various applications. Further work can also be performed using a flat Pd foil to better understand the process and properties of the NHC-terminated Pd surface. Following that the NHC-terminated surfaces or nanoparticles can be treated with different solvent (for example 1% H_2O_2) and conditions to check the stability of the Pd-C bond. In addition, a reversible reaction of the NHC-terminated Pd with dodecyl sulfide can also be performed to better understand the properties of the NHC-terminated Pd. All of those samples can be successfully characterized by surface analytical techniques especially by XPS. In addition, information about the form of the residual S on the Pd nanoparticles surface can also be analyzed by the solid-state NMR.